Supporting Information for

Unusual Spectral Diffusion of Single $CuInS_2$ Quantum Dots Sheds Light on the Mechanism of Radiative Decay

Stijn O.M. Hinterding[1,2], *Mark J.J. Mangnus*[1,2], *P. Tim Prins*[3], *Huygen J. Jöbsis*[3], *Serena Busatto*[3], *Daniël Vanmaekelbergh*[3], *Celso de Mello Donega*[3], *Freddy T. Rabouw*[1,2,*]

[1]Soft Condensed Matter, [2]Inorganic Chemistry and Catalysis, and [3]Condensed Matter and Interfaces, Debye Institute for Nanomaterials Science, Utrecht University, Princetonplein 1, 3584CC Utrecht, The Netherlands

[*]Corresponding author. E-mail: f.t.rabouw@uu.nl.

Section S1: Experimental

Chemicals

Indium(III) acetate [$In(Ac)_3$, 99.99%], Copper(I) iodide (CuI, 98%), 1-dodecanethiol (DDT, $\geq$98%), Cadmium(II) oxide (99.5%), Oleic Acid (OA, 90%), 1-octadecene (ODE, tech. 90%), Sulphur (99.98%), Trioctylphosphine (TOP, Fischer Scientific), Acetone (VWR International BV, dried, max. 0.0075% H_2O), and Toluene (99.8%) were purchased from Sigma-Aldrich and used as received, unless specified otherwise. ODE was degassed for 2 h at 110 °C prior to use.

Synthesis of $CuInS_2$ quantum dots

$CuInS_2$ (CIS) quantum dots (QDs) were synthesized by adapting the method described by Zhong et al.[1] Briefly, $In(Ac)_3$ (3 mmol), CuI (3 mmol) and DDT (5 mL) were combined in a roundbottom flask, degassed for 10 min and brought under N_2 atmosphere. The mixture was stirred and heated to 100 °C for 30 min, until the mixture became transparent. Next, the mixture was degassed at 60–70 °C to remove any volatile species. These heating and degassing steps were repeated until no more bubbles were observed when the mixture was brought under vacuum. Under N_2 atmosphere, the mixture was rapidly heated to 230 °C. This temperature was maintained for 5 min, after which the reaction was quenched by removal of the heat source and active cooling of the flask with compressed air. The core-only CIS QDs were isolated by addition of a non-solvent (acetone), followed by centrifugation at 2800 revolutions per minute for 15 min and re-dispersion of the precipitate in toluene. These washing steps were repeated three times. The batch of core-only CIS QDs used as seeds for the core/shell CIS/CdS QDs were not washed.

Preparation of Cd-oleate solution

CdO (9 mmol), OA (36.8 mmol), and ODE (12.2 mmol) were combined and degassed for 1 h at 80 °C. The mixture was then brought under N_2 atmosphere and heated at 280 °C for 1 h, to form a clear solution. The solution was further degassed for 12 h at 110 °C and finally kept under N_2 atmosphere.

Preparation of TOP-S

A 2 M solution of sulphur in TOP was prepared by addition of sulphur (20 mmol) to TOP (10 mL), inside a N_2-filled glovebox.

Growth of CdS shell

Growth of a CdS shell on the core CIS QDs was done by adapting the method described by Li et al.[2] Briefly, the crude QD reaction mixture (3 mL) and ODE (36 mL) were combined in a roundbottom flask and degassed for 10 min. Under N_2 atmosphere, the flask was heated to 210 °C, at which point a mixture of TOP-S (3.6 mmol), Cd-oleate (3.6 mmol), and ODE (12 mL) was added dropwisely over the course of 20 min using a syringe pump. The sample was further annealed for 20 min after which the reaction was quenched by removal of the heat source and cooling with compressed air. The core/shell CIS/CdS QDs were washed in the same way as the core-only QDs.

Ensemble absorption, photoluminescence, and excitation spectroscopy

The core and core/shell samples were diluted in anhydrous toluene and transferred to 10 mm $\times$ 10 mm quartz cuvettes. The absorption spectra were recorded using a double-beam Perkin-Elmer Lambda 950 UV/vis/NIR spectrometer. The photoluminescence (PL) spectra were recorded on a fiber-coupled spectrometer (Ocean Optics, USB4000) using a 395-nm LED as excitation source. The wavelength-dependent detection efficiency of this spectrometer was corrected for using a calibrated light source (Avantes AvaLight-DH-CAL). Photoluminescence excitation spectra were obtained on an Edinburgh FLS920 fluorescence spectrometer with a double monochromator in the excitation path and equipped with a 450 W lamp (Edinburgh Xe2 XenonArc) as excitation source. The spectrometer internally corrects for the shape of the lamp spectrum. To avoid second-order excitation a 400-nm long-pass filter was placed in the excitation path. Emission was detected by a Hamamatsu R928 photomultiplier tube equipped with a water-cooled refrigerated chamber (Photocool TE177RF).

Ensemble time-resolved photoluminescence spectroscopy
The core and core/shell samples were diluted in anhydrous toluene and transferred to 10 mm $\times$ 10 mm quartz cuvettes. Ensemble-scale PL decay measurements were performed using either a 405-nm or 510-nm pulsed diode laser (Edinburgh Instruments, EPL-405 or EPL-510, 100 kHz repetition rate) as excitation source, with detection by a photomultiplier tube (Hamamatsu H7422).

Electron microscopy, electron diffraction and energy-dispersive X-ray spectroscopy
Electron micrographs, electron diffraction (ED) patterns, and energy-dispersive X-ray spectra (EDS) were recorded on a Thermo Fisher Scientific Talos F200X operating at 200 kV. Samples were prepared by drop-casting a QD dispersion onto a carbon-coated gold TEM-grid. The ED patterns were calibrated using a AuPd reference sample.

Small and wide-angle X-ray scattering
Small- and wide-angle X-ray scattering measurements (SAXS, WAXS) were performed at the SWING beamline, part of the SOLEIL synchrotron in Saint-Aubin, France.[3] The energy of the X-rays used was 16 keV. For SAXS a EigerX4M detector in a vacuum tube was used at a distance of 1.83 m from the sample. For WAXS a Merlin detector was used. For both SAXS and WAXS the q-range was calibrated using a silver behenate reference.[4] The CIS core-only QDs were placed inside a quartz capillary with a diameter of 1 mm. A home-built capillary holder was used to place the sample inside the beam. The collected 2D scattering patterns were processed to 1D scattering patterns via beamline specific software (Foxtrot). The scattering pattern from the solvent and capillary were subtracted from the QD scattering pattern as discussed in Ref. 5.

Sample preparation for single-quantum-dot measurements
Our sample preparation procedure was aimed at maximizing the QD stability under prolonged illumination while minimizing background luminescence. Glass #1.5 coverslips and glass microscopy slides were cleaned using a low-pressure plasma cleaner (Diener Zepto), operated at 0.2–0.4 mbar, at the maximum power setting. Inside a N_2-filled glovebox, the QD dispersion was diluted 10^5–$10^6\times$ with a 1-vol% solution of ethyl mercaptoacetate in distilled toluene. 30 µL of the diluted QD dispersion was placed on a plasma-cleaned coverslip, smeared out using a second coverslip, and the solvent was allowed to evaporate. Next, the coverslip was placed sample-side down onto a plasma-cleaned microscopy slide. The edges of the assembly were sealed with Norland #68 UV-curable glue, which contains a volatile thiol component.[6] The glue was not cured.

Core-only $CuInS_2$ and core/shell $CuInS_2$/CdS samples used in experiments
The synthesis of the CIS/CdS core/shell QDs consumed nearly an entire batch of non-washed core-only CIS QDs. As a result, there was too little material left over of this batch (denoted here as "CIS-A") to allow for the proper washing procedures required for single-particle measurements. Therefore, a different batch of core-only CIS QDs (denoted here as "CIS-B") was used in the single-particle measurements. The CIS-A and CIS-B batches are spectroscopically virtually identical (see Section S2).

Fluorescence microscopy experiments
Single-QD measurements were performed on a home-built microscopy setup. This setup consisted of a Nikon Ti-U inverted microscope, on which the sample was placed. The excitation light source was a 405-nm ps-pulsed diode laser (Picoquant D-C-405), operated at a repetition rate of 500 or 250 kHz (for measurements on core-only CIS or core/shell CIS/CdS QDs, respectively). The excitation light was guided into an oil-immersion objective (Nikon CFI Plan Apochromat Lambda 100$\times$, NA 1.45) by a dichroic long-pass mirror. Before entering the microscope, the excitation beam was guided through an iris with a diameter of 2.0 mm. This underfilling of the objective back-aperture reduces the effective NA for excitation (we estimate an NA of 1.2, based on a measured back-aperture diameter of 5 mm). We thus obtain a slightly larger diffraction-limited excitation spot, which makes the measurements less sensitive to drift. PL was collected by the same objective and filtered by suitable long-pass filters to remove reflected excitation light. Additionally, the PL was filtered by a 600-nm long-pass filter (Thorlabs FEL0600) to minimize the detection of background luminescence. The PL signal was then directed to one of three detection setups: (i) two avalanche photon diodes (APDs; Micro Photon Devices PDM) in Hanbury Brown-Twiss configuration, (ii) a spectrograph (Andor Kymera 193i) equipped with an electron-multiplying charge-coupled device detector (EMCCD; Andor iXon Ultra 888), or (iii) a setup in

which a non-polarizing beamsplitter directed half of the PL into the same spectrograph and the other half onto an APD. The wavelength-dependent detection efficiency of the spectrograph–EMCCD pair (which decreases significantly in the NIR) was corrected for using a broadband calibration light source (Ocean Optics, HL-3plus-CAL). The EMCCD detector, avalanche photon diodes, and laser driver (Picoquant PDL 800-D) were connected to a time-to-digital converter (qutools quTAG), that communicated the spectrum-recording, laser-pulse, and photon-detection events to a computer. Live time-correlated single-photon data visualization and storage was performed using home-written software.[7]

Fluorescence microscopy data processing and analysis

Custom Python scripts were used to process and analyze the single-QD data. The raw data obtained from the time-to-digital converter contains a list of time tags for each signal received from our instruments: the APDs, the EMCCD camera, and the laser driver.

The event lists from the laser driver and APD signals are compared to calculate the delay time for each photon detected. For each APD separately, a constant delay-time correction is then determined from the temporal position of the decay curve maximum. This correction time accounts for, amongst other factors, a time lag between the signals from laser driver and APD due to different cable lengths and light travel time. The negative delay times t that this produces are shifted by a laser pulse period T via $t \rightarrow t + T$. Such photons, that were detected close to the rise in the decay curve (originating from the finite instrument response function), were ignored in the further data analysis.

Our APDs exhibit so-called *afterpulsing*: after a valid photon detection event, there is a probability that the APD reports a false photon detection event. We removed such after-pulsing events in post-processing by using only the first photon detection event per laser pulse and per detector for further analysis, and discarding any other events.

Where possible, we confirmed that we measured emission from an individual QD, instead of multiple QDs, by measuring the cross-correlation $g^{(2)}(\tau)$ between two detectors in Hanbury Brown-Twiss configuration. A relatively low correlation at lag time $\tau = 0$, compared to the side-peaks at $\pm$ the laser pulse period (4000 or 2000 ns), confirms that we detect emission from an individual (nearly) single-photon emitter.

The event list of the EMCCD channel contains the times at which the camera started integrating individual spectra. With the data from this channel and known camera integration time, the start and end time of each spectral recording is calculated. These start and end times, in turn, are used to link each detected photon on the APD to a corresponding spectrum.

For both the measurements on core-only CIS and core/shell CIS/CdS QDs, the spectral integration time was 100 ms. However, to improve the signal/noise ratio in the data analysis of the core/shell CIS/CdS QDs, every four subsequent PL spectra were accumulated, thus yielding an effective integration time of 400 ms.

Excitation regime

We estimate the excitation regime, i.e. the average number of excitons generated in a single QD per laser pulse, based on the single-QD absorption cross-section and the applied laser power. For measurements on the core-only CIS QDs, we estimate a single-QD absorption cross-section of 0.10 nm^2, based on an absorption cross-section per CIS formula unit of $1.18 \cdot 10^{-17} \mathrm{cm}^2$ at 3.1 eV,[8] a CIS chalcopyrite unit cell volume of 339.192 $Å^3$,[9] and a core-only particle diameter of 2.4 nm (see Section S2). We estimate the absorption cross-section of the CIS/CdS core/shell QDs in the same way, i.e. we assume that the growth of a CdS shell has a similar effect as increasing the size of a CIS-only QD (using a core/shell QD diameter of 3.0 nm, Section S2). We thereby estimate an absorption cross-section of 0.20 nm^2. In the measurements on individual core-only (core/shell) QDs, we used excitation powers of 35 (23) nW, at a repetition rate of 500 (250) kHz, corresponding to a fluence of 52 (69) μJ/cm^2 [for a diffraction-limited excitation-spot diameter of 412 nm, based on an effective excitation NA of 1.2 (see above)]. This yields an average number of excitations per laser pulse of 0.11 and 0.28, for the core-only and core/shell measurements, respectively.

Section S2: Ensemble-scale characterization of core-only $CuInS_2$ and core/shell $CuInS_2$/CdS samples

Electron microscopy and EDS

The CIS core-only and CIS/CdS core/shell QDs were studied using electron microscopy (see Section S1 for details). Unfortunately, the small particle size and poor contrast prohibit proper characterization, especially of the core-only particles. We therefore estimated the nominal core-only particle size using absorption spectroscopy, as well as WAXS and SAXS (see below). From the electron micrograph of the core/shell CIS/CdS QDs (see Figure S1a), we can conclude that our CIS/CdS core/shell QDs are heterogenous in size and shape. We can distinguish lattice fringes in the high-resolution electron micrographs (Figure S1b–d). Analysis of the fast Fourier transform (Figure 1e) indicates that the corresponding lattice spacings are 2.1 and 3.5 Å. We attribute these spacings to the $\{204\}$ and $\{11\bar{2}\}$ planes of chalcopyrite CIS,[9] respectively (see also Figure S3c,d).

We used EDS to determine the QD composition. Quantification of the EDS data (Figure 1f) yields an atomic Cu:In ratio of 1.0:0.78.

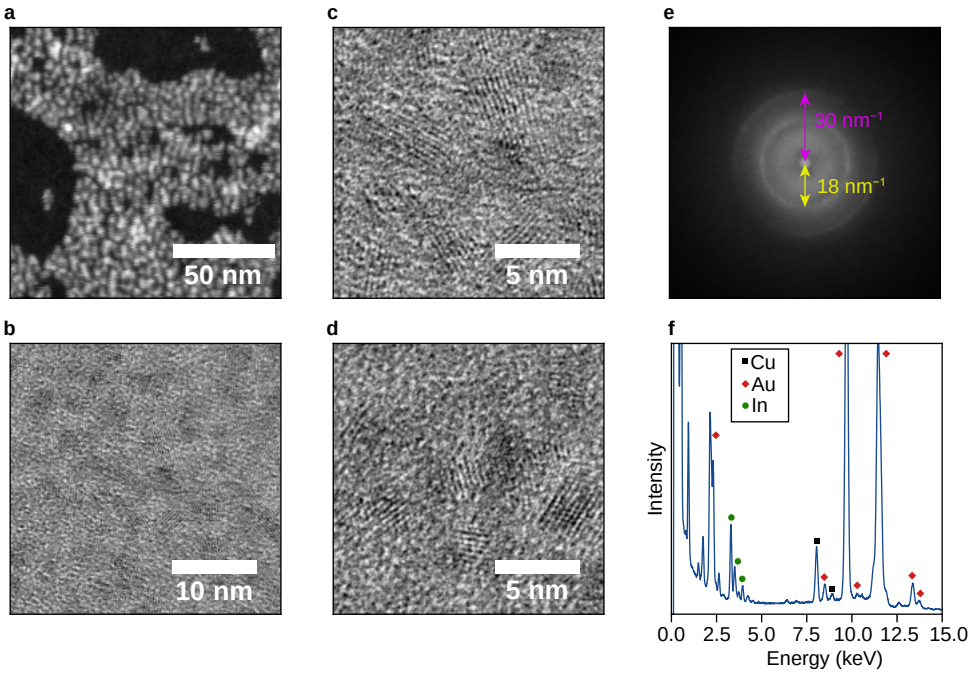

Figure S1 — Electron microscopy characterization. **(a)** High-angle annular dark-field micrograph, **(b–d)** high-resolution transmission electron micrographs (HRTEMs), and **(e)** fast Fourier transform of the HRTEM, of core/shell CIS/CdS QDs. **(f)** Energy-dispersive X-ray emission spectrum of core-only CIS QDs. The Au signal originates from the Au electron microscope grid. The inverse lattice spacings $q = 2\pi/d$ (with d the real-space lattice spacing) are indicated in panel **e**.

Optical spectroscopy

Both batches of core-only CIS QDs are spectroscopically virtually identical (compare absorption and emission spectra in Figure S2a). As we were not able to obtain electron micrographs of sufficient quality to measure the particle size (see above), we used the absorption spectra of the core-only samples to estimate their nominal particle size. First, we determined the position of the first absorption feature by finding the minimum in the second derivative of the spectrum. To this end, the absorption spectrum was fitted with a polynomial up to order 20 (see Figures S2b,c), which was used to calculate the second derivative (dashed line in Figure S2b,c). The obtained peak positions were related to the nanocrystal diameter using a literature sizing curve.[8] For the core-only CIS-A and CIS-B samples, the peak positions are 2.255 and 2.240 eV, respectively, corresponding to a diameter of 2.4 nm for both samples. We estimate a nominal diameter of 3.0 nm for the core/shell QDs, assuming that the CdS shell-growth procedure deposited a single monolayer of zinc-blende CdS onto the QD surface, which would increase the QD radius by 0.3 nm.[10]

The PL spectra of the core-only and core/shell QDs exhibit very similar line widths and peak positions (Figure S2d). The absorption spectrum of the core/shell QDs is slightly broadened compared to the core-only sample (see Figure S2d). The PL decay is multi-exponential, and is the same for 405 or 510-nm excitation (see Figure S2e,f). The decay of the core/shell sample is slower than that of the core-only sample, which may be due to an improved quantum yield, and/or due to reduced electron–hole wavefunction overlap, as the electron can delocalize over the entire core/shell particle, whereas the hole is restricted to the CIS core.

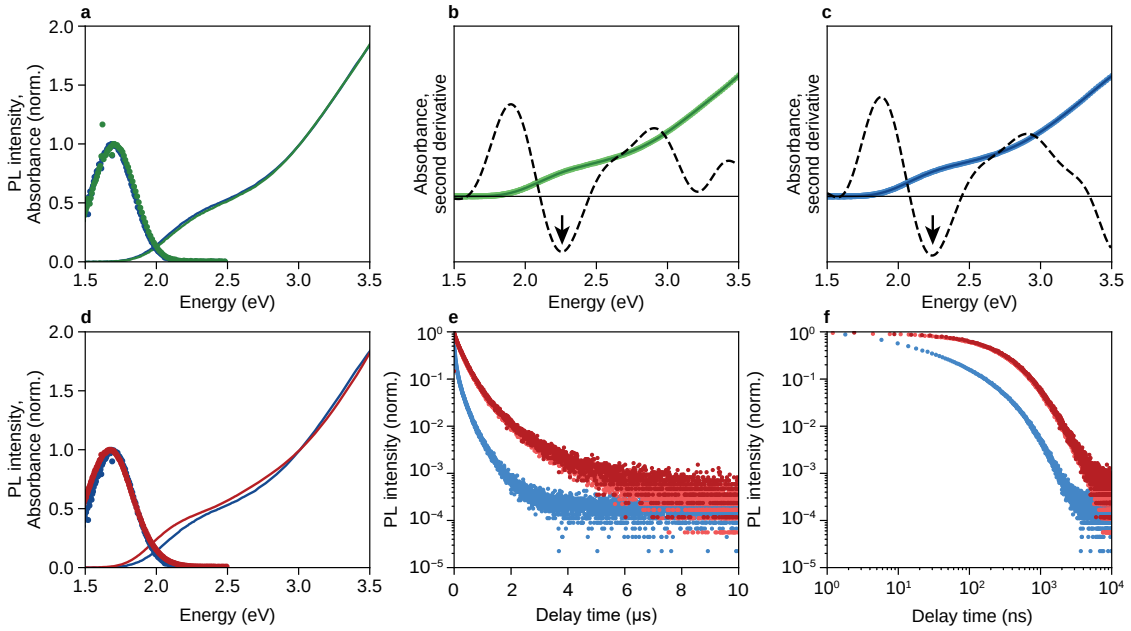

Figure S2 — Spectroscopy on core-only CIS and core/shell CIS/CdS ensembles. (**a**) (solid lines) Absorption and (circles) PL spectra, of (green) CIS-A and (blue) CIS-B. (**b,c**) (light lines) absorption spectra, (dark lines) polynomial fits, and (dashed black lines) second derivatives of the fitted polynomials, for the (**b**) CIS-A and (**c**) CIS-B core-only samples. Arrows indicate the position of the minimum in the second derivative. (**d**) The same as in (**a**), but for (blue) CIS-B and (red) CIS/CdS QDs. (**e**) Photoluminescence decay curves of (blue) CIS-B and (light red) CIS/CdS QDs, excited at 510 nm, and (dark red) CIS/CdS QDs, excited at 405 nm. (**f**) The same data as in (**e**), but plotted on double-logarithmic axes.

X-ray scattering and electron diffraction experiments

We have conducted small and wide-angle X-ray scattering (SAXS, WAXS) experiments on the core-only CIS QDs, as well as electron diffraction (ED) measurements on both the core-only CIS and the CIS/CdS core/shell QDs. The former two techniques allow an additional estimate of the CIS core-only QD size, while WAXS and ED provide information on the crystal structure. The SAXS diffraction pattern (Figure S3a) exhibits no minima, as expected for nanocrystals with a tetrahedral shape.[11] Using the Guinier-fit approach (Figure S3b), we obtain a radius of gyration of 1.2 nm.

The WAXS and ED patterns are shifted with respect to the chalcopyrite CIS reference peaks (Figure S3c). After manually scaling the q values these datasets coincide well with the reference peaks (Figure S3d), showing that both the core-only and the core/shell QDs exhibit the chalcopyrite crystal structure. We attribute the initial mismatch between the experimental data and the reference to calibration errors.

We additionally obtain a measure for the crystallite domain size τ following Scherrer's equation[12] $\tau = 2\pi K/\beta$, with $K \approx 1$ the Scherrer constant of a tetrahedral crystallite,[13] and β the full-width at half-maximum obtained from a Gaussian fit (Figure S3c). This approach yields $\tau = 2.7$ nm, in good agreement with the diameters estimated from the absorption and SAXS data.

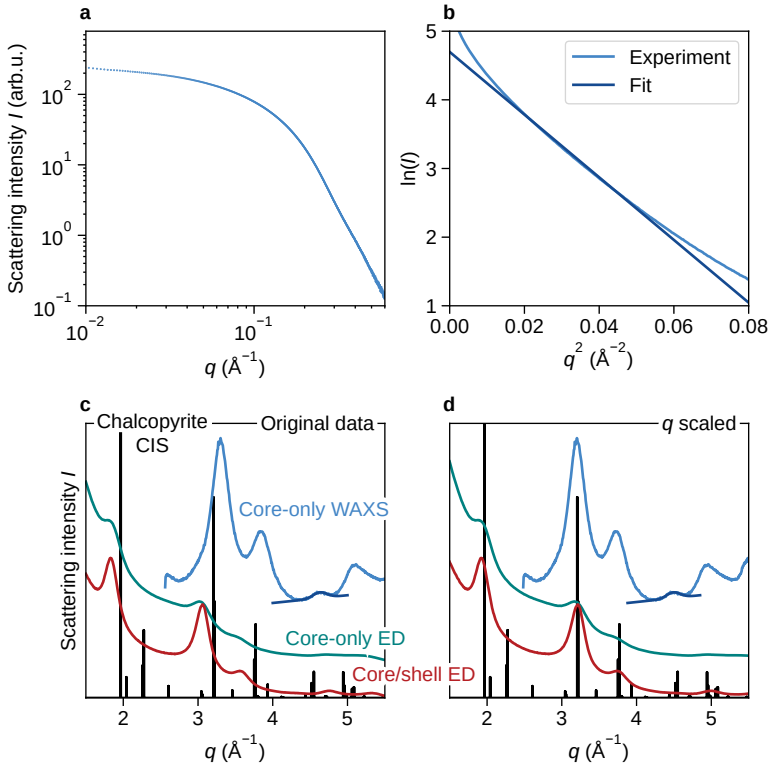

Figure S3 — Results of diffraction measurements. (**a**) SAXS diffraction pattern of core-only CIS QDs dispersed in toluene, and (**b**) Guinier plot of the same data. The dark blue line in **b** is a fit to the data. (**c**) (light blue) WAXS diffraction pattern of core-only CIS QDs dispersed in toluene; electron diffraction (ED) pattern of (green) core-only CIS QDs, (red) core.shell CIS/CdS QDs; (black) reference peaks for the chalcopyrite $CuInS_2$ crystal structure,[9] generated using the VESTA 3 software package.[14] (**d**) The same as in panel **c**, but the q values of the experimental data have been scaled by (WAXS, light blue) 0.97, and (ED, green, red) 1.05, to overlay the experimental data onto the reference peaks. The dark blue curve in **c,d** is the Gaussian fit used in the Scherrer analysis.

Fitting of ensemble-scale PL decay

The PL decay curve of the ensemble of CIS/CdS core/shell QDs was fitted with a simple model of a distribution of radiative decay rates due to a distribution of hole localization sites. We assume that the electron wave function is the lowest-energy solution to the particle-in-a-spherical-box problem, $\psi_{\mathrm{e}}(\mathbf{r}) = a\sin(\pi r/a)/\pi r$, while the hole is a delta function, $\psi_{\mathrm{h}}(\mathbf{r}) = \delta(\mathbf{r} - \mathbf{r}_{\mathrm{loc}})$. Here, a is the QD radius, and $\mathbf{r}_{\mathrm{loc}}$ is the hole localization site. The radiative lifetime is inversely proportional to the square of the electron–hole overlap integral:

$$\tau(r_{\mathrm{loc}}) = \frac{\pi^2 r_{\mathrm{loc}}^2 \tau_0}{a^2 \sin^2(\pi r_{\mathrm{loc}}/a)}, \tag{1}$$

where τ_0 is the radiative lifetime for $r_{\mathrm{loc}} = 0$. We assume that the distribution of hole localization sites (over the ensemble and time) is homogeneous over a sphere of radius $r_{\mathrm{max}} < a$ and no effect of nonradiative recombination. This produces

$$I(t, A, \tau_0, r_{\mathrm{max}}) = A \int_0^{r_{\mathrm{max}}} \frac{e^{-t/\tau(r_{\mathrm{loc}})}}{\tau(r_{\mathrm{loc}})} 4\pi r_{\mathrm{loc}}^2 dr_{\mathrm{loc}} \tag{2}$$

as a model for the PL decay curve. Fitting this to the data of Figure 2d yields a best fit with $\tau_0 = 111.2$ ns and $r_{\mathrm{max}} = 0.735a$. This is in good agreement with expected maximum radial position at which the hole can localize ($a_{\mathrm{core}}/a_{\mathrm{core/shell}} = 0.8$).

The distribution of lifetimes $\rho(\tau)$ in Figure 2f is defined such that

$$I(t, A, \tau_0, r_{\mathrm{max}}) = A \int_{\tau_0}^{\tau_{\mathrm{max}}} \frac{\rho(\tau)}{\tau} e^{-t/\tau} d\tau. \tag{3}$$

We calculated the distribution numerically as

$$\rho(\tau) = 4\pi r_{\mathrm{loc}}(\tau)^2 \frac{dr_{\mathrm{loc}}(\tau)}{d\tau}, \tag{4}$$

where $r_{\mathrm{loc}}(\tau)$ is the inverse of eq 1.

Section S3: Quantum-mechanical calculations

Here, we develop a theoretical model that describes spectral diffusion of photoluminescence and fluctuations in lifetime observed in CIS quantum dots. We apply a simple effective-mass model, where the CIS/CdS core/shell quantum dot is approximated as a spherical infinite potential well with radius a of 1.5 nm. The hole resides on specific localization sites within the CIS core (with radius b = 0.8a = 1.2 nm), while the electron is delocalized over the entire nanocrystal volume. There are two factors that strongly influence the exciton energy and lifetime, namely the radial position of the hole localization site and the presence of external electric fields (e.g. induced by mobile ligands/dangling bonds).

Linear electric-field approximation

In our simple model, we consider that two opposite charges $\pm q$ at opposite sides of a spherical particle of radius a produce an approximately homogeneous electric field of $F = q/(2\pi\epsilon\epsilon_0 a^2)$, where ϵ_0 is the vacuum permittivity and ϵ is the relative permittivity of the QD material. Two full elementary charges $q = e$ at opposite ends of a particle with radius $a = 1.5$ nm result in a field strength of $F = 1.3 \cdot 10^2$ MV m^{-1}. Compared to the actual, inhomogeneous, field distribution (Figure S4a), the assumption of a homogeneous field (Figure S4b) introduces deviations in the electrostatic potential V_{ext} only very close to the charges (Figure S4c,d). For the comparison of Figure S4, we do not consider effects of the dielectric contrast between the QD and its environment. We take $\epsilon = 10$ for chalcopyrite $CuInS_2$.[15–17]

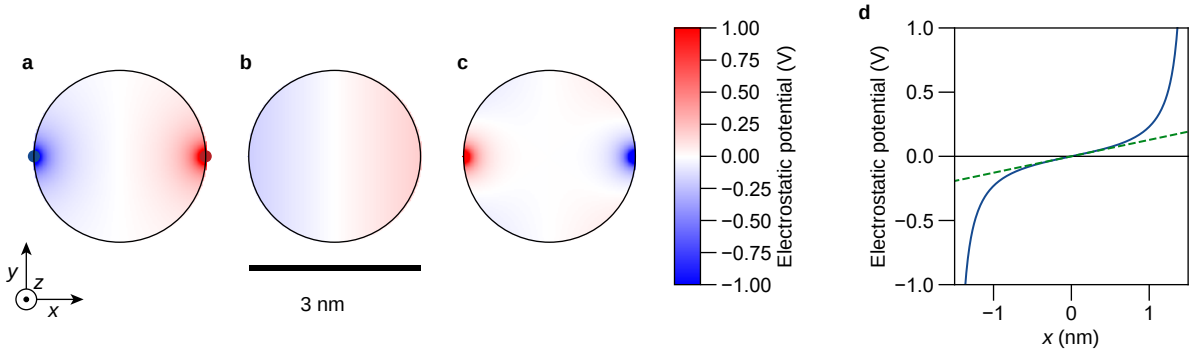

Figure S4 — Validity of linear electric-field approximation. (**a**) Electrostatic potential V_{ext} inside a sphere with radius a = 1.5 nm, with opposite elementary charges with charge $\pm e$ situated at opposite ends of the sphere (indicated by the small blue and red circles). (**b**) The electrostatic potential $V_{\mathrm{ext,hom}}$ obtained by approximating the field due to the charges as homogeneous. (**c**) The error in electrostatic potential $V_{\mathrm{ext,hom}} - V_{\mathrm{ext}}$ induced by the approximation of a homogeneous field. Panels (a–c) depict a cross-cut through the sphere, showing the x,y-plane, with z = 0. (**d**) (blue) V_{ext} and (green) $V_{\mathrm{ext,hom}}$ plotted along a line running through the center of the sphere.

Quantum-mechanical framework

The electron wave function $\psi^{\mathrm{e}}_{n_{\mathrm{e}},l_{\mathrm{e}},m_{\mathrm{e}}}(\mathbf{r}_{\mathrm{e}})$ can be expressed as a linear combination of spherical particle-in-a-box wave functions:

$$\psi^{\mathrm{e}}_{n_{\mathrm{e}},l_{\mathrm{e}},m_{\mathrm{e}}}(\mathbf{r}_{\mathrm{e}}) = \sum_{n_{\mathrm{e}},l_{\mathrm{e}},m_{\mathrm{e}}} c_{n_{\mathrm{e}},l_{\mathrm{e}},m_{\mathrm{e}}}\, \xi^{\mathrm{e}}_{n_{\mathrm{e}},l_{\mathrm{e}},m_{\mathrm{e}}}(\mathbf{r}_{\mathrm{e}}), \tag{5}$$

$$\xi^{\mathrm{e}}_{n_{\mathrm{e}},l_{\mathrm{e}},m_{\mathrm{e}}}(\mathbf{r}_{\mathrm{e}}) = \begin{cases} R^{\mathrm{e}}_{n_{\mathrm{e}},l_{\mathrm{e}}}(r_{\mathrm{e}})\, Y^{m_e}_{l_e}(\theta_{\mathrm{e}},\phi_{\mathrm{e}}) & \text{if } r < a, \\ 0 & \text{if } r \geq a. \end{cases} \tag{6}$$

where the radial part of the wave function is given by $R^{\mathrm{e}}_{n_{\mathrm{e}},l_{\mathrm{e}}}(r_{\mathrm{e}}) = A_{n_{\mathrm{e}},l_{\mathrm{e}}} j(\chi_{n_{\mathrm{e}},l_{\mathrm{e}}} r/b)$—with $j_l(x)$ the spherical Bessel function of order l, $\chi_{n,l}$ the n^{th} zero of $j_l(x)$ and $A_{n_{\mathrm{e}},l_{\mathrm{e}}}$ a normalization constant—and the angular part is given by the spherical harmonics $Y^m_l(\theta,\phi)$. The indices n_{e}, l_{e}, and m_{e} describe the principal,

azimuthal and magnetic quantum numbers of the electron particle-in-a-box wave functions. Corresponding energies are given by the sum of the bulk band gap E_g and a confinement energy:

$$E^\mathrm{e}_{n_\mathrm{e},l_\mathrm{e},m_\mathrm{e}} = E_\mathrm{g} + \frac{\hbar^2 \chi^2_{n_\mathrm{e},l_\mathrm{e}}}{2m_\mathrm{e}a^2}, \tag{7}$$

with m_e the electron effective mass. The probability density for the hole is approximated by a delta function centered around the hole localization site $\mathbf{r}_\mathrm{loc}$:

$$\left|\psi^\mathrm{h}(\mathbf{r}_\mathrm{h})\right|^2 = \delta(\mathbf{r}_\mathrm{h} - \mathbf{r}_\mathrm{loc}). \tag{8}$$

The exciton wave function is the product of the electron and hole single-particle wave functions:

$$\Psi^{(0)}_{n_\mathrm{e},l_\mathrm{e},m_\mathrm{e}}(\mathbf{r}_\mathrm{e},\mathbf{r}_\mathrm{h}) = \psi^\mathrm{e}_{n_\mathrm{e},l_\mathrm{e},m_\mathrm{e}}(\mathbf{r}_\mathrm{e})\,\psi^\mathrm{h}(\mathbf{r}_\mathrm{h}). \tag{9}$$

The radiative recombination rate of the exciton (inverse of the exciton lifetime τ) is proportional to the square of the electron–hole overlap integral:

$$k_\mathrm{decay} \propto \left| \int\int \Psi_{n_\mathrm{e},l_\mathrm{e},m_\mathrm{e}}(\mathbf{r}_\mathrm{e},\mathbf{r}_\mathrm{h})\delta(\mathbf{r}_\mathrm{e}-\mathbf{r}_\mathrm{h})d\mathbf{r}_\mathrm{e}d\mathbf{r}_\mathrm{h} \right|^2 = \left| \sum_{n_\mathrm{e},l_\mathrm{e},m_\mathrm{e}} c_{n_\mathrm{e},l_\mathrm{e},m_\mathrm{e}}\, \psi^\mathrm{e}_{n_\mathrm{e},l_\mathrm{e},m_\mathrm{e}}(\mathbf{r}_\mathrm{loc}) \right|^2, \tag{10}$$

and the energy of the exciton ground state is found using the Hamiltonian matrix H:

$$E_\mathrm{exciton} = \langle\Psi|H|\Psi\rangle\,, \tag{11}$$

$$H = H^\mathrm{e}_0(\mathbf{r}_\mathrm{e}) + V_\mathrm{C}(\mathbf{r}_\mathrm{e},\mathbf{r}_\mathrm{h}) - eV_\mathrm{ext}(\mathbf{r}_\mathrm{e}) + eV_\mathrm{ext}(\mathbf{r}_\mathrm{loc}). \tag{12}$$

Here, $H^\mathrm{e}_0(\mathbf{r}_\mathrm{e})$ are the eigenvalues of spherical particle-in-a-box electron wave functions, $V_\mathrm{C}(\mathbf{r}_\mathrm{e},\mathbf{r}_\mathrm{loc})$ is the electron–hole interaction potential, and V_ext is the external potential. To calculate these Coulomb energies, the CIS/CdS core/shell quantum dot is approximated as a homogeneous dielectric with permittivity ϵ in a medium with permittivity $\epsilon_\mathrm{medium} = 2$.

The electron–hole potential has the form

$$V_\mathrm{C}(\mathbf{r}_\mathrm{e},\mathbf{r}_\mathrm{h}) = \frac{e^2}{4\pi\epsilon\epsilon_0}\left[-\frac{1}{|\mathbf{r}_\mathrm{e}-\mathbf{r}_\mathrm{h}|} + \frac{1}{2}P(\mathbf{r}_\mathrm{e},\mathbf{r}_\mathrm{e}) + \frac{1}{2}P(\mathbf{r}_\mathrm{h},\mathbf{r}_\mathrm{h}) - P(\mathbf{r}_\mathrm{e},\mathbf{r}_\mathrm{h})\right], \tag{13}$$

The electron–hole potential can be decomposed into a direct electron–hole interaction (first term) and indirect interactions with image charges that exist as a result of the dielectric contrast between the nanocrystal and the surrounding medium (second, third and fourth term). The direct interaction describes the attraction between the electron and hole (drawing the electron towards the hole localization site), while the indirect contribution describes the effect that charge carriers are attracted towards the point of highest dielectric stabilization (i.e. the center of the nanocrystal).

The function $P(\mathbf{r}_1,\mathbf{r}_2)$ is given by

$$P(\mathbf{r}_1,\mathbf{r}_2) = \sum_{s=0}^{\infty} \alpha_s\, \frac{r_1^s r_2^s}{a^{2s+1}}\, P_s(\cos\zeta), \tag{14}$$

with $\alpha_s = \big[(\gamma-1)(s+1)\big]/\big[\epsilon\,(\gamma s + s + 1)\big]$, $\gamma = \epsilon/\epsilon_\mathrm{medium}$, and P_s the s^th Legendre polynomial of the cosine of the angle between $\mathbf{r}_1$ and $\mathbf{r}_2$.[18–20]

The operator for the direct electron–hole potential can be expressed in terms of spherical harmonics using a multipole expansion:

$$\frac{1}{|\mathbf{r}_\mathrm{e}-\mathbf{r}_\mathrm{h}|} = \sum_{q=0}^{\infty}\sum_{p=-q}^{q} \frac{4\pi}{2q+1}\frac{\min(r_\mathrm{e},\, r_\mathrm{h})^q}{\max(r_\mathrm{e},\, r_\mathrm{h})^{q+1}} Y^p_q(\theta_\mathrm{e},\phi_\mathrm{e})\, Y^{p*}_q(\theta_\mathrm{h},\phi_\mathrm{h}). \tag{15}$$

As a result, the electron–hole interaction integrals can be separated into a radial integral and an angular integral. The radial integrals are solved numerically and have the form

$$\begin{aligned}\int_0^a \int_0^a R^{\mathrm{e}}_{n_1,l_1}(r_{\mathrm{e}})\, R^{\mathrm{e}}_{n_2,l_2}(r_{\mathrm{e}})\, \delta(r_{\mathrm{h}} - r_{\mathrm{loc}})\, \frac{\min(r_{\mathrm{e}},\, r_{\mathrm{h}})^q}{\max(r_{\mathrm{e}},\, r_{\mathrm{h}})^{q+1}} r_{\mathrm{e}}^2\, dr_{\mathrm{e}} dr_{\mathrm{h}} \\ = \int_0^a R^{\mathrm{e}}_{n_1,l_1}(r_{\mathrm{e}})\, R^{\mathrm{e}}_{n_2,l_2}(r_{\mathrm{e}})\, \frac{\min(r_{\mathrm{e}},\, r_{\mathrm{loc}})^q}{\max(r_{\mathrm{e}},\, r_{\mathrm{loc}})^{q+1}} r_{\mathrm{e}}^2\, dr_{\mathrm{e}}\end{aligned} \tag{16}$$

The angular integrals contain the spherical harmonics and are of the form:

$$\begin{aligned}I_{l_1,m_1,l_2,m_2} = \int_0^{2\pi}\int_0^{\pi}\int_0^{2\pi}\int_0^{\pi} \sum_{q=0}^{\infty}\sum_{p=-q}^{q} \frac{4\pi}{2q+1} Y_{l_1}^{m_1}(\theta_{\mathrm{e}},\phi_{\mathrm{e}}) Y_{l_2}^{m_2 *}(\theta_{\mathrm{e}},\phi_{\mathrm{e}}) \delta(\theta_{\mathrm{h}} - \theta_{\mathrm{loc}}) \delta(\phi_{\mathrm{h}} - \phi_{\mathrm{loc}}) \\ Y_q^p(\theta_{\mathrm{e}},\phi_{\mathrm{e}}) Y_q^{p*}(\theta_{\mathrm{h}},\phi_{\mathrm{h}}) \sin(\theta_{\mathrm{e}})\, d\theta_{\mathrm{e}} d\phi_{\mathrm{e}} d\theta_{\mathrm{h}} d\phi_{\mathrm{h}}.\end{aligned} \tag{17}$$

Using the 3-j symbols,

$$\begin{aligned}\int_0^{2\pi}\int_0^{\pi} Y_{l_1}^{m_1}(\theta,\phi)\, Y_{l_2}^{m_2}(\theta,\phi)\, Y_{l_3}^{m_3}(\theta,\phi) \sin(\theta)\, d\theta\, d\phi \\ = \sqrt{\frac{(2l_1+1)(2l_2+1)(2l_3+1)}{4\pi}} \begin{pmatrix} l_1 & l_2 & l_3 \\ 0 & 0 & 0 \end{pmatrix} \begin{pmatrix} l_1 & l_2 & l_3 \\ m_1 & m_2 & m_3 \end{pmatrix},\end{aligned} \tag{18}$$

and

$$Y_l^{m*}(\theta,\phi) = (-1)^m\, Y_l^{-m}(\theta,\phi), \tag{19}$$

the angular integrals can be simplified to

$$\begin{aligned}I_{l_1,m_1,l_2,m_2} = \sum_{q=0}^{\infty}\sum_{p=-q}^{q} \frac{4\pi}{2q+1} (-1)^{m_2}\, Y_q^{p*}(\theta_{\mathrm{loc}},\phi_{\mathrm{loc}}) \\ \sqrt{\frac{(2l_1+1)(2l_2+1)(2q+1)}{4\pi}} \begin{pmatrix} l_1 & l_2 & q \\ 0 & 0 & 0 \end{pmatrix} \begin{pmatrix} l_1 & l_2 & q \\ m_1 & -m_2 & p \end{pmatrix}.\end{aligned} \tag{20}$$

Defining the hole localization site to be along the z-axis, combined with the relation $P_s(\cos\zeta) = \sqrt{4\pi/(2s+1)}\, Y_l^0(\theta,\phi)$, the contribution of indirect electron–hole interactions can be calculated using a similar mathematical procedure.

We approximate that external charges generate a homogeneous electric field $\mathbf{F}$ (see Figure S4), giving rise to an electrostatic potential

$$V_{\mathrm{ext}}(\mathbf{r}) = \mathbf{F} \cdot \mathbf{r}. \tag{21}$$

Perturbation theory

Neglecting all electron–hole interactions, the lowest-energy electron wave function is the 1S particle-in-a-box function. Here, we account for the electron–hole potential (eq 13) using a first-order correction to the exciton energy (this is a good approximation; see below). The impact of the hole localization site on the exciton energy and lifetime are shown in Figure S5a,b (black circles). Hole localization on a site *away from the center* of the nanocrystal results in a relatively high exciton energy (weak electron–hole attraction) and slow recombination (small electron–hole overlap). Conversely, localization *close to the center* results in a low exciton energy and fast recombination.

We consider the effect of an external electric field up to a second-order correction:

$$E_0 = E_0^{(0)} + \langle \Psi_0^{(0)} | V_{\text{ext}} | \Psi_0^{(0)} \rangle + \sum_i \frac{\left| \langle \Psi_0^{(0)} | V_{\text{ext}} | \Psi_i^{(0)} \rangle \right|^2}{E_0^{(0)} - E_i^{(0)}}. \tag{22}$$

Here, $E_0^{(0)}$ is the sum of confinement (second term in eq 7) and electron–hole interaction (eq 13, calculated up to first order) energies:

$$E_0^{(0)} = E_{1,0,0}^{\text{e}} + \langle \Psi_0^{(0)} | V_{\text{C}} | \Psi_0^{(0)} \rangle \,. \tag{23}$$

The first-order contribution of the electric field evaluates to

$$\langle \Psi_0^{(0)} | V_{\text{ext}} | \Psi_0^{(0)} \rangle = \mathbf{p} \cdot \mathbf{F}, \tag{24}$$

with the internal dipole moment defined as

$$\mathbf{p} = e\big(\mathbf{r}_{\text{loc}} - \mathbf{r}_0\big) \tag{25}$$

and $\mathbf{r}_0$ the center of the nanocrystal. The major contribution to the second-order correction originates from mixing with the 1P state. Neglecting contributions from other odd-parity states, the second-order term can be expressed as

$$\sum_i \frac{\left| \langle \Psi_0^{(0)} | V_{\text{ext}} | \Psi_i^{(0)} \rangle \right|^2}{E_0^{(0)} - E_i^{(0)}} = -\frac{1}{2}\, \alpha F^2, \tag{26}$$

with the polarizability $\alpha = 0.036 m_{\text{e}} e^2 a^4 / \hbar^2$. The second-order correction to the energy of the exciton is small compared to the first-order correction, as the polarizability of the electron is small and the intrinsic dipole moment of the exciton can be very large. The effect of polarizability on the exciton energy only becomes apparent when the projection of the exciton dipole moment in the direction of the electric field is (approximately) zero, or when field become very strong (i.e. the quadratic term dominates over the linear term). The range of fields studied here roughly corresponds to the scenario in which two elementary charges of opposite sign reside on either side of the quantum dot (see above). The results are shown in Figure S5e,f (black dashed lines).

Variational theory
With a variational approach, we can optimize the coefficients $c_{n_\mathrm{e},l_\mathrm{e},m_\mathrm{e}}$ of the wave function of the exciton ground state (eq 5, 10) by minimizing the exciton energy:

$$E_\mathrm{exciton} = \langle \Psi | H | \Psi \rangle \,. \tag{27}$$

80 basis functions were used to achieve convergence, with quantum numbers $n_\mathrm{e} = \{1, 2, \ldots, 5\}$, $l_\mathrm{e} = \{1, 2, 3\}$ and $m_\mathrm{e} = \{-3, -2, \ldots, +2, +3\}$.

The results of this variational approach (solid lines in Figure S5e,f) differ slightly from the simple model as predicted by perturbation theory. The most important discrepancies are that:

- perturbation theory overestimates the the exciton dipole moment
- perturbation theory overestimates the polarizability of the exciton

Both discrepancies originate from the fact that in our second-order perturbation description of the impact of an external field, the effect of the hole on the electron wave function is neglected: attraction of the electron wave function to the localized hole decreases the dipole moment (the electron is pulled towards the hole) of the exciton as well as the polarizability of the exciton (electron–hole attraction attraction that opposes polarization of the electron cloud by an external field). The effective dipole moments calculated in the absence of an external electric field are in good agreement with the slopes found in Figure S5e. The corresponding electron charge densities are depicted in Figure S5c,d, for a hole localized in the center or $0.5a$ away from the center, respectively. Similarly, the polarizabilities as expected from second-order perturbation theory are equivalent to what we find using variational theory without taking into account electron–hole interactions (compare red and black dashed lines in Figure S5f).

Estimation of polarizability from model
To obtain the polarizability in units of volume, we use the relationship $\alpha = 0.036 m_\mathrm{e} e^2 a^4 / \hbar^2$. For $a = 1.5$ nm, and $m_\mathrm{e} = 0.153 m_0$, $\alpha/(4\pi\epsilon_0) = 5 \cdot 10^2$ Å^3, with m_0 the electron rest mass.

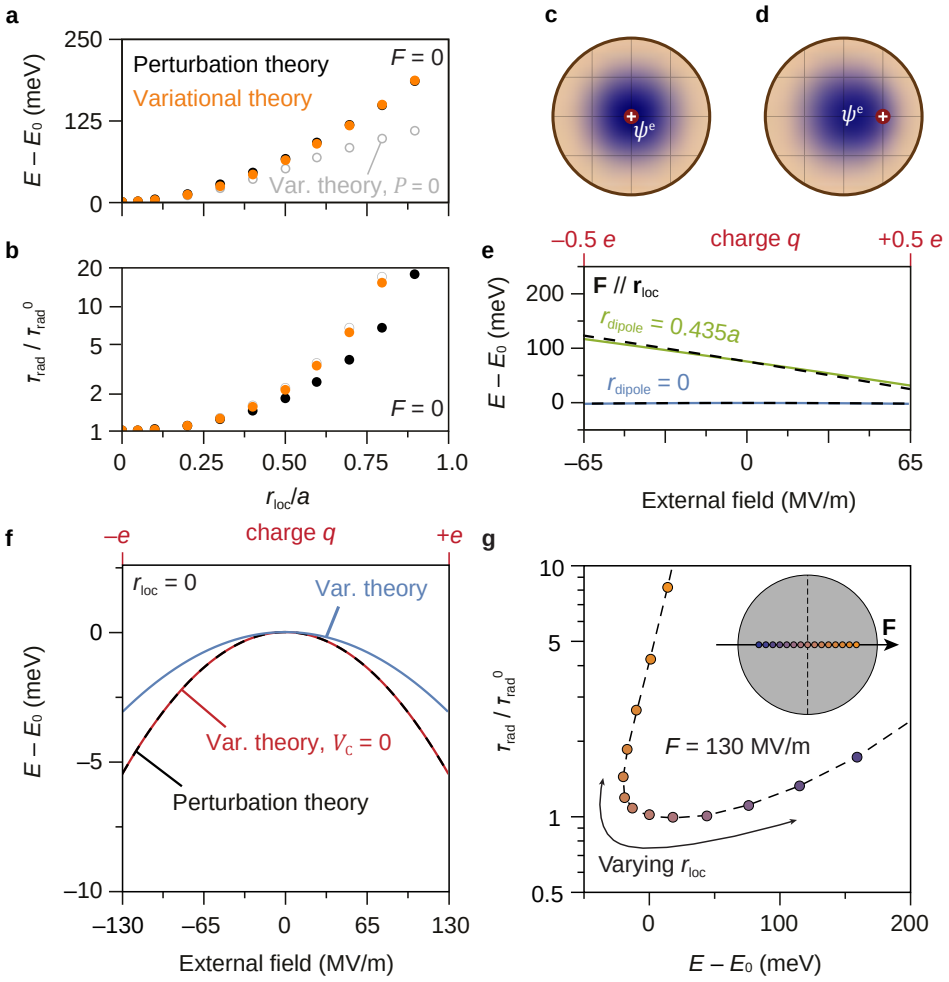

Figure S5 — Impact of the hole localization site and the quantum-confined Stark effect. **(a,b)** Exciton energy E, relative to the reference exciton energy E_0, and lifetimes (inverse of the radiative recombination rate of the exciton) relative to the reference lifetime τ_0, calculated using a variational approach with 80 basis functions (orange) and a first-order perturbation description of the electron–hole interaction potential U_{eh} (black), in absence of an external electric field. E_0 and τ_0 correspond to the exciton energy and lifetime in the situation where $r_{\mathrm{loc}} = 0$ and $F = 0$. The grey circles correspond to the same calculation as the orange circles, but without a contribution of indirect electron–hole interactions (second, third and fourth term in eq 13). **(c,d)** 2-Dimensional representations of the electron charge density (blue) in the absence of an electric field, calculated using the variational approach for a hole localization site in the center of the particle and at $r_{\mathrm{loc}} = 0.5a$ away from the center. Hole positions are indicated by the red circles. **(e)** Influence of a weak electric field oriented parallel to $\mathbf{r}_{\mathrm{loc}}$, with the hole localization site in the center (blue), or $0.5a$ away from the center in the direction of the external electric field (green). The solid lines indicate the result of the variational approach; black dashed lines are calculated treating the external field as a second-order perturbation (eq 22). The slope corresponds to the effective dipole moment. **(f)** Influence of a strong electric field, with the hole localization site in the center. The blue solid line represents the result of the variational approach. The red line correspond to the same calculation, but with $U_{\mathrm{eh}} = 0$. The black dashed line are calculated treating the external field as a second-order perturbation (eq 22). **(g)** Correlation between exciton energy and lifetime, calculated using the variational approach in the presence of an electric field of 130 MV/m. The circle colors represent the location of the hole localization site, as indicated in the inset.

Table S1 — Overview of measurements on individual core-only $CuInS_2$ quantum dots. With μ_{tot} the fitted peak energy of the total PL spectrum, $\mathrm{FWHM}_{\mathrm{tot}}$ the fitted full-width-at-half-maximum of the total PL spectrum, $\widetilde{\mathrm{FWHM}}$ the median FWHM of all fitted 'instantaneous' PL spectra, R_μ the spread in μ, the fitted peak position of each 'instantaneous' PL spectrum, and $\langle\tau\rangle$ the mean photon delay time. Here, R_μ is defined as the difference between the 95th and 5th percentile of the fitted μ values. The blinking type abbreviations are: n.d.: blinking mechanism could not be determined, BE: energy loss due to trapping of carriers from the band edge, HCC: energy loss due to trapping of hot charge-carriers, and f: flickering, fluctuations in the PL intensity too fast to resolve experimentally. The total PL spectrum was accumulated for time periods where $I_{\mathrm{tot}} > 2.5$ cts/100 ms. Only instantaneous spectra which were fit well (i.e., only fits where $\sigma_\mu \leq 30$ meV, $\sigma_{\mathrm{FWHM}} \leq 40$ meV and FWHM ≥ 60 meV, with σ_μ the fit error on μ and σ_{FWHM} the fit error on the FWHM) were used to calculate $\widetilde{\mathrm{FWHM}}$ and R_μ. Only 100-ms time periods in which the QD was not OFF (i.e., $I_{\mathrm{tot}} > 15$ cts/100 ms) were used to calculate $\langle\tau\rangle$. See also the corresponding figures in the Extended Data.

CIS QD	μ_{tot} (eV)	$\mathrm{FWHM}_{\mathrm{tot}}$ (meV)	$\widetilde{\mathrm{FWHM}}$ (meV)	R_μ (meV)	$\langle\tau\rangle$ (ns)	Blinking type
1	1.810	226	155	171	–	–
2	1.759	179	154	63	–	–
3	1.802	200	183	93	–	–
4	1.902	206	192	99	–	–
5	1.831	206	186	62	–	–
6	1.535	224	191	83	–	–
7	–	–	–	–	406	BE
8	–	–	–	–	190	BE
9	–	–	–	–	412	BE
10	–	–	–	–	212	f
11	–	–	–	–	284	BE
12	–	–	–	–	369	BE
13	–	–	–	–	260	f
14	–	–	–	–	418	n.d.
15	–	–	–	–	311	BE
16	–	–	–	–	266	HCC

Table S2 — Overview of measurements on individual core/shell $CuInS_2$/CdS quantum dots. Variable definitions are the same as in Table S1. Additionally, abbreviations used to denote the type of spectral diffusion (SD) are: QCSE: spectral diffusion due to the quantum-confined Stark effect, SC: spectral diffusions due to a change in the preferential hole localization site. Similar to Table S1, the total PL spectrum was accumulated only using time periods where the total PL intensity was high (criterium used here: $I_{\mathrm{tot}} > 40$ cts/400 ms). Likewise, $\widetilde{\mathrm{FWHM}}$ and R_μ were calculated using only instantaneous spectra which were fitted well (criterium used here: $\sigma_\mu \leq 40$ meV $\wedge$ $I_{\mathrm{tot}} > 40$ cts/400 ms $\wedge$ FWHM ≥ 60 meV). Finally, only 400-ms time periods where $I_{\mathrm{tot}} > 40$ cts/400 ms were used to calculate $\langle\tau\rangle$. See also the corresponding figures in the Extended Data.

CIS/CdS QD	μ_{tot} (eV)	$\mathrm{FWHM}_{\mathrm{tot}}$ (meV)	$\widetilde{\mathrm{FWHM}}$ (meV)	R_μ (meV)	SD type	$\langle\tau\rangle$ (ns)	Blink. type
1	1.885	191	188	57	–	399	BE
2	2.000	246	248	169	n.d.	554	HCC
3	1.813	167	157	87	n.d.	463	f
4	1.916	158	159	40	–	368	n.d.
5	1.800	174	173	34	–	483	HCC
6	1.871	191	182	90	QCSE	441	f
7	1.824	175	176	41	–	468	f
8	1.837	213	202	104	QCSE	574	f
9	1.759	166	168	53	–	396	f
10	1.960	157	162	58	–	334	f
11	1.831	217	209	95	QCSE	680	HCC
12	1.780	210	211	73	SC	623	BE
13	1.990	170	173	285	QCSE;SC	340	n.d.
14	1.772	191	194	58	–	685	f
15	1.862	472	276	292	QCSE	772	f
16	1.821	197	172	107	SC	575	n.d.
17	1.754	323	256	181	n.d.	639	HCC
18	1.881	184	178	67	–	376	f
19	1.850	253	220	186	QCSE	664	f
20	1.563	238	209	71	–	992	f
21	1.631	182	173	108	n.d.	461	f
22	1.858	197	177	114	QCSE	430	f
23	1.906	173	165	104	QCSE	373	n.d.
24	1.625	176	167	85	n.d.	513	f
25	1.719	218	216	113	n.d.	738	f
26	1.859	185	177	90	–	503	HCC
27	1.902	195	182	70	n.d.	340	BE
28	1.831	168	164	47	–	465	n.d.
29	1.726	167	164	27	–	489	n.d.
30	1.936	223	195	185	–	454	f
31	1.693	448	229	254	QCSE	683	f
32	1.759	297	256	174	QCSE	531	f

Figure E1–E6 — Results of spectrometer experiments for more core-only $CuInS_2$ quantum dots.
Below we provide an overview of results from micro-spectroscopy experiments on core-only $CuInS_2$ quantum dots.

The arrangement of each of these figures is as follows: (**a**) Total photoluminescence (PL) intensity ($I_{\rm tot}$) as a function of time, obtained by integrating each measured PL spectrum over the interval 1.5–2.0 eV. (**b**) PL spectrum as a function of time. The PL intensity is indicated by the color, from black to purple to yellow (low to medium to high). Each of the measured spectra (integration time: 100 ms) was fitted using a symmetric Gaussian peak with a constant background. (**c**) Fitted peak position μ as a function of time (**d**) Fitted full-width-at-half-maximum (FWHM) as a function of time. For clarity, only results from successful fits are displayed (i.e., only fits where $\sigma_\mu \leq 30$ meV and $\sigma_{\rm FWHM} \leq 40$ meV and FWHM ≥ 60 meV, with σ_μ the fit error in μ and $\sigma_{\rm FWHM}$ the fit error in the FWHM). (**e**) The total PL spectrum, obtained as the average of all measured PL spectra where $I_{\rm tot} > 2.5$ cts/100 ms. (**f**) PL spectra of selected time periods in the experiment [colored spectra in (f) correspond to the indicated regions in (a,c,d)]. Symbols in (e,f) are data points. Solid lines in (e) is a fit to an asymmetric Gaussian peak:

$$I_{\rm Gaussian}\left(E, C, A, \mu, \sigma_{\rm B}, \sigma_{\rm R}\right) = \begin{cases} A\exp\left[\frac{-(E-\mu)^2}{2\sigma_{\rm R}^2}\right] + C, & \text{if } E < \mu \\ \\ A\exp\left[\frac{-(E-\mu)^2}{2\sigma_{\rm B}^2}\right] + C, & \text{otherwise} \end{cases}, \tag{1}$$

where E denotes the photon energy, and C, A, μ, $\sigma_{\rm B}$, and $\sigma_{\rm R}$ are the five fit parameters, which are the background intensity, peak amplitude, peak position, high-energy (blue) standard deviation, and the low-energy (red) standard deviation, respectively. Solid lines in (f) are fits to symmetric Gaussian peaks. The values of the relevant fitted parameters are indicated in the respective panels. Dotted lines indicate (c,f) the median μ, (d) the median FWHM, obtained from fitting each individual PL spectrum.

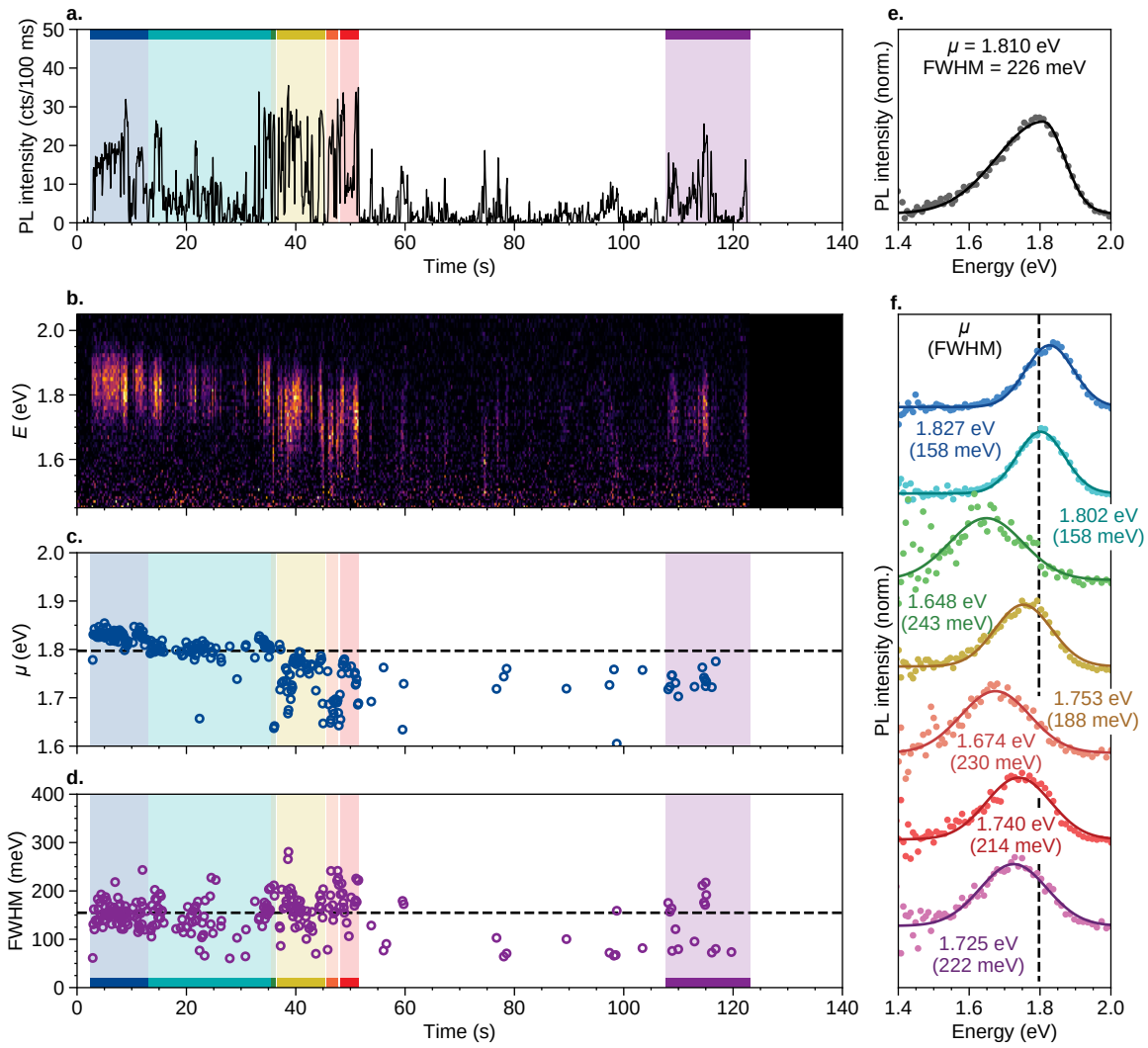

Figure E1 — Results of micro-spectroscopy experiment on core-only $CuInS_2$ quantum dot 1.

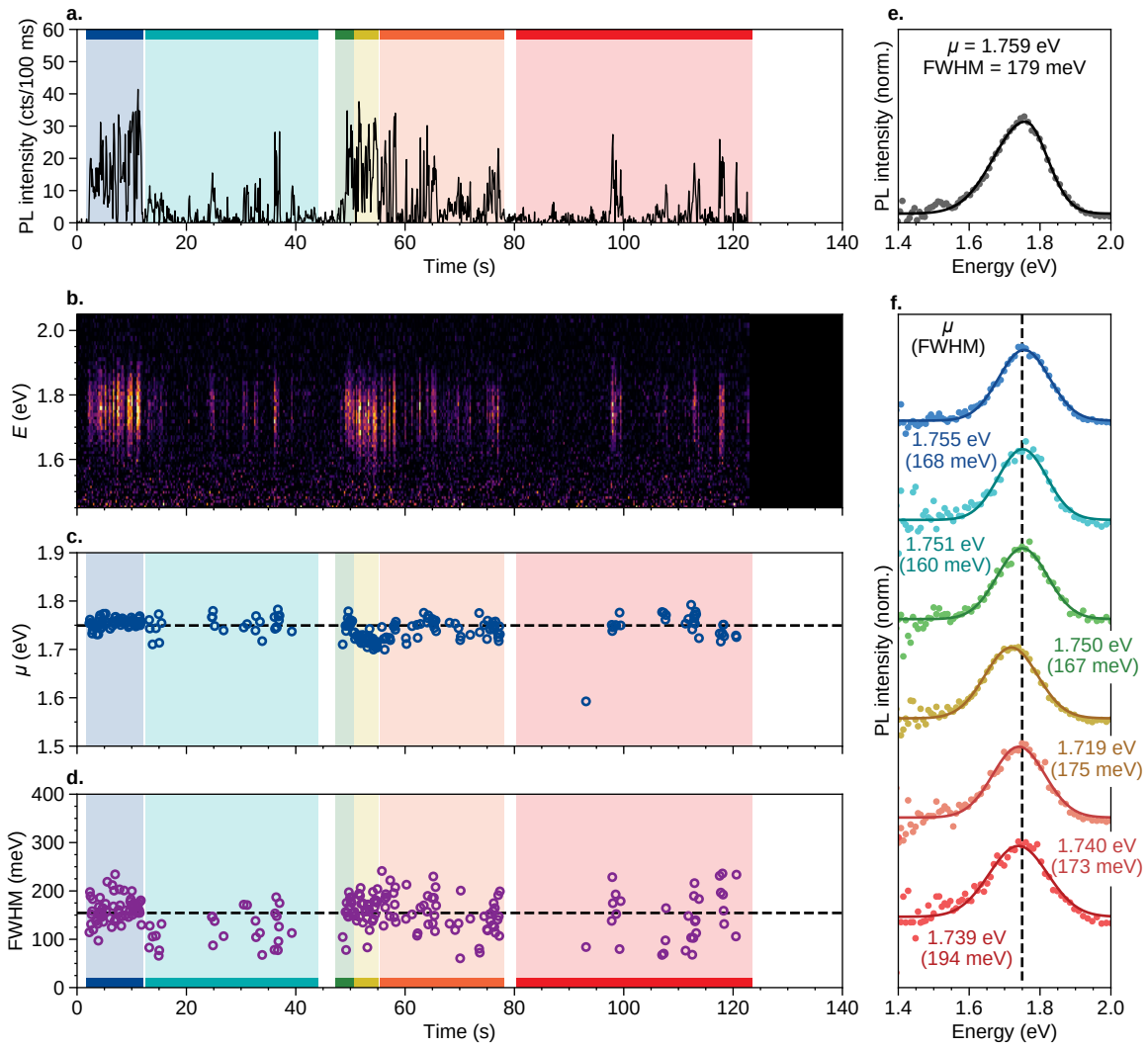

Figure E2 — Results of micro-spectroscopy experiment on core-only $CuInS_2$ quantum dot 2.

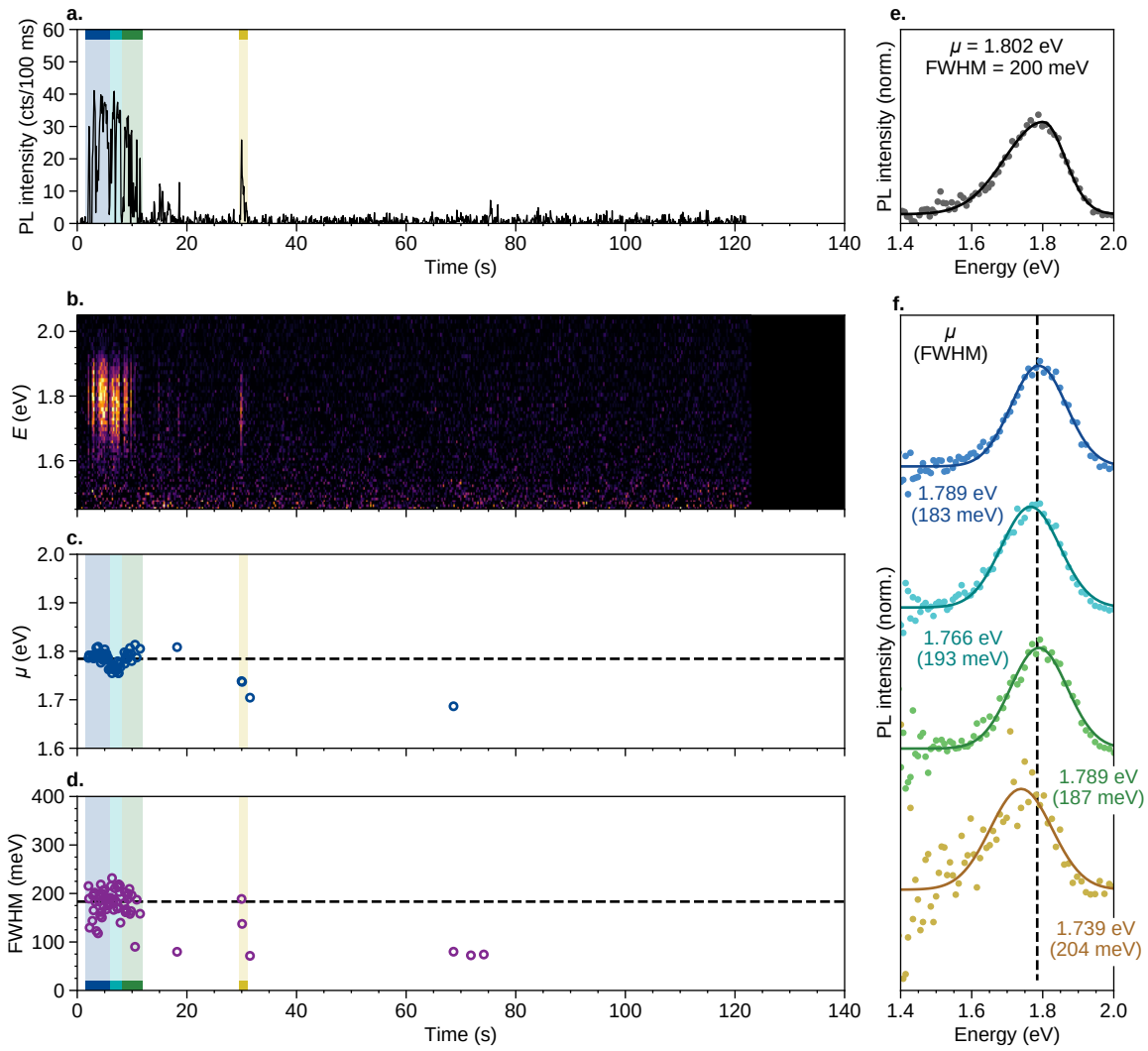

Figure E3 — Results of micro-spectroscopy experiment on core-only $CuInS_2$ quantum dot 3.

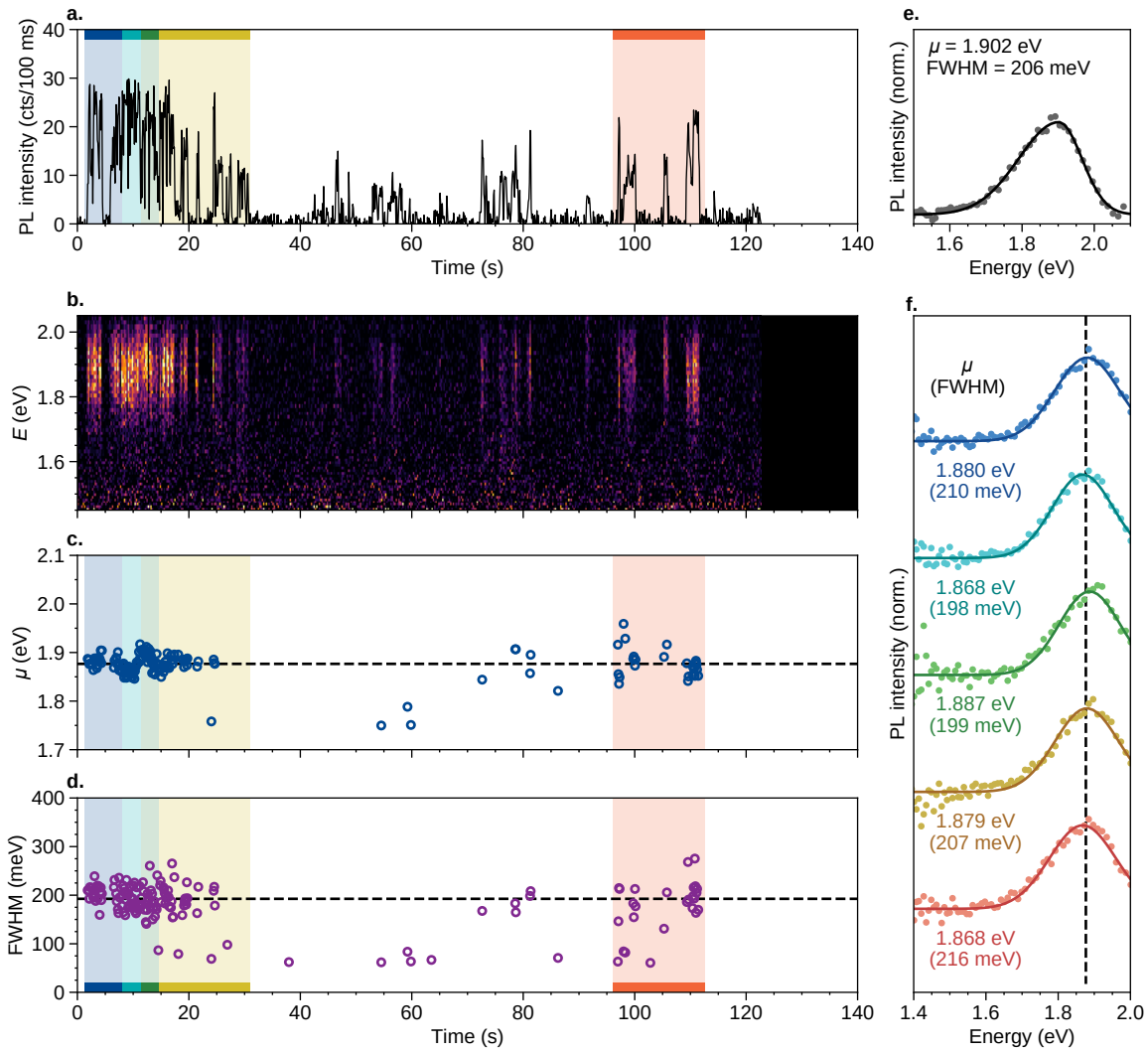

Figure E4 — Results of micro-spectroscopy experiment on core-only $CuInS_2$ quantum dot 4.

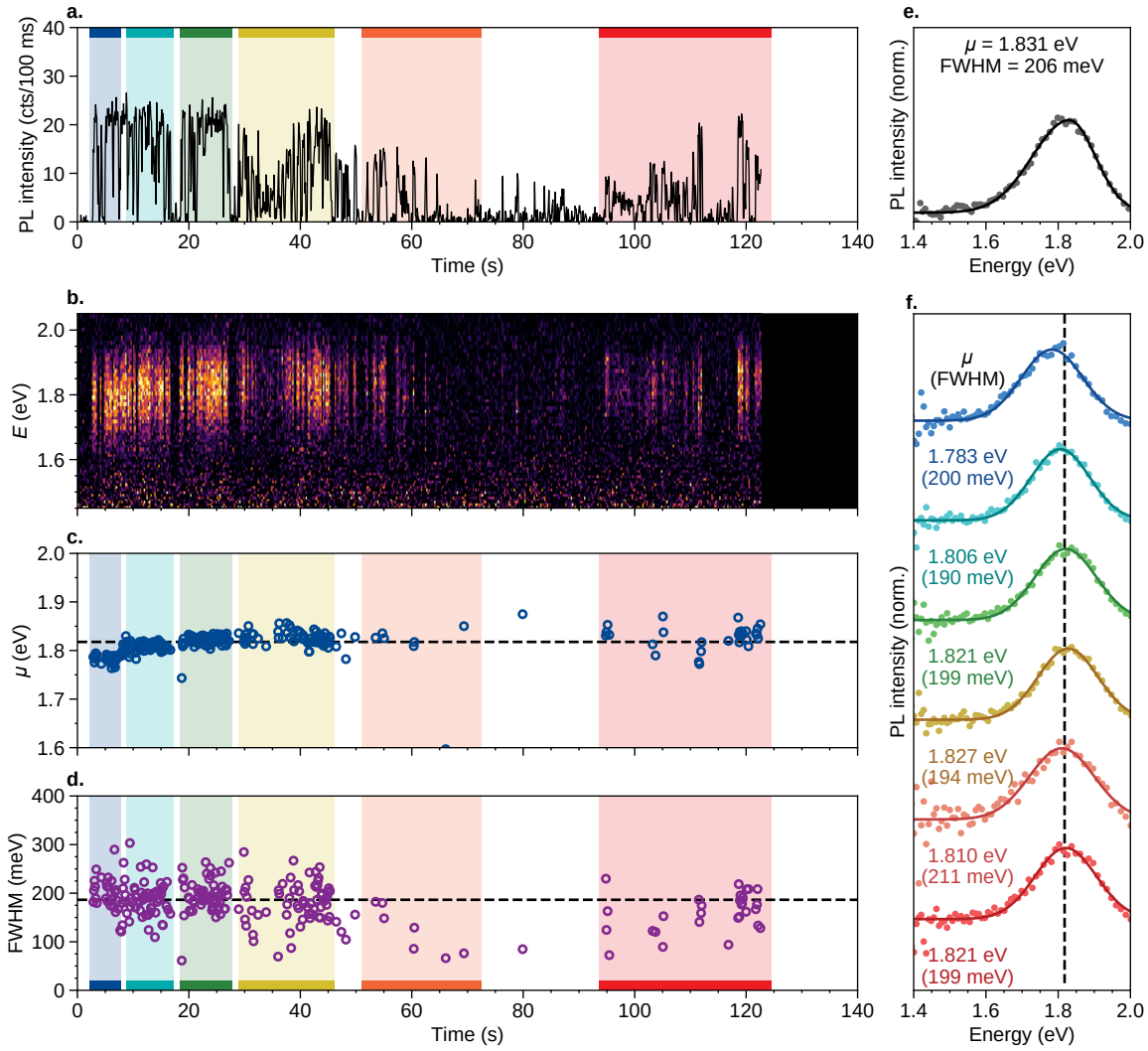

Figure E5 — Results of micro-spectroscopy experiment on core-only $CuInS_2$ quantum dot 5.

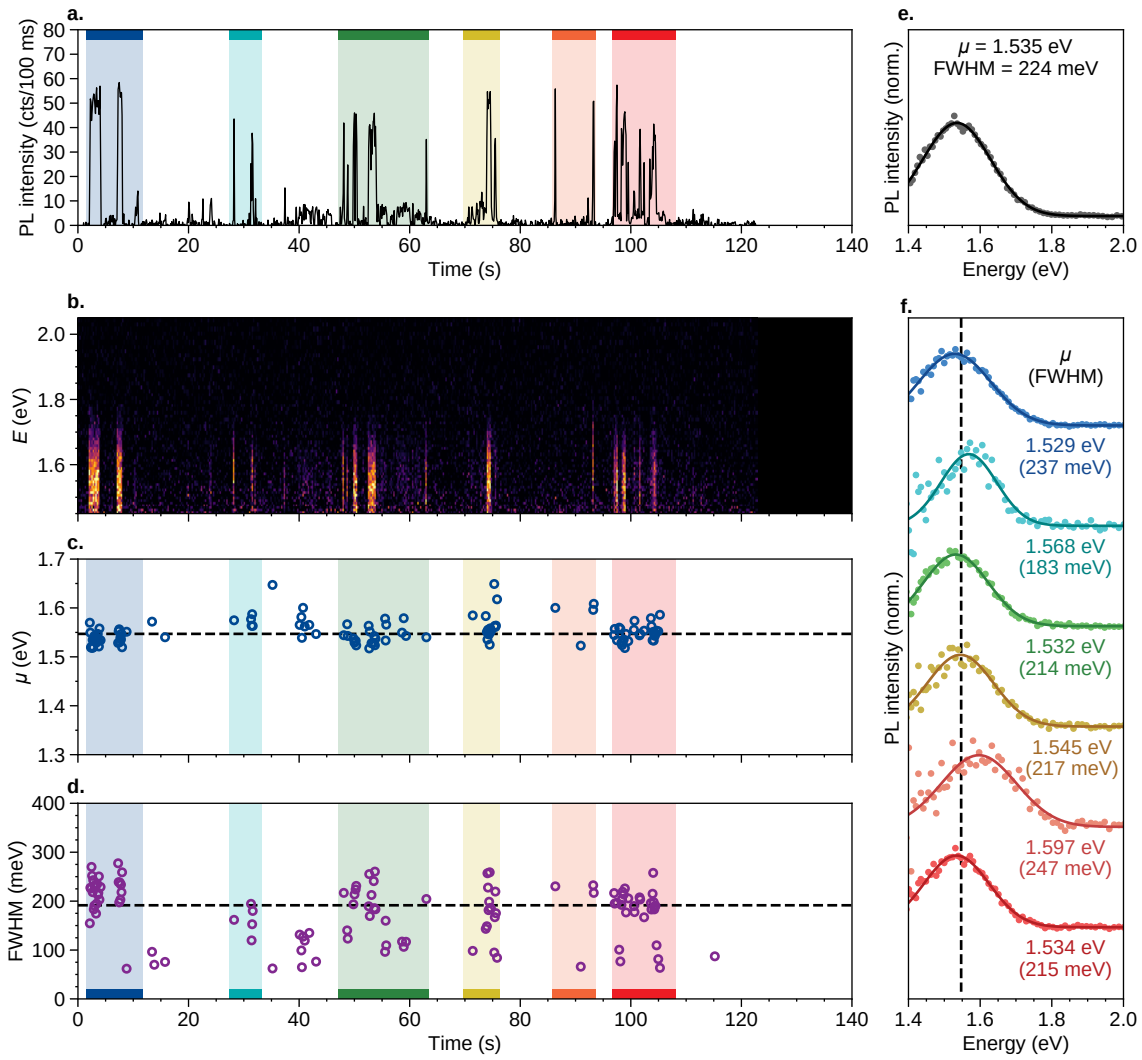

Figure E6 — Results of micro-spectroscopy experiment on core-only $CuInS_2$ quantum dot 6.

Figure E7–E16 — Results of double-APD experiments for more core-only $CuInS_2$ quantum dots.
Below we provide an overview of results from time-correlated single-photon counting experiments, using two avalanche photon diodes (APDs) in Hanbury Brown–Twiss configuration, on core-only $CuInS_2$ quantum dots.

The arrangement of each of these figures is as follows: (**a**) Total photoluminescence (PL) intensity ($I_{\rm tot}$) as a function of time. (**b**) The average photon delay time $\langle\tau\rangle$ for each 100-ms period in the experiment. To minimize contributions from background signal, only photons with delay times $\leq 1.6\mu$s were considered. For clarity, only data points where $I_{\rm tot} \geq 15$ cts/100 ms are displayed. (**c**) Second-order correlation function. (**d**) Total PL decay curve, constructed from time periods where $I_{\rm tot} \geq 15$ cts/100 ms. The total average photon delay time $\langle\tau\rangle$, calculated from this decay curve, without additional time gating, is indicated. (**e**) Two-dimensional fluorescence lifetime–PL intensity histogram. Occurrence is indicated by the color, from black to purple to yellow (low to medium to high). (**f**) PL decay curves constructed for (blue) GREY, (red) ON periods, by selecting time periods with low or high $I_{\rm tot}$, respectively. The intensity ranges that contribute to these two curves are indicated by the colored boxes in panel (e). Symbols are data points, lines are fits to single-exponential decay with a constant background.

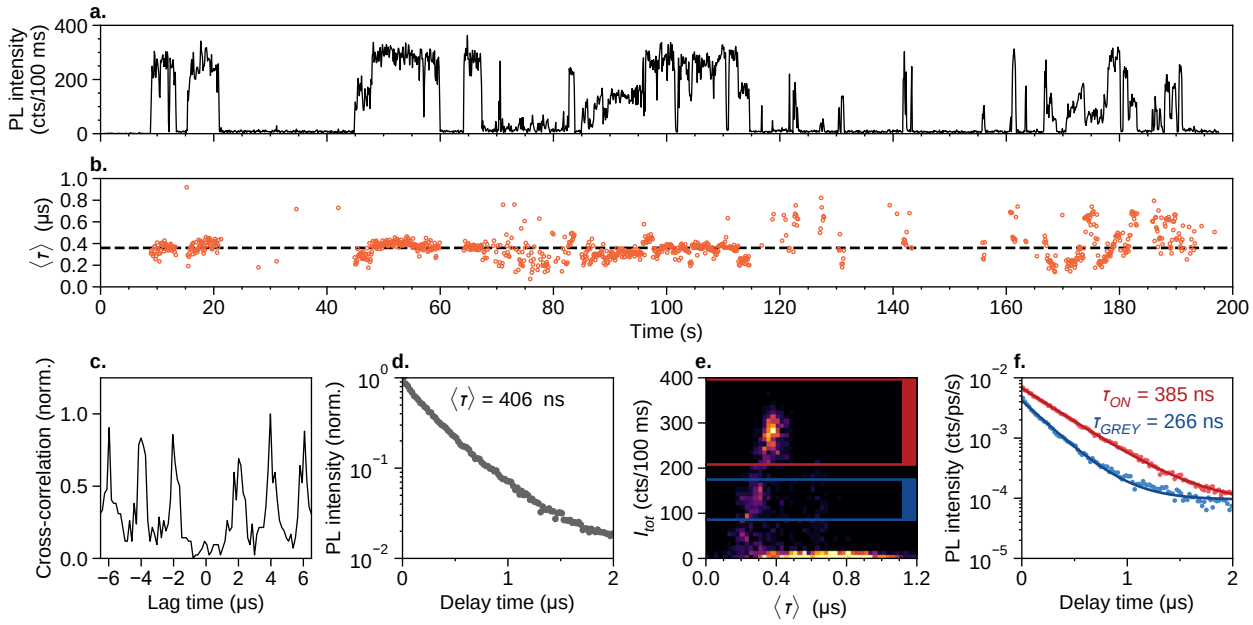

Figure E7 — Results of double-APD experiment on core-only $CuInS_2$ quantum dot 7.

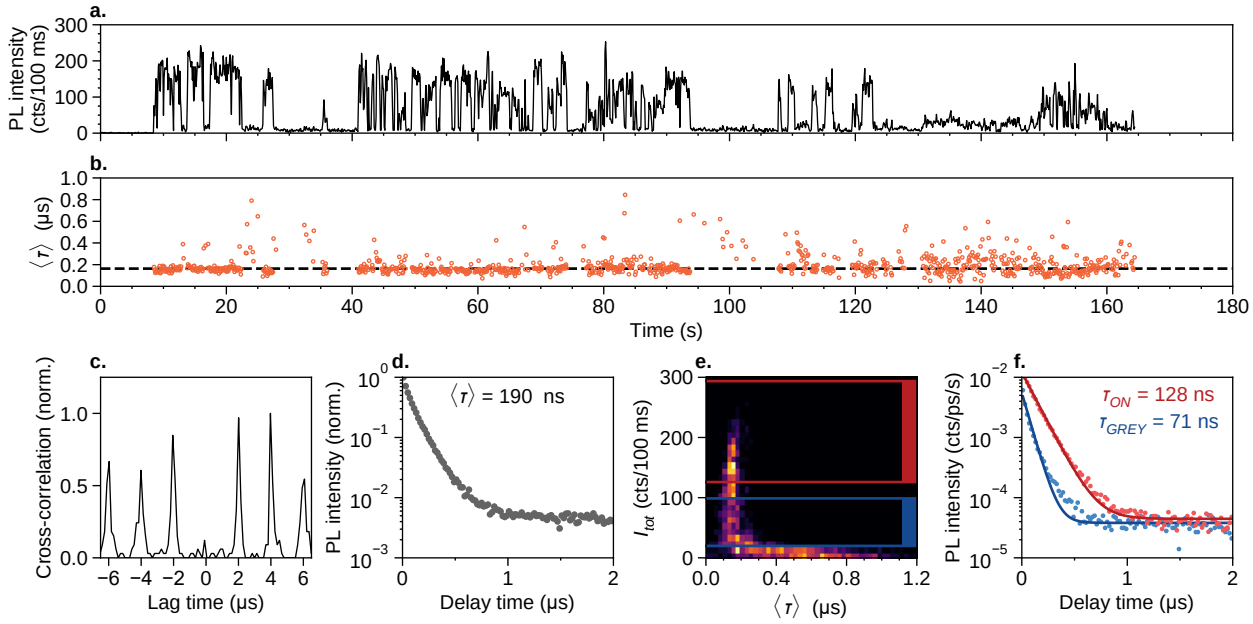

Figure E8 — Results of double-APD experiment on core-only $CuInS_2$ quantum dot 8.

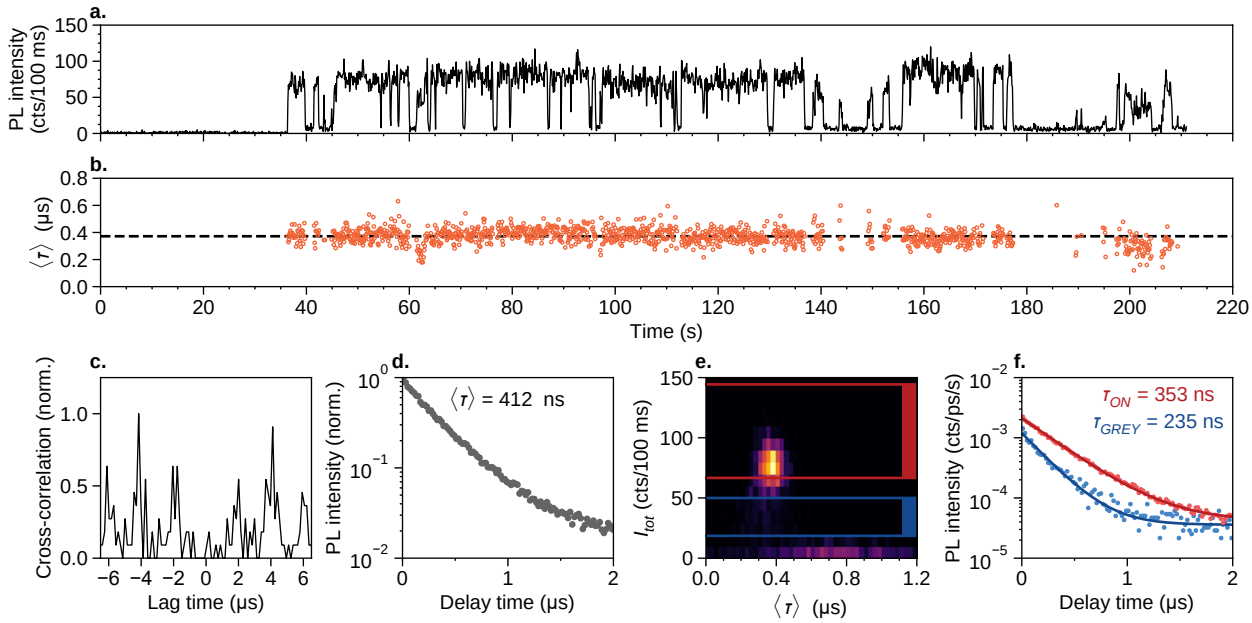

Figure E9 — Results of double-APD experiment on core-only $CuInS_2$ quantum dot 9.

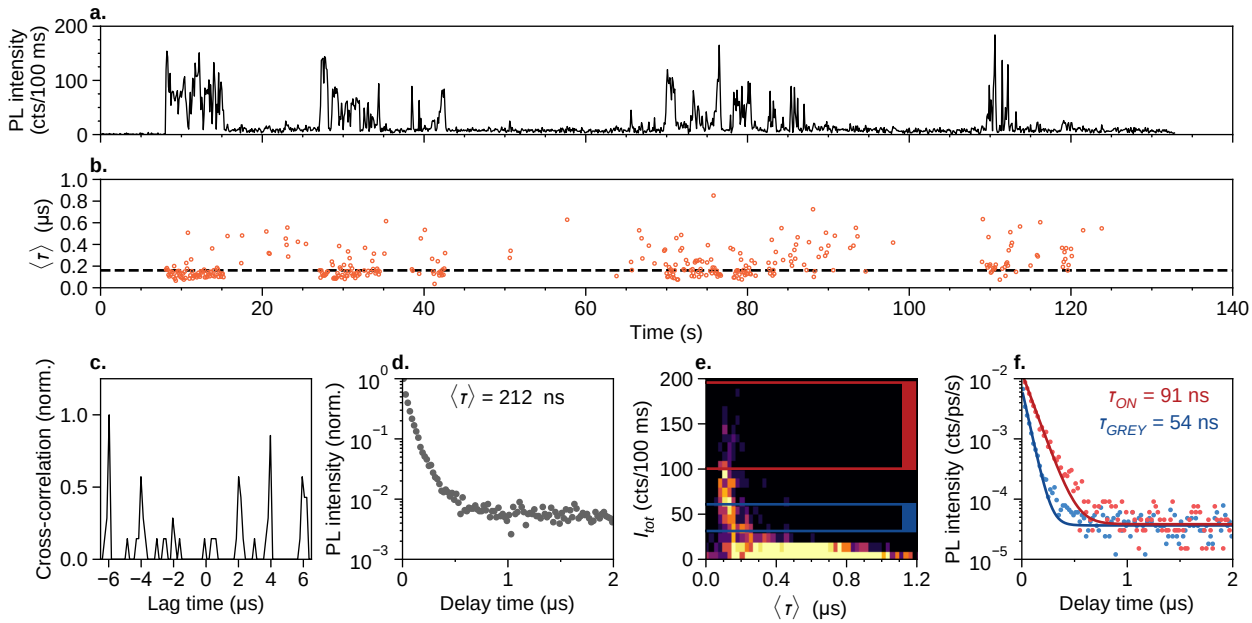

Figure E10 — Results of double-APD experiment on core-only $CuInS_2$ quantum dot 10.

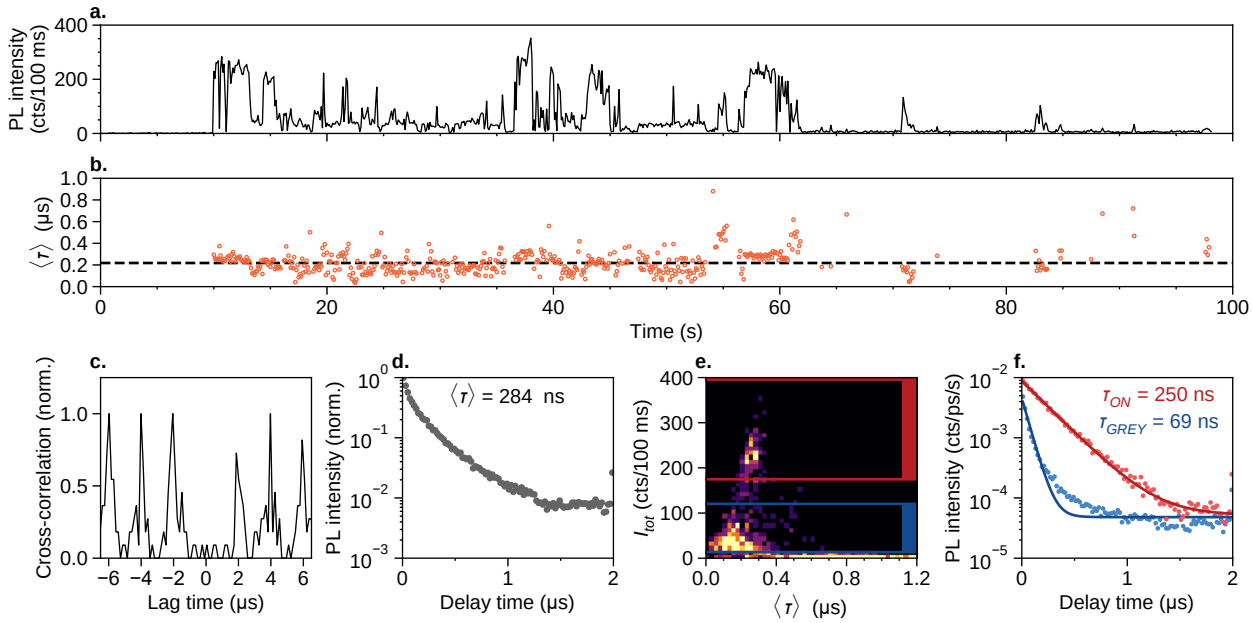

Figure E11 — Results of double-APD experiment on core-only $CuInS_2$ quantum dot 11.

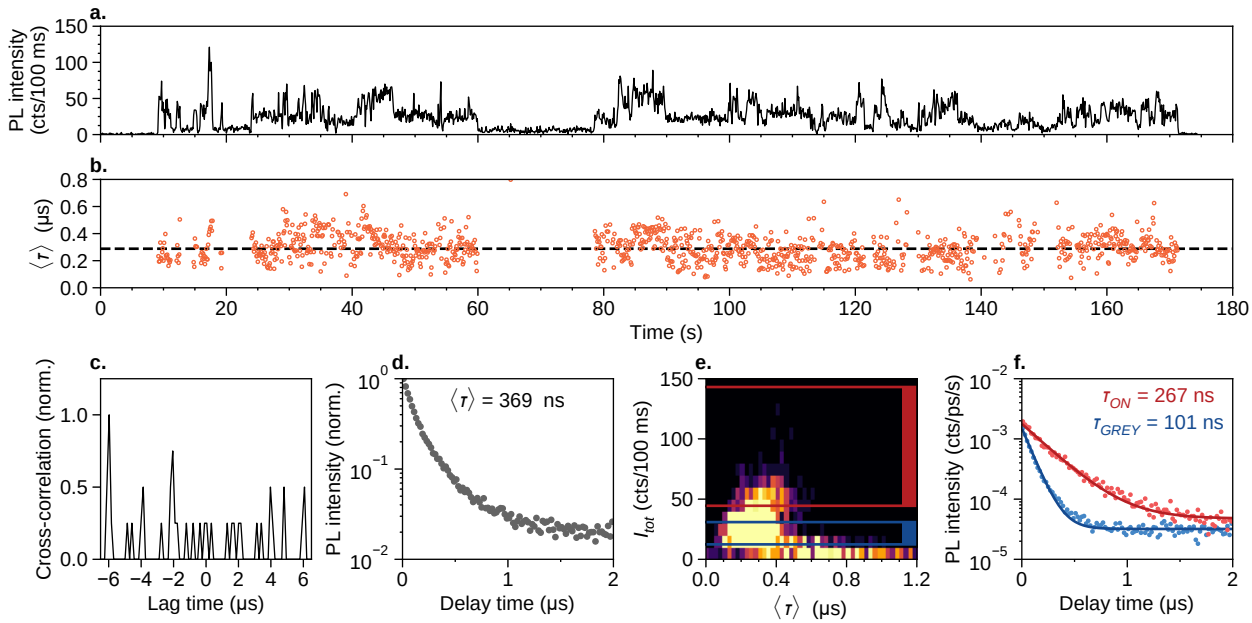

Figure E12 — Results of double-APD experiment on core-only $CuInS_2$ quantum dot 12.

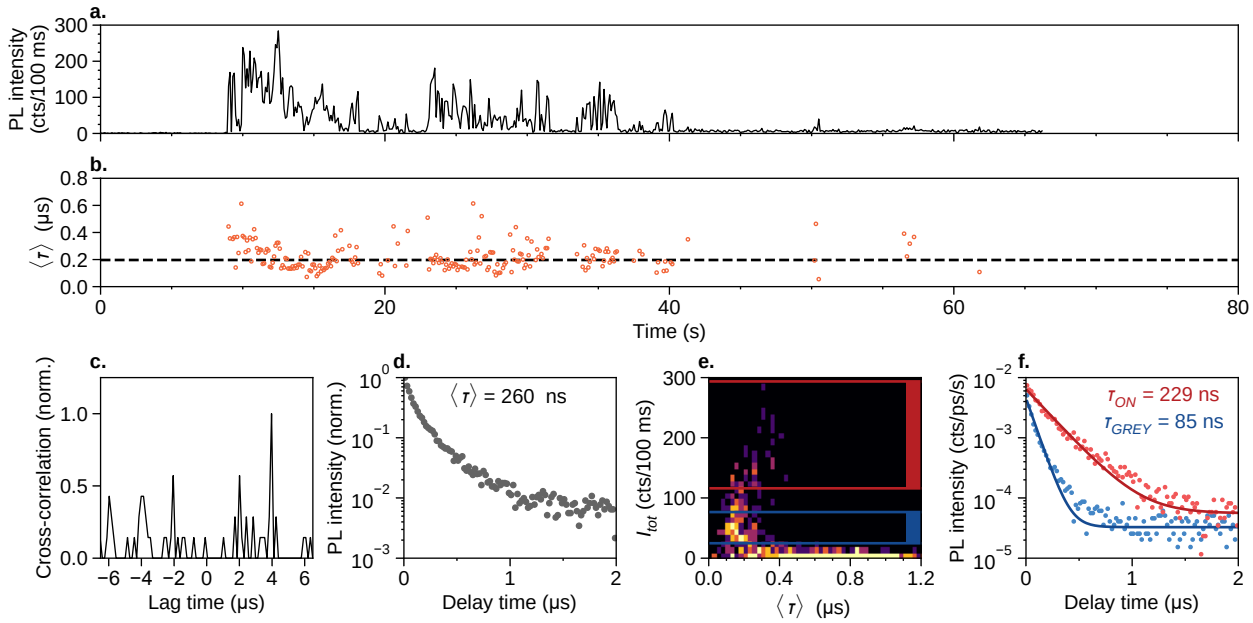

Figure E13 — Results of double-APD experiment on core-only $CuInS_2$ quantum dot 13.

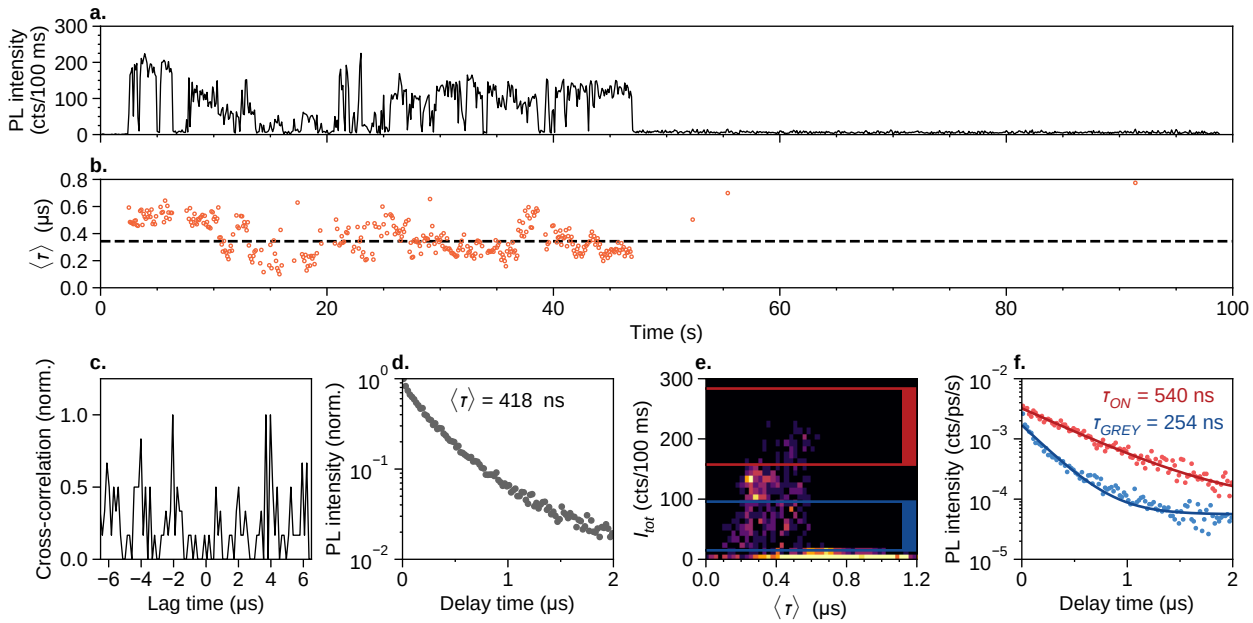

Figure E14 — Results of double-APD experiment on core-only $CuInS_2$ quantum dot 14.

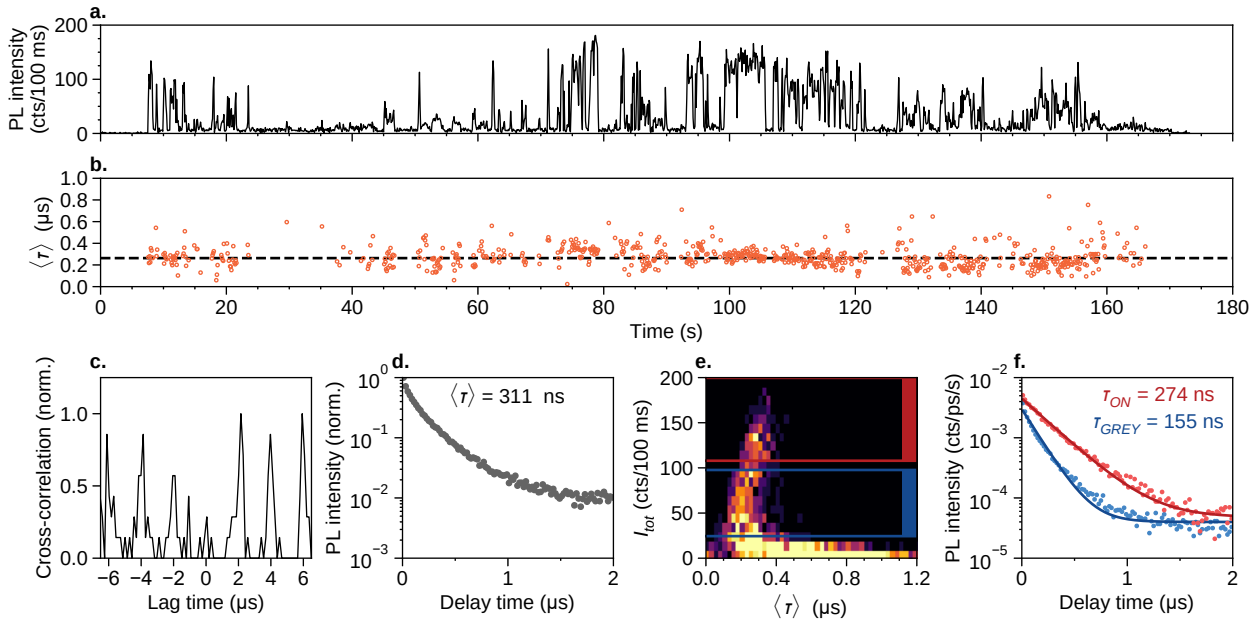

Figure E15 — Results of double-APD experiment on core-only $CuInS_2$ quantum dot 15.

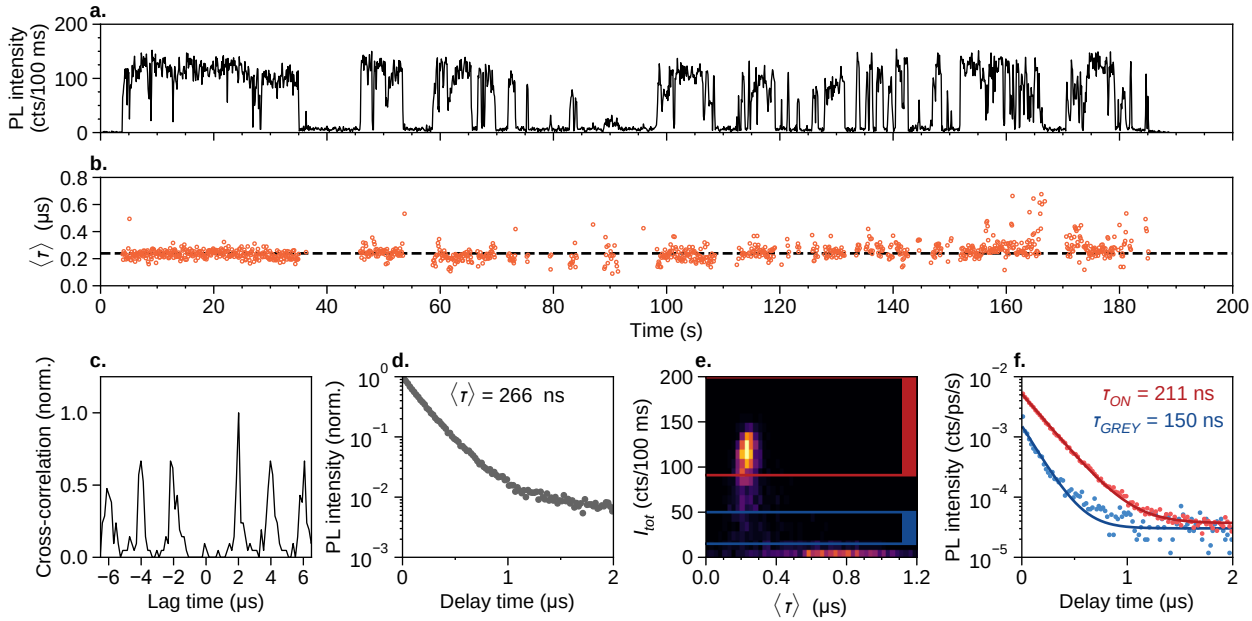

Figure E16 — Results of double-APD experiment on core-only $CuInS_2$ quantum dot 16.

Figure E17–E48 — Results of measurements for more core/shell $CuInS_2$/CdS quantum dots.
Below we provide an overview of results from hybrid time-correlated single-photon counting and PL spectroscopy experiments on core/shell $CuInS_2$/CdS quantum dots.

The arrangement of each of these figures is as follows: (**a**) Total photoluminescence (PL) intensity (I_{tot}) as a function of time. (**b**) The total PL spectrum, obtained as the average of all measured PL spectra where $I_{\mathrm{tot}} > 40$ cts/400 ms. (**c**) The total PL decay curve, constructed for all time periods where $I_{\mathrm{tot}} > 40$ cts/400 ms. The average photon delay time $\langle\tau\rangle$, calculated from this decay curve without additional time gating, is indicated. (**d**) PL spectrum as a function of time. The PL intensity is indicated by the color, from black to purple to yellow (low to medium to high). Each of the measured spectra (integration time: 400 ms) was fitted using a symmetric Gaussian peak with a constant background. (**e**) Fitted peak position μ as a function of time. (**f**) Fitted FWHM as a function of time. (**g**) The average photon delay time $\langle\tau\rangle$ for each 400-ms period in the experiment. To minimize contributions from background signal, only photons with delay times $\leq 3\mu$s were considered. (**h**) PL spectra of selected time periods in the experiment. (**i**) PL decay curves, constructed from selected time periods in the experiment. Colors in (h,i) indicate the time period over which the data was collected; these regions are indicated by the same colors in panels (a,e–g). (**j**) Second-order correlation function, measured using two APDs in Hanbury Brown–Twiss configuration, prior to the hybrid APD–spectrometer experiment. (**k**) Two-dimensional fluorescence lifetime–PL intensity histogram. Occurrence is indicated by the color, from black to purple to yellow (low to medium to high). (**l**) Correlation between $\langle\tau\rangle$ and fitted PL peak position μ. (**m**) Correlation between I_{tot} and fitted PL peak position μ. In (l,m), each symbol corresponds to a 400-ms period in the experiment, and the color (blue to green to yellow) indicates time. For clarity, in (e–g,l,m) only results for time periods where the PL spectrum was fitted successfully are displayed (i.e., only when $\sigma_\mu \leq 40$ meV and $\sigma_{\mathrm{FWHM}} \leq 80$ meV and FWHM ≥ 60 meV). Symbols in (b,h,i) are data points, solid lines are: (b) a fit to an asymmetric Gaussian peak (see Equation 1), (h) symmetric Gaussians with a constant background, and (i) single-exponential decay with a constant background. The values of relevant fitted parameters are indicated in the respective panels.

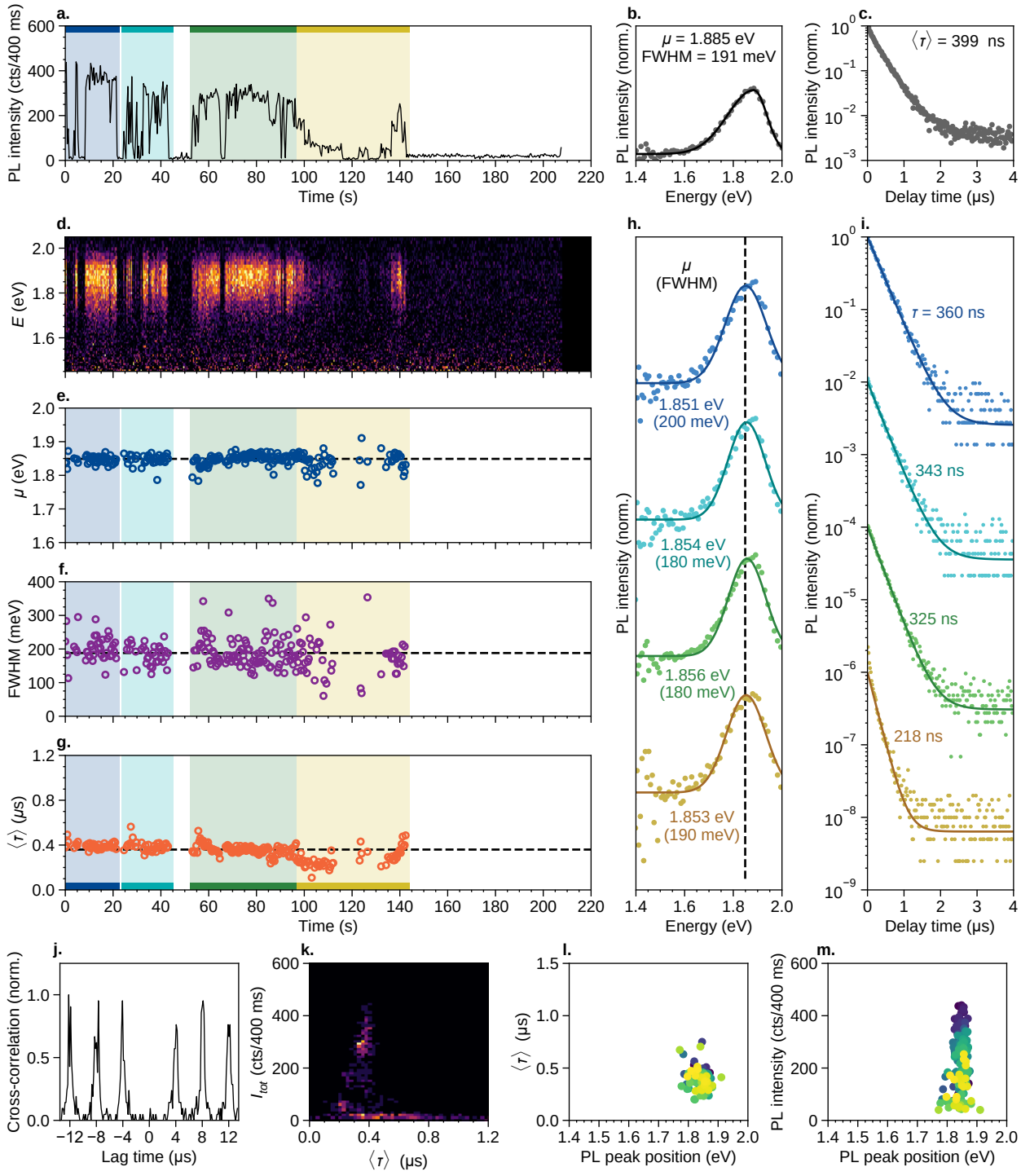

Figure E17 — Results of micro-spectroscopy experiment on core/shell $CuInS_2$/CdS quantum dot 1.

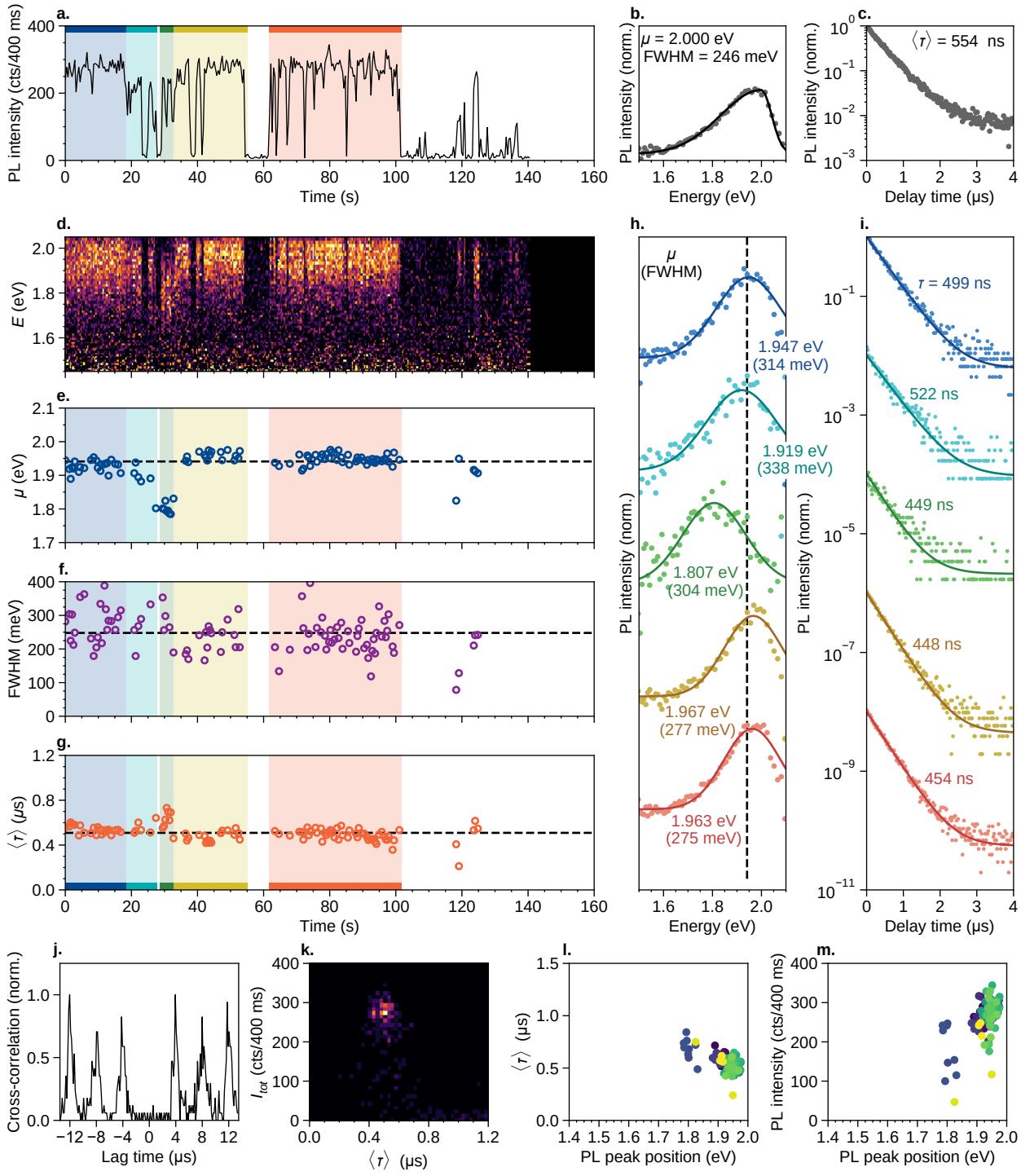

Figure E18 — Results of micro-spectroscopy experiment on core/shell $CuInS_2$/CdS quantum dot 2.

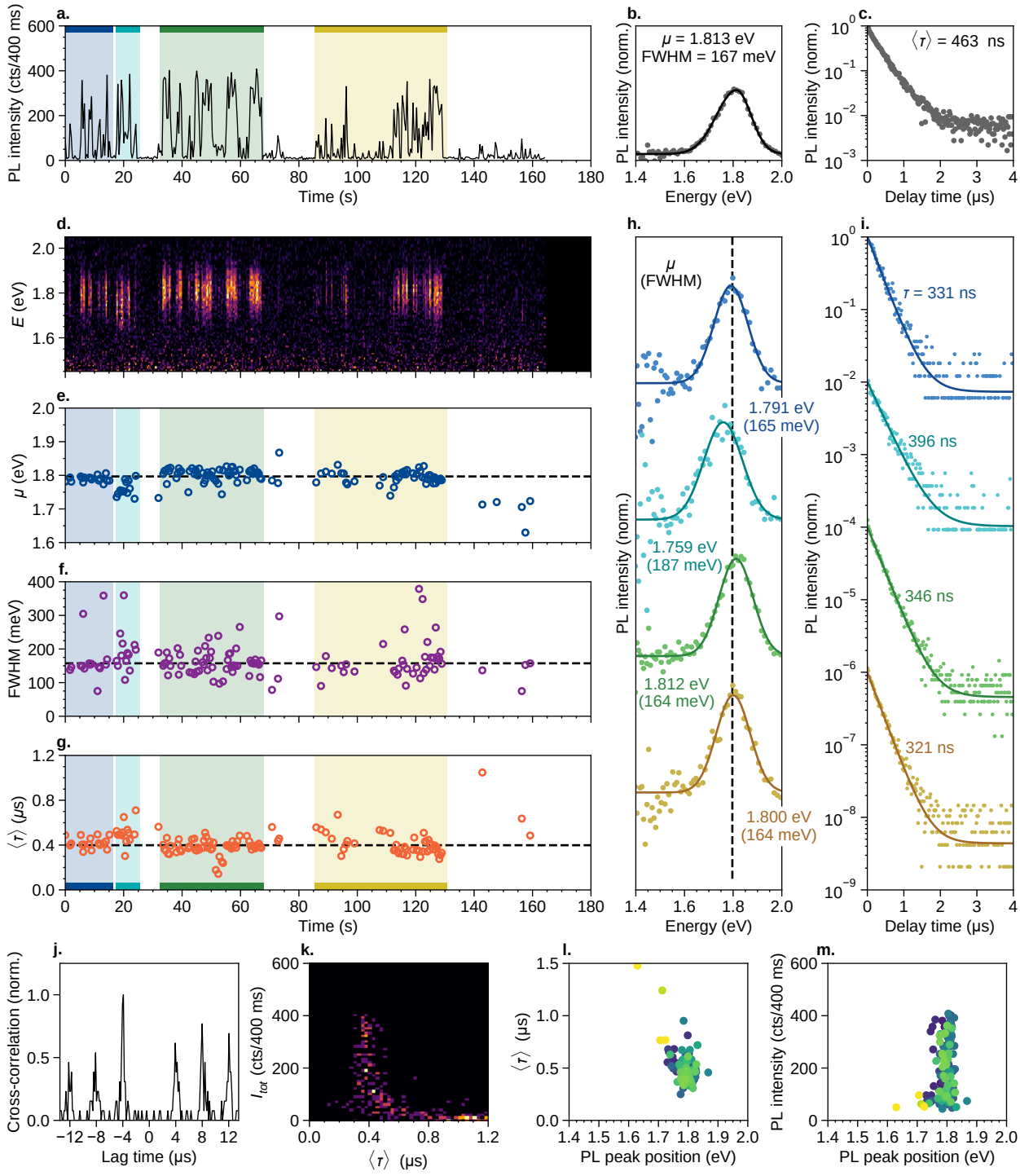

Figure E19 — Results of micro-spectroscopy experiment on core/shell $CuInS_2$/CdS quantum dot 3.

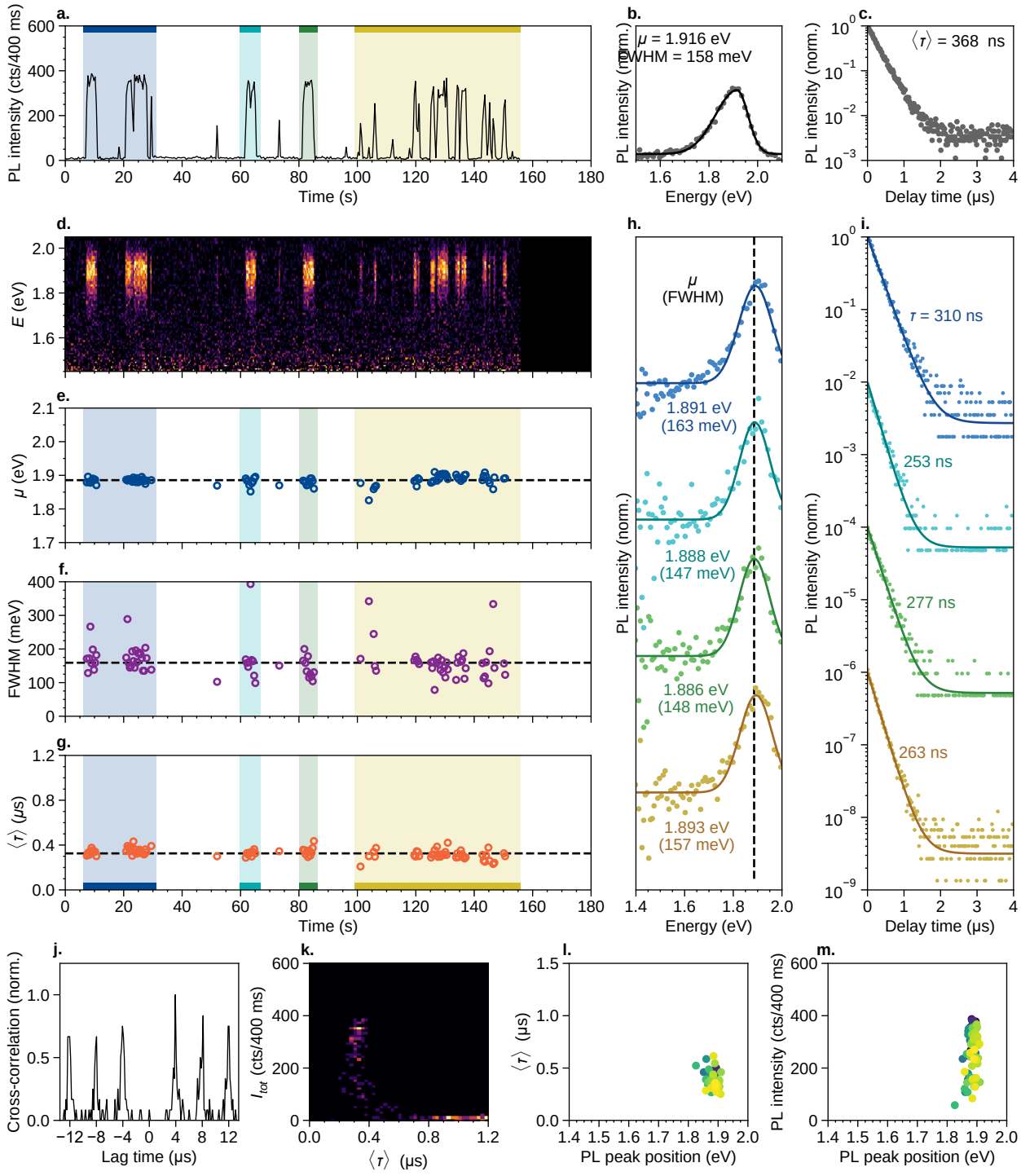

Figure E20 — Results of micro-spectroscopy experiment on core/shell $CuInS_2$/CdS quantum dot 4.

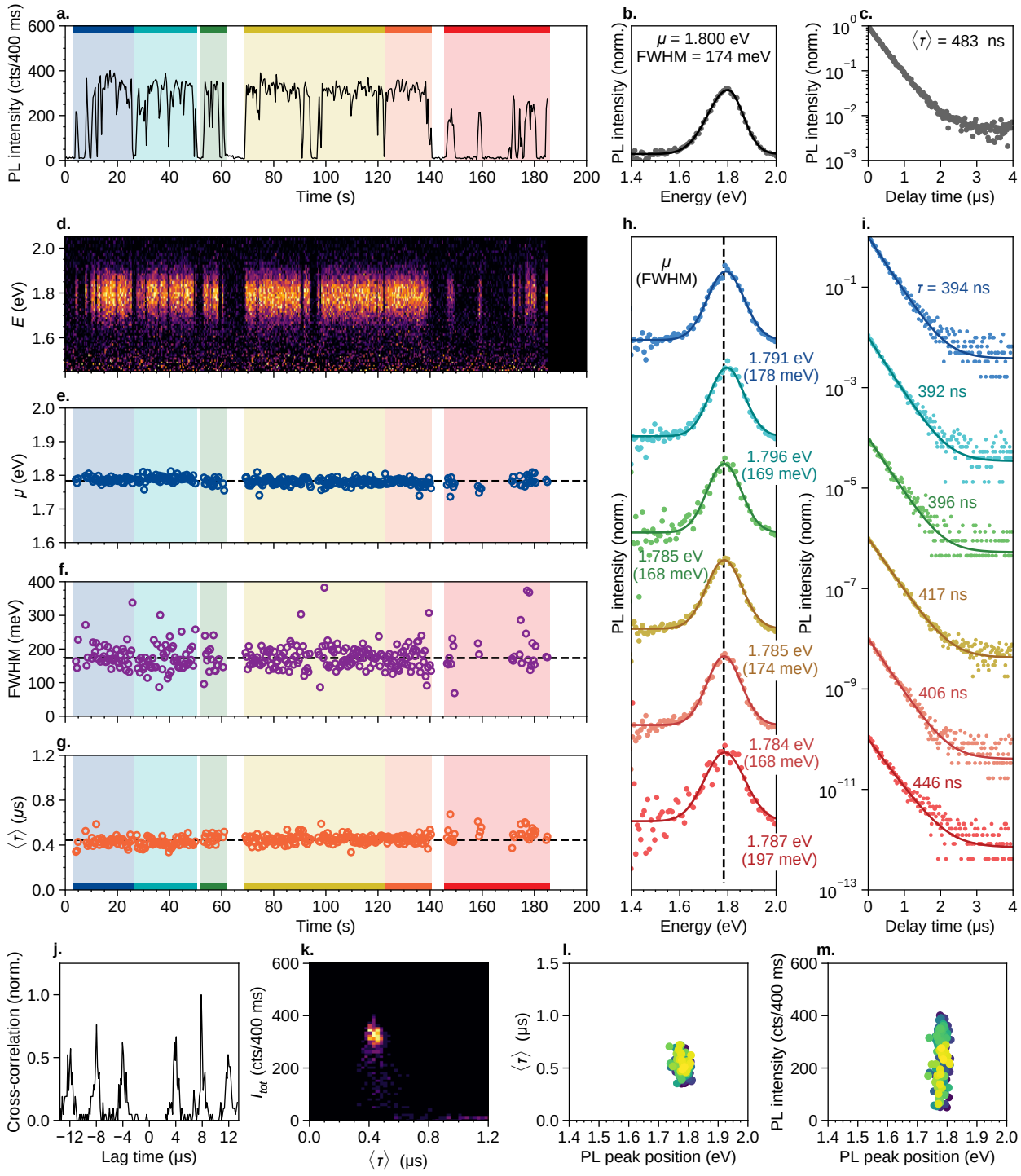

Figure E21 — Results of micro-spectroscopy experiment on core/shell $CuInS_2$/CdS quantum dot 5.

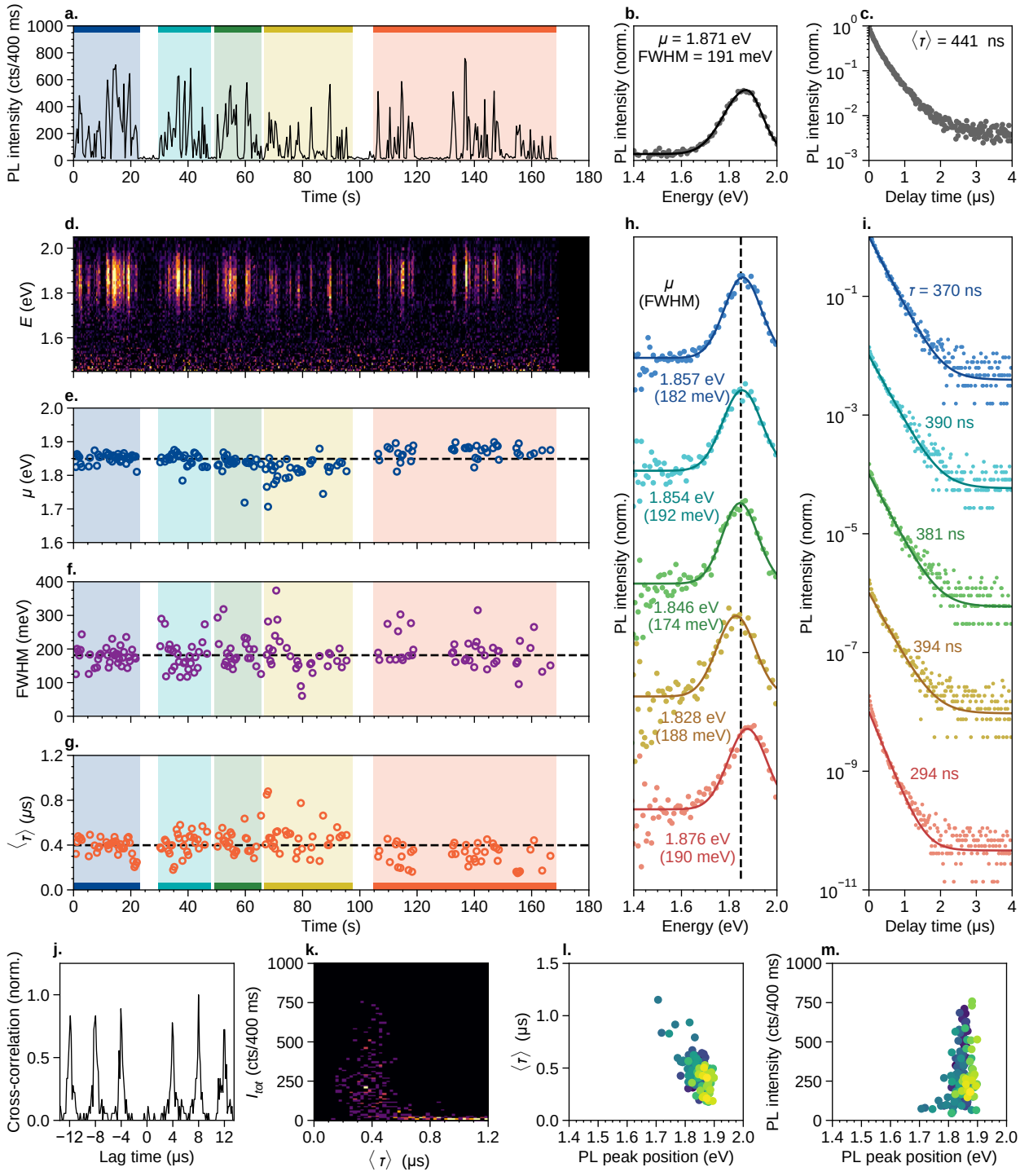

Figure E22 — Results of micro-spectroscopy experiment on core/shell $CuInS_2$/CdS quantum dot 6.

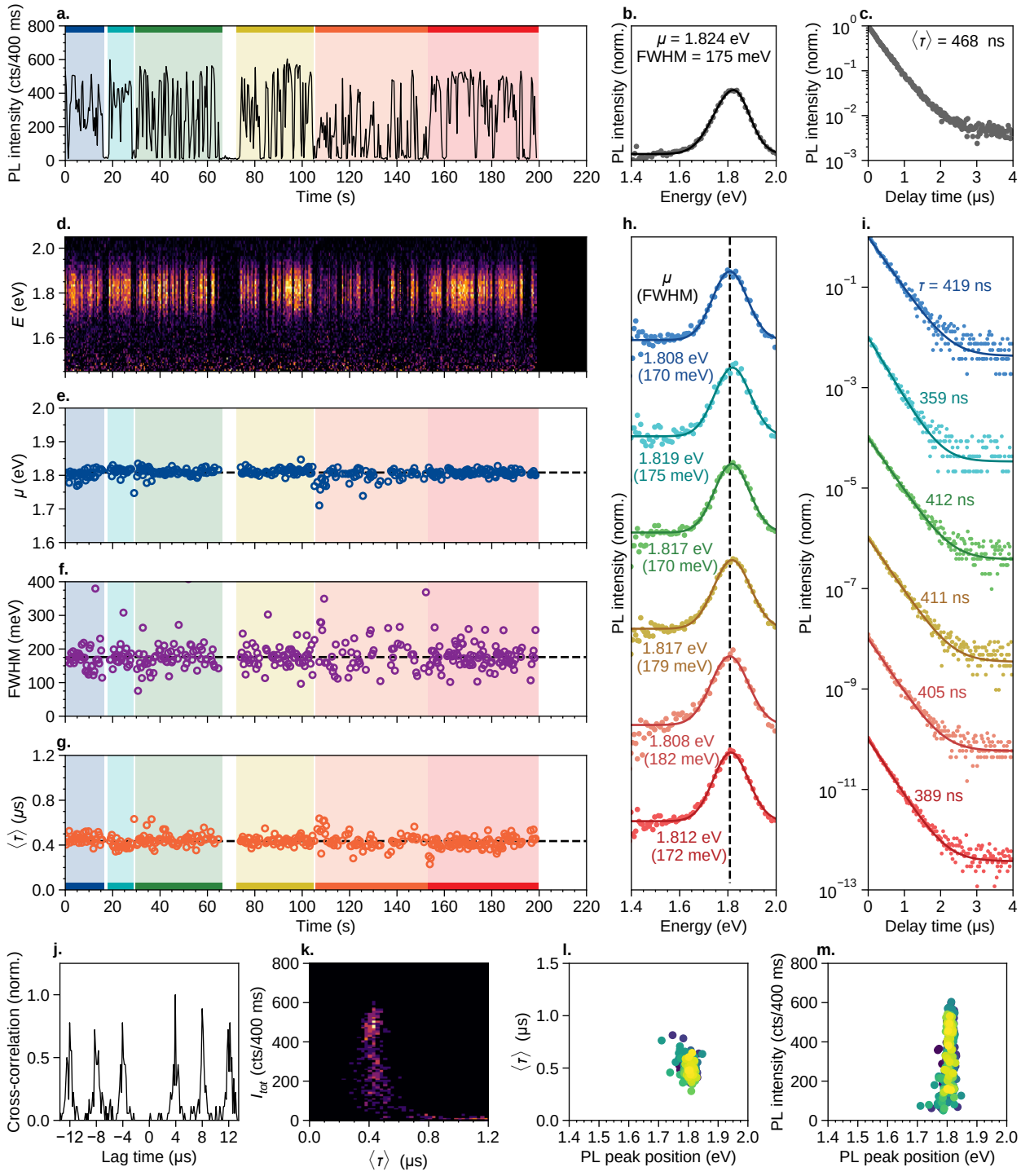

Figure E23 — Results of micro-spectroscopy experiment on core/shell $CuInS_2$/CdS quantum dot 7.

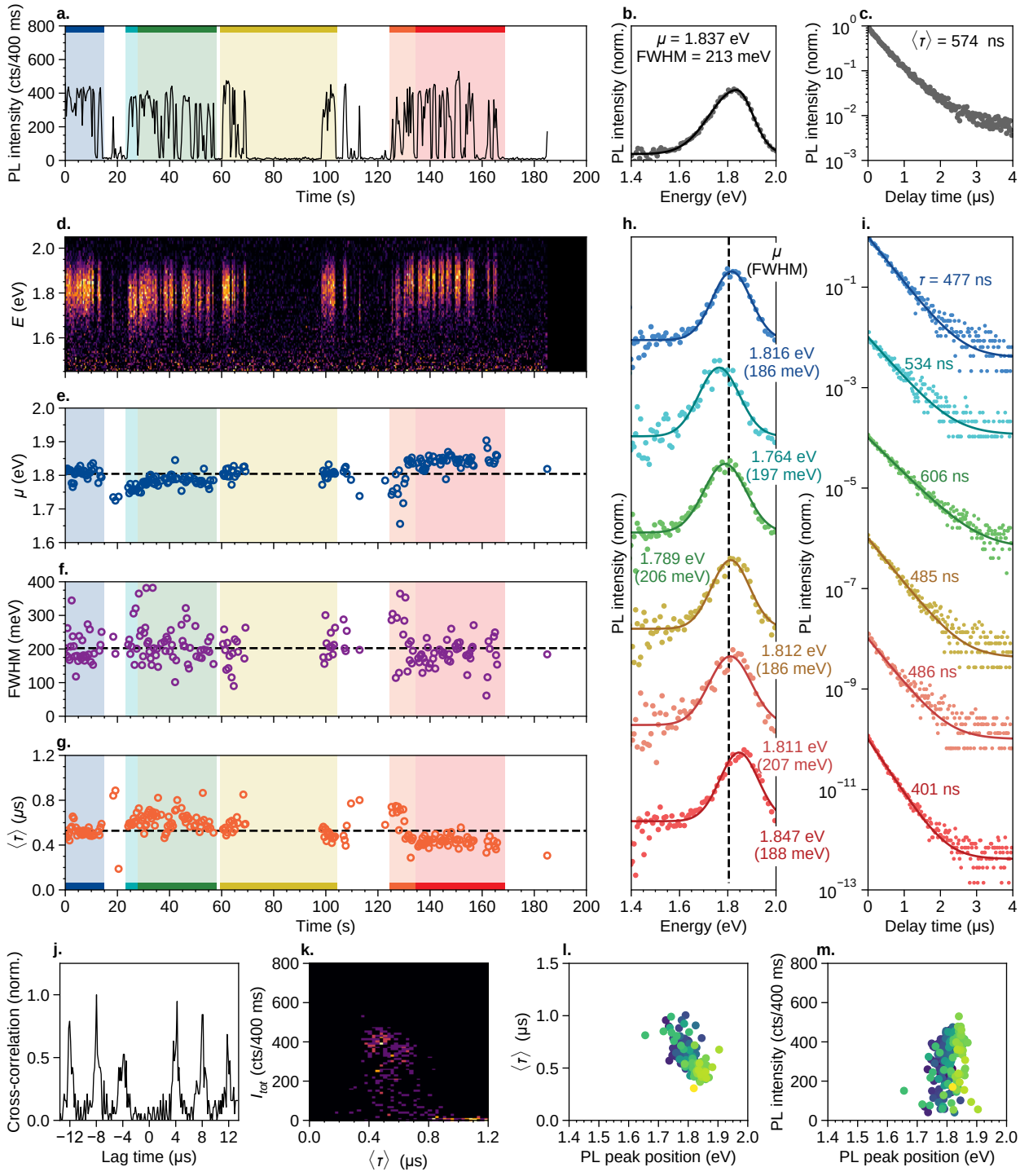

Figure E24 — Results of micro-spectroscopy experiment on core/shell $CuInS_2$/CdS quantum dot 8.

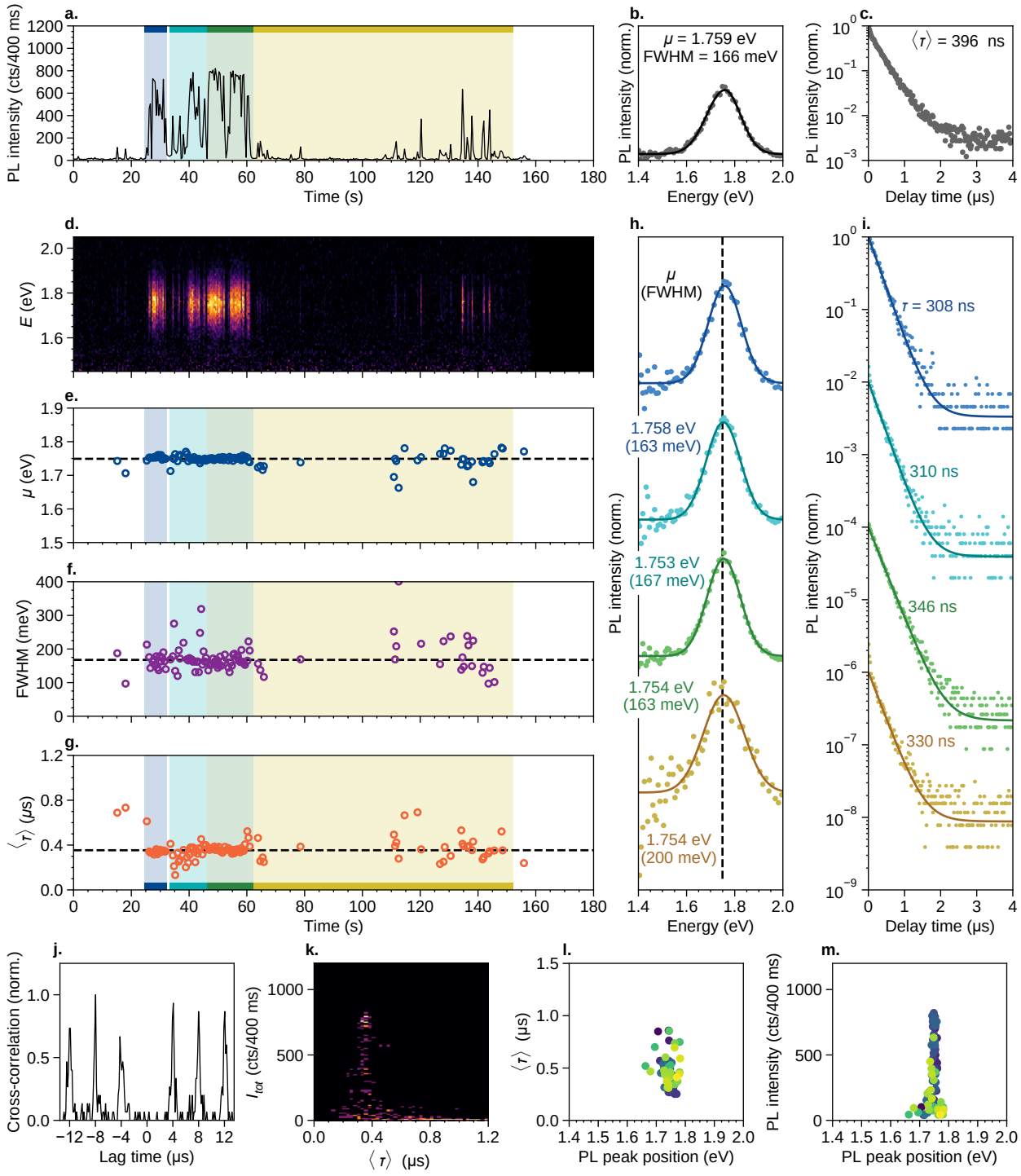

Figure E25 — Results of micro-spectroscopy experiment on core/shell $CuInS_2$/CdS quantum dot 9.

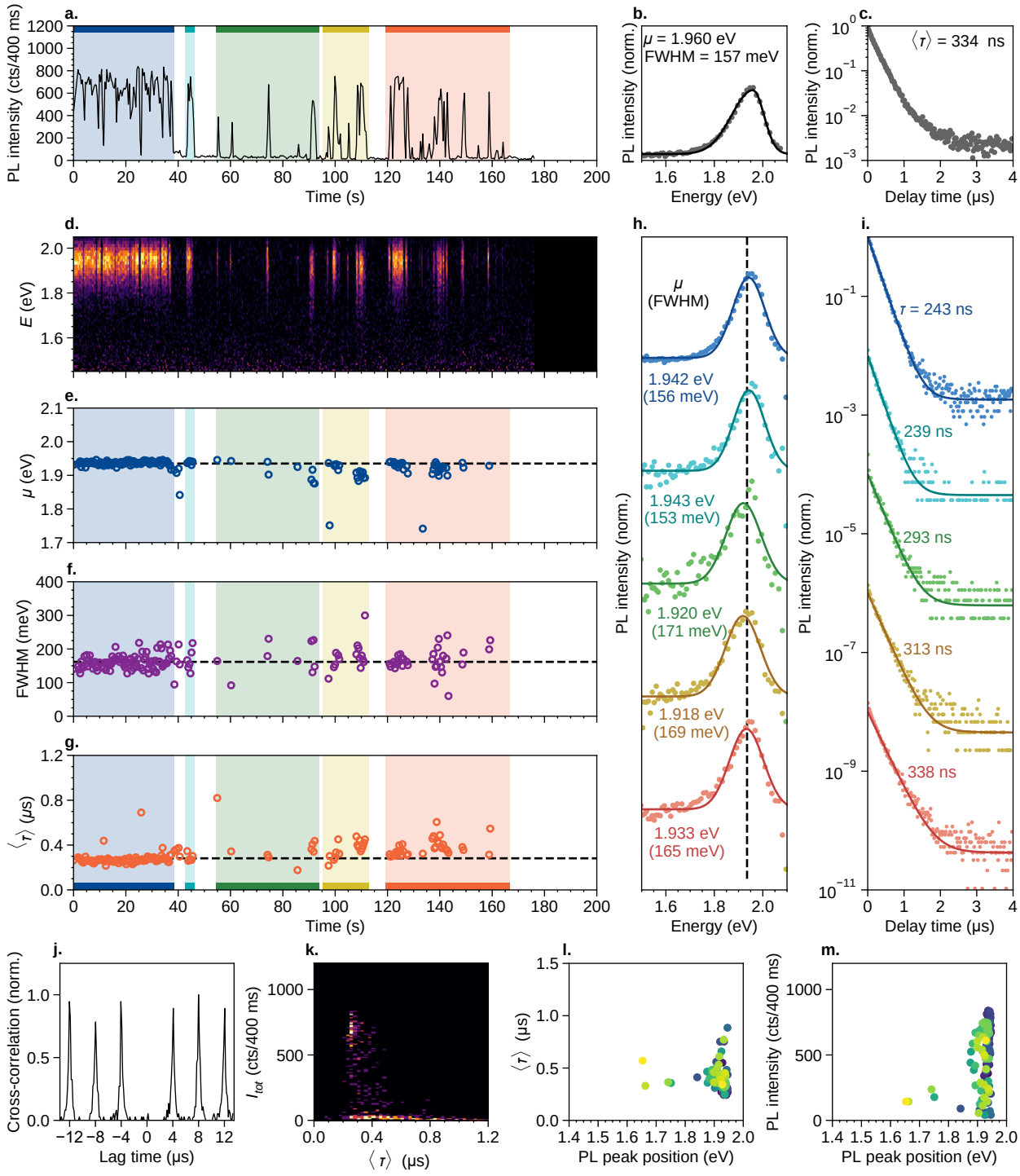

Figure E26 — Results of micro-spectroscopy experiment on core/shell $CuInS_2$/CdS quantum dot 10.

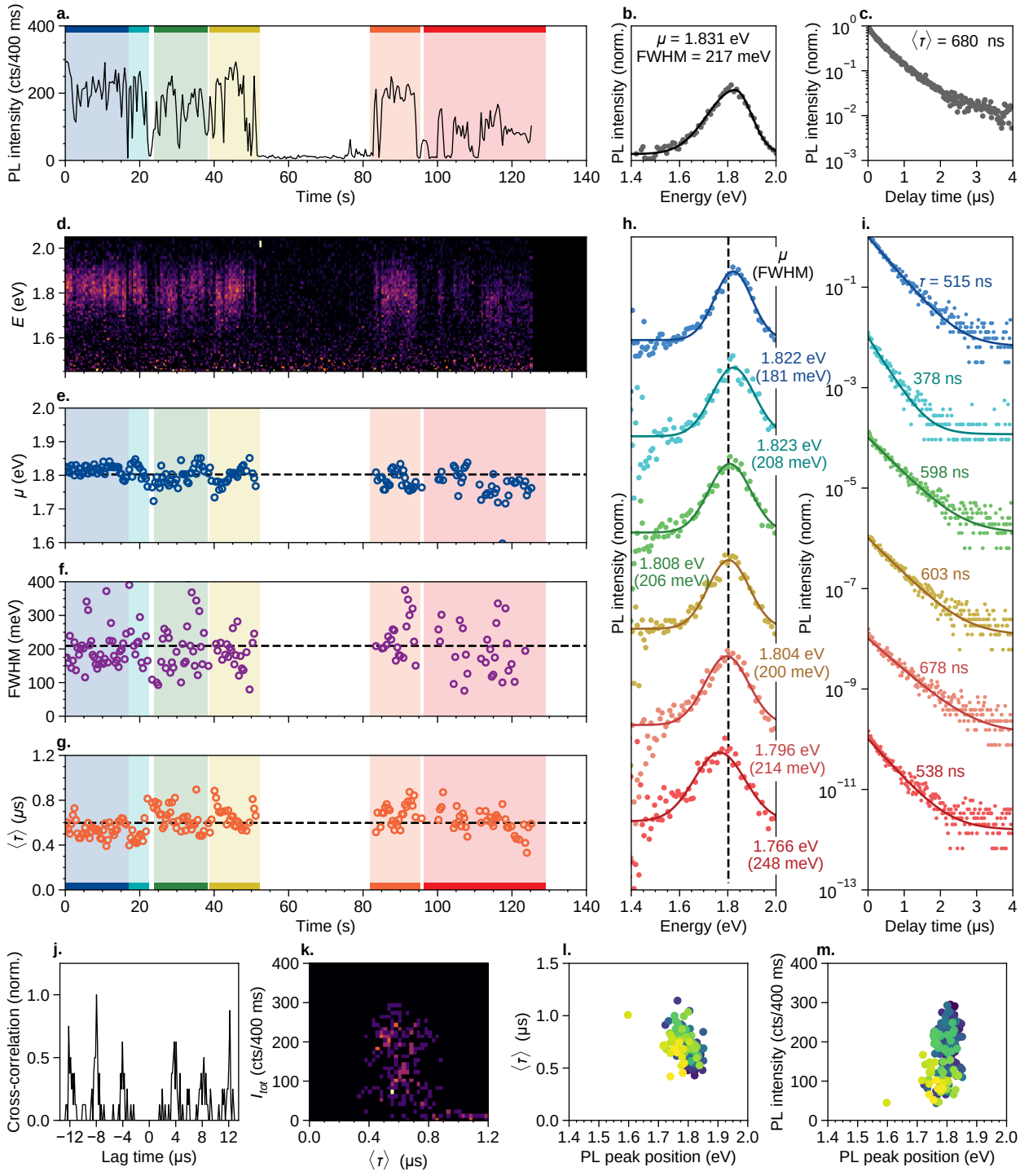

Figure E27 — Results of micro-spectroscopy experiment on core/shell $CuInS_2$/CdS quantum dot 11.

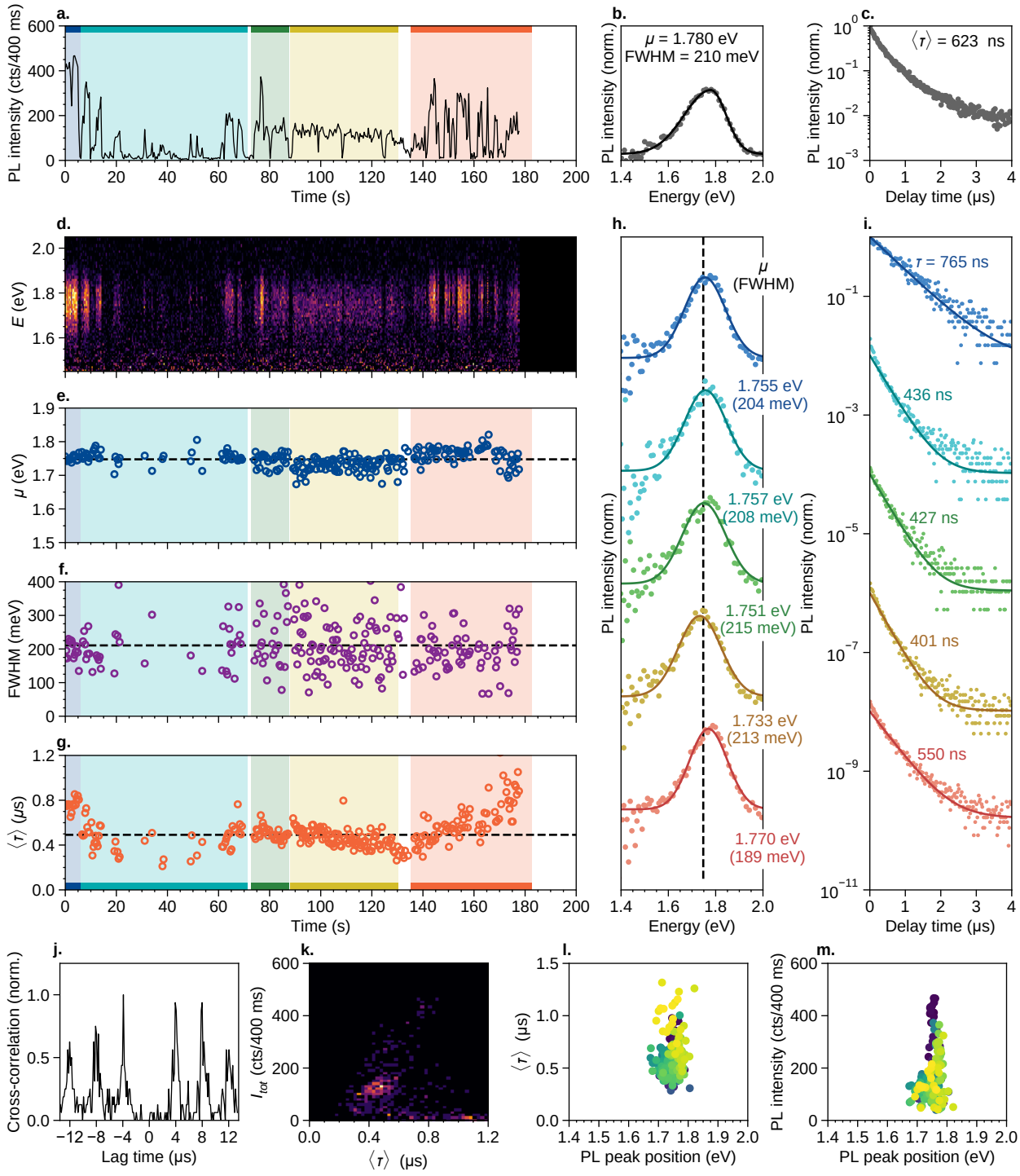

Figure E28 — Results of micro-spectroscopy experiment on core/shell $CuInS_2$/CdS quantum dot 12.

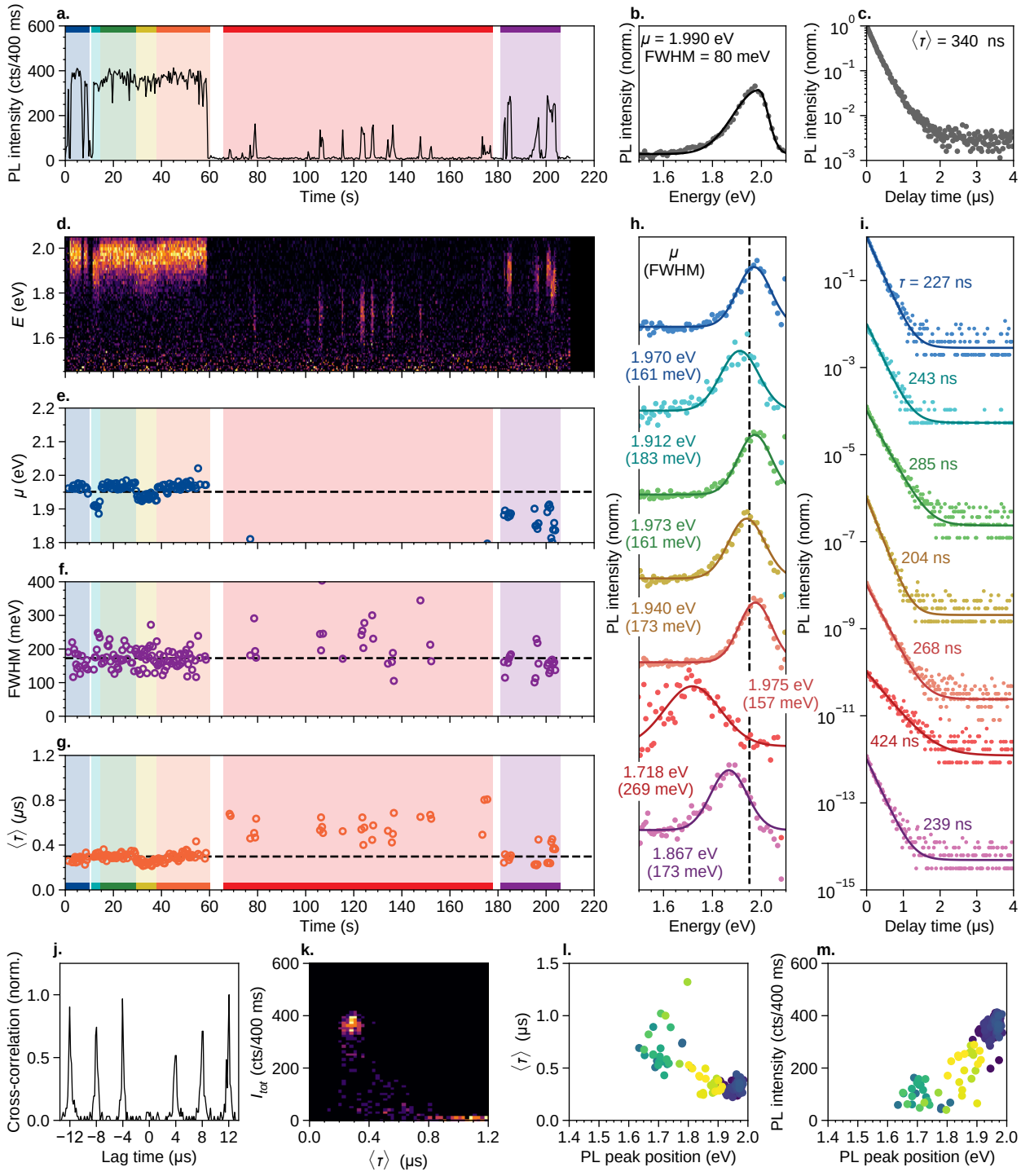

Figure E29 — Results of micro-spectroscopy experiment on core/shell $CuInS_2$/CdS quantum dot 13.

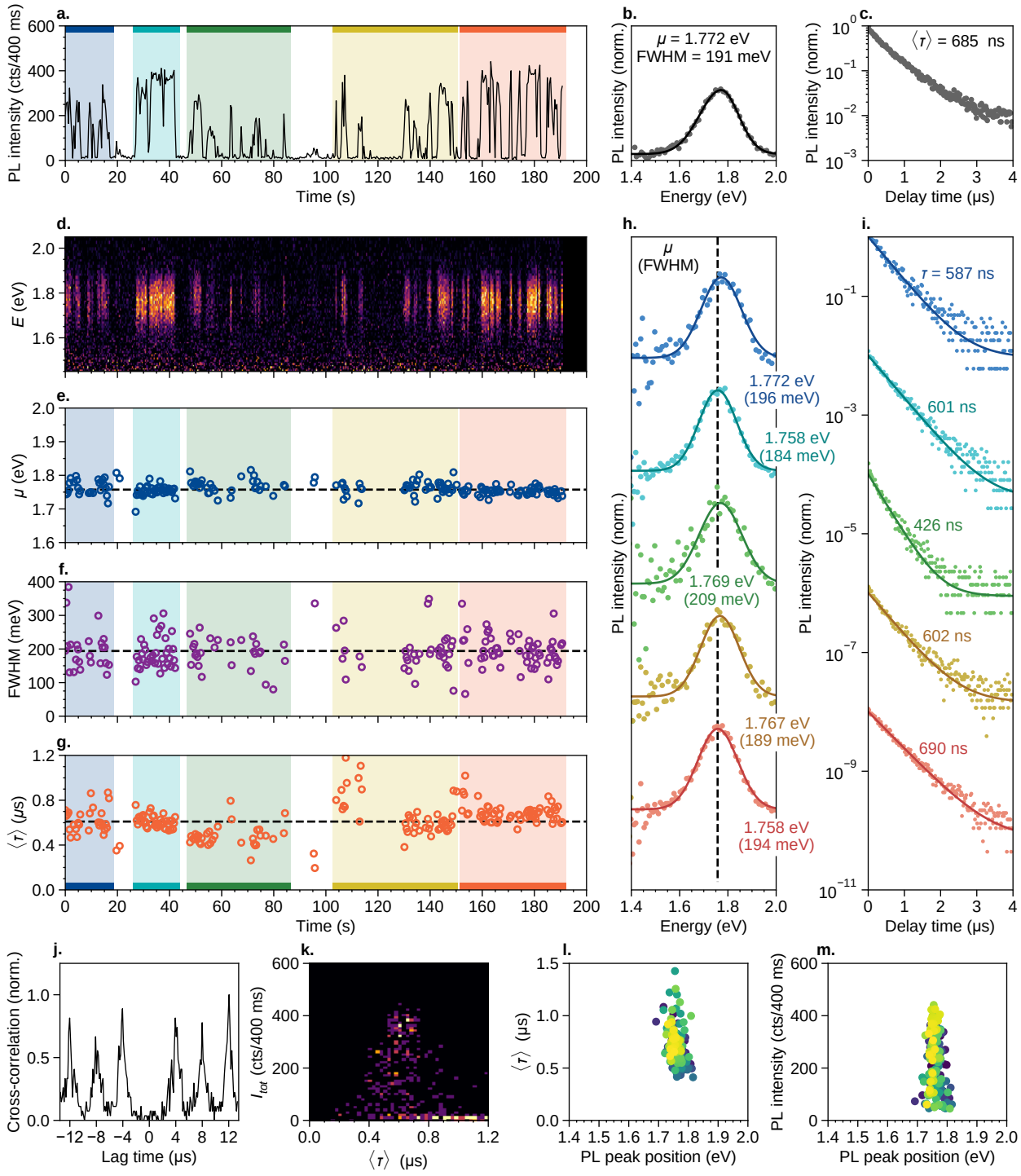

Figure E30 — Results of micro-spectroscopy experiment on core/shell $CuInS_2$/CdS quantum dot 14.

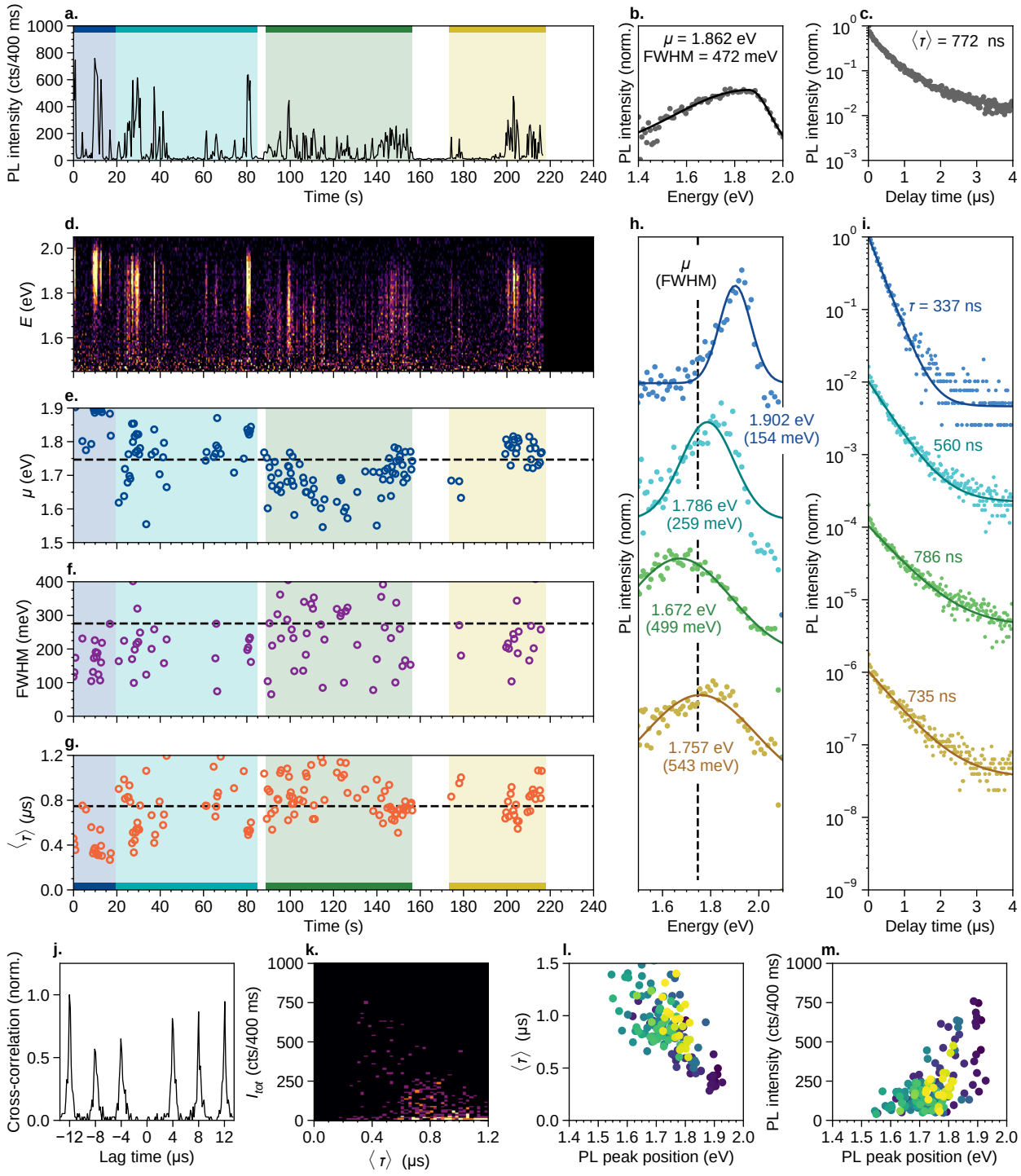

Figure E31 — Results of micro-spectroscopy experiment on core/shell $CuInS_2$/CdS quantum dot 15.

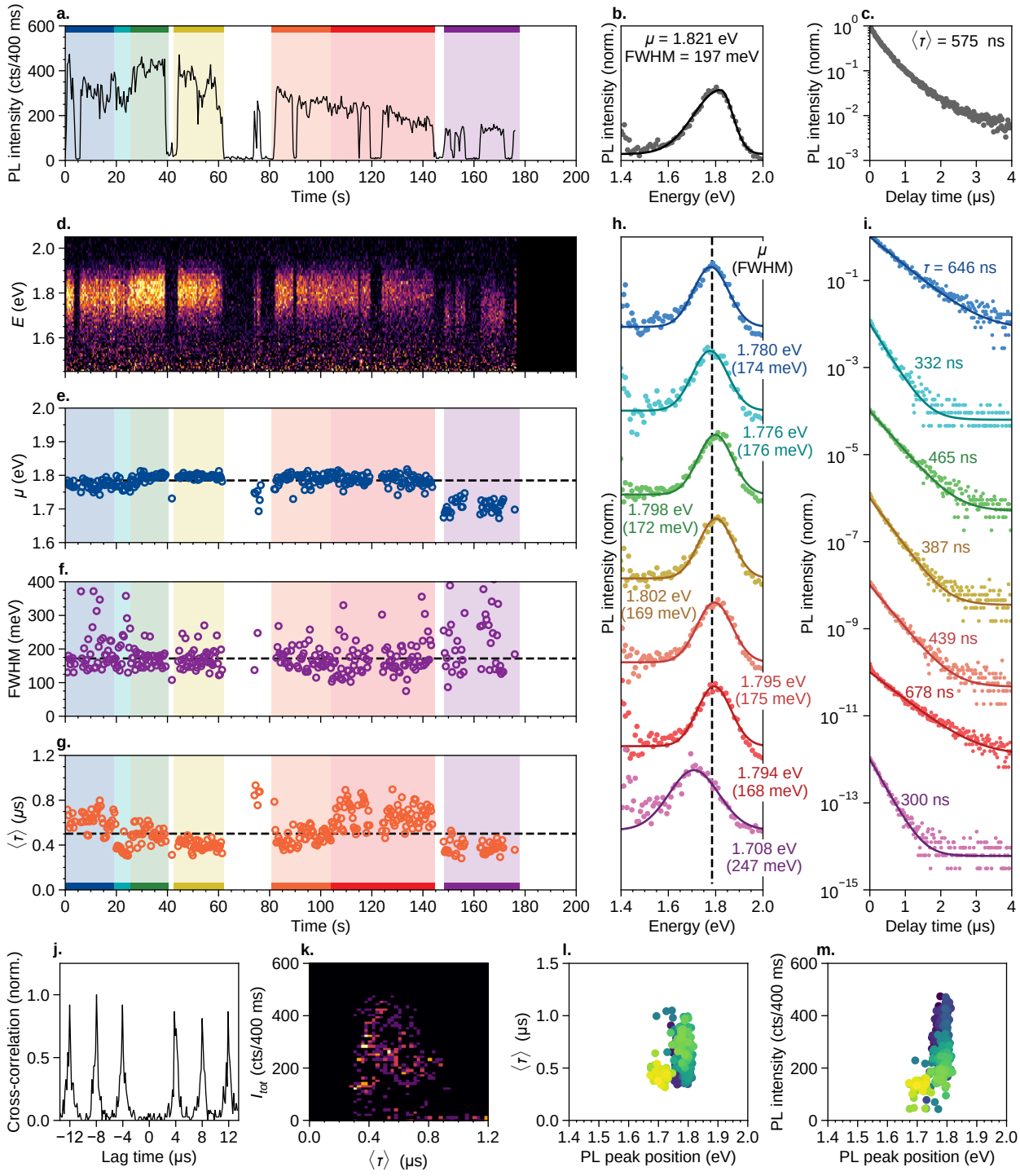

Figure E32 — Results of micro-spectroscopy experiment on core/shell $CuInS_2$/CdS quantum dot 16.

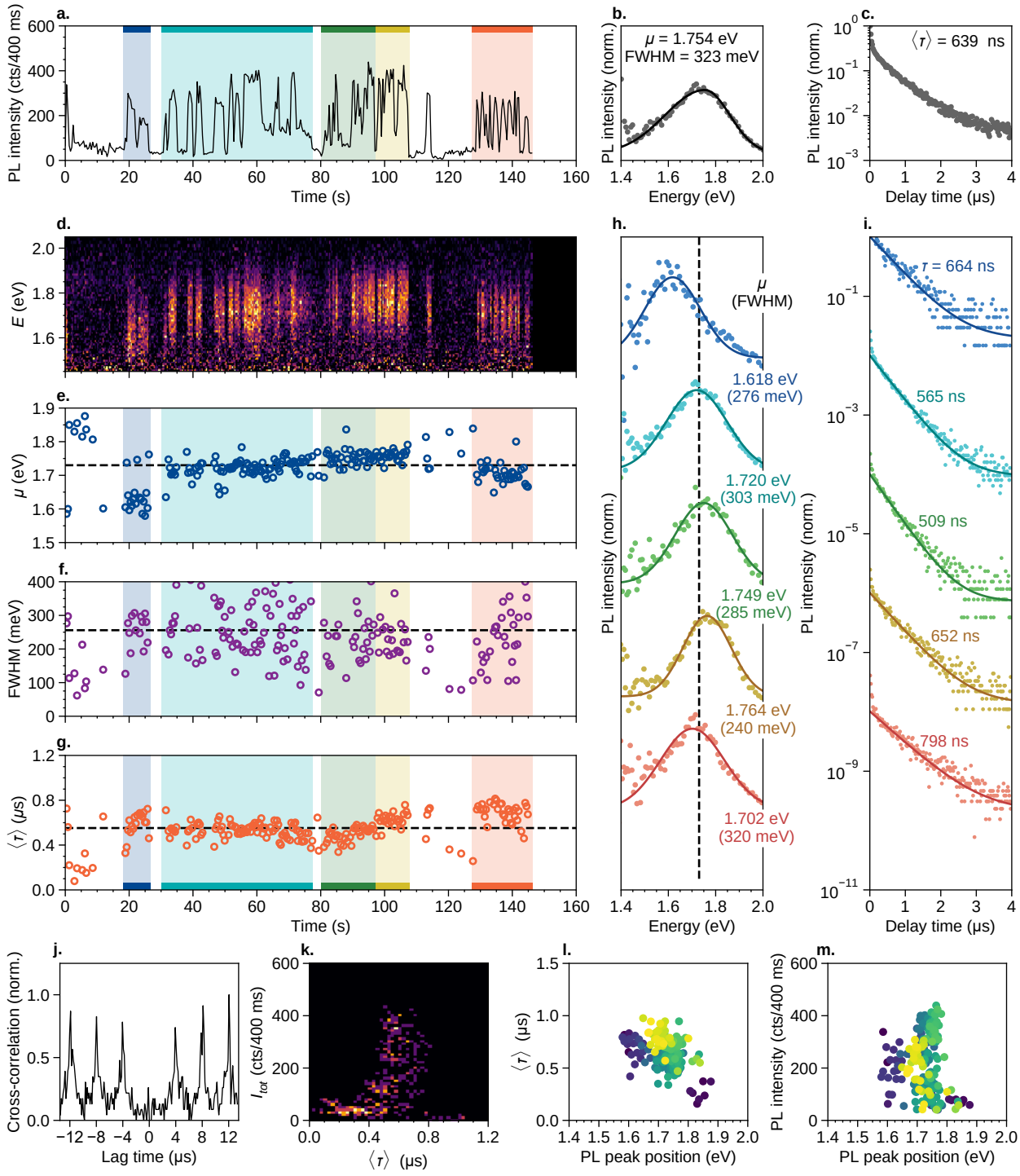

Figure E33 — Results of micro-spectroscopy experiment on core/shell $CuInS_2$/CdS quantum dot 17.

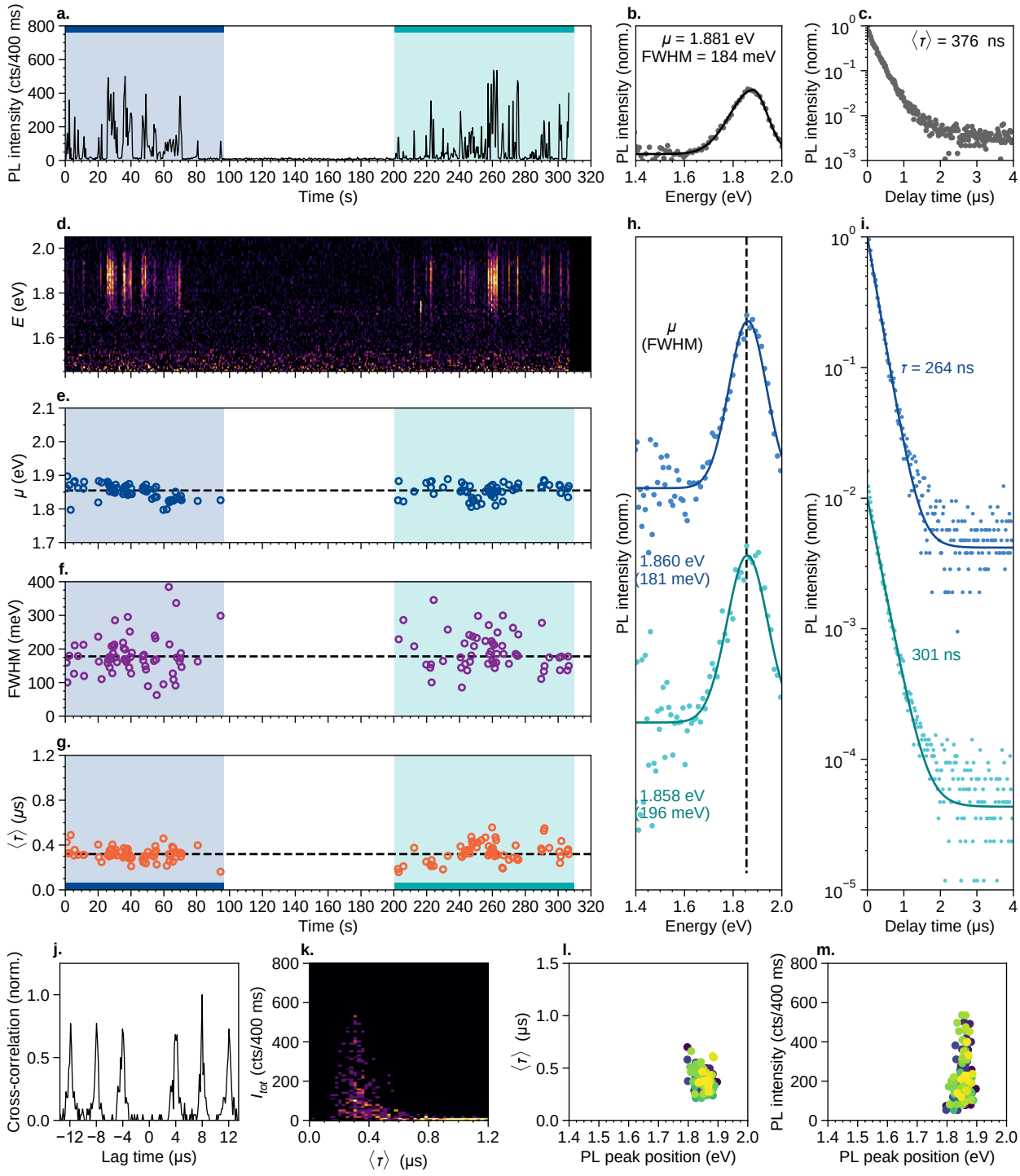

Figure E34 — Results of micro-spectroscopy experiment on core/shell $CuInS_2$/CdS quantum dot 18.

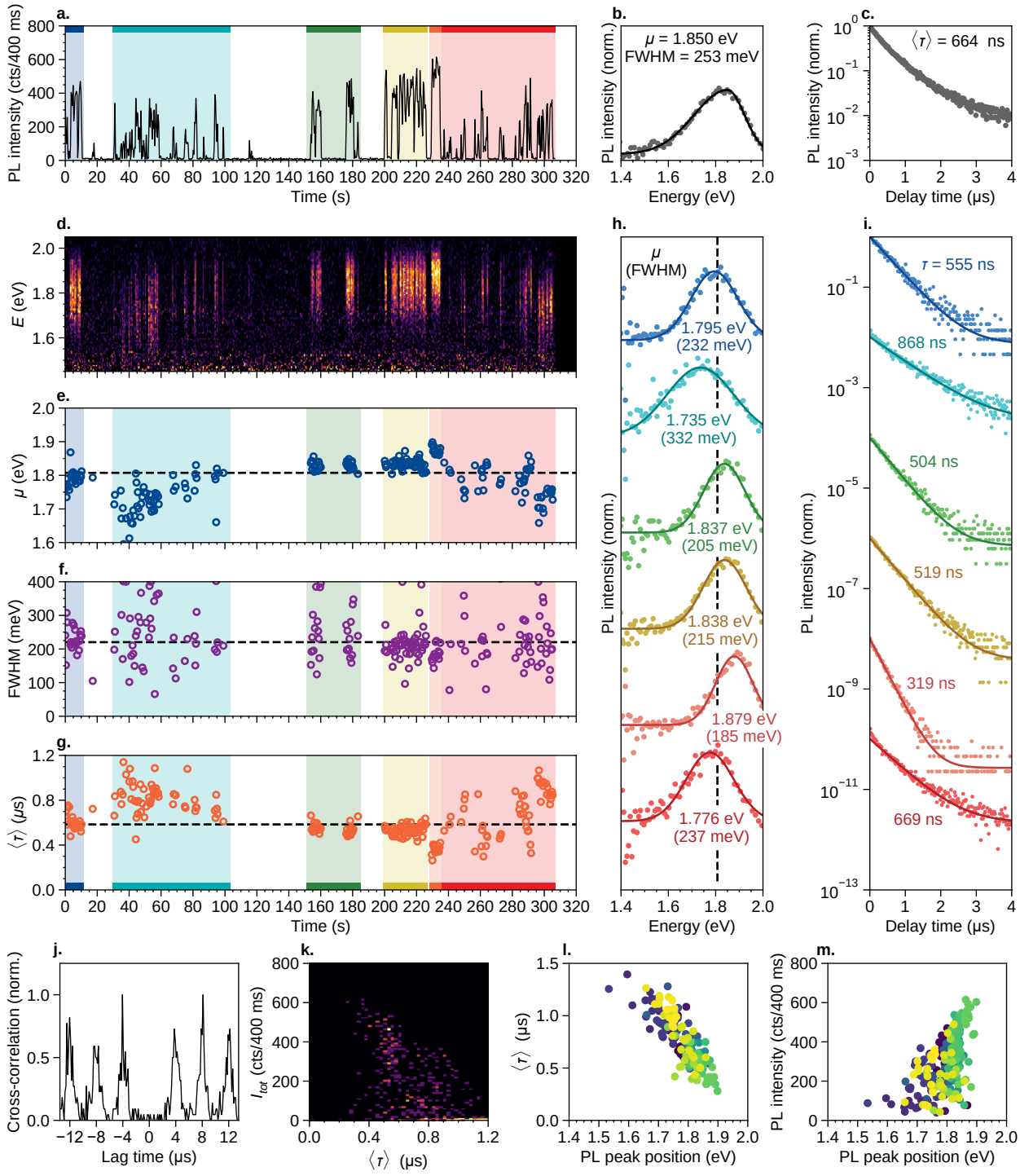

Figure E35 — Results of micro-spectroscopy experiment on core/shell $CuInS_2$/CdS quantum dot 19.

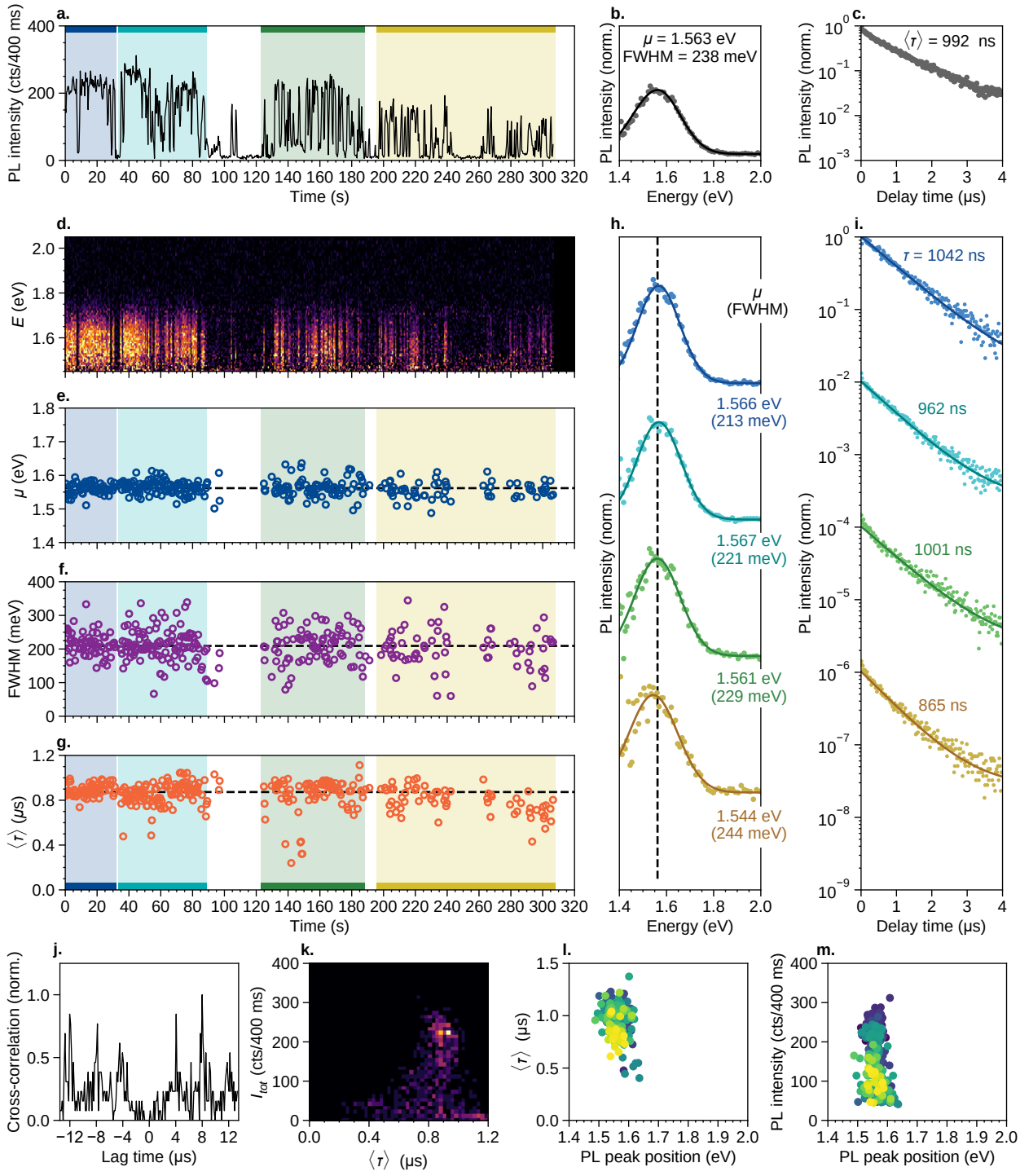

Figure E36 — Results of micro-spectroscopy experiment on core/shell $CuInS_2$/CdS quantum dot 20.

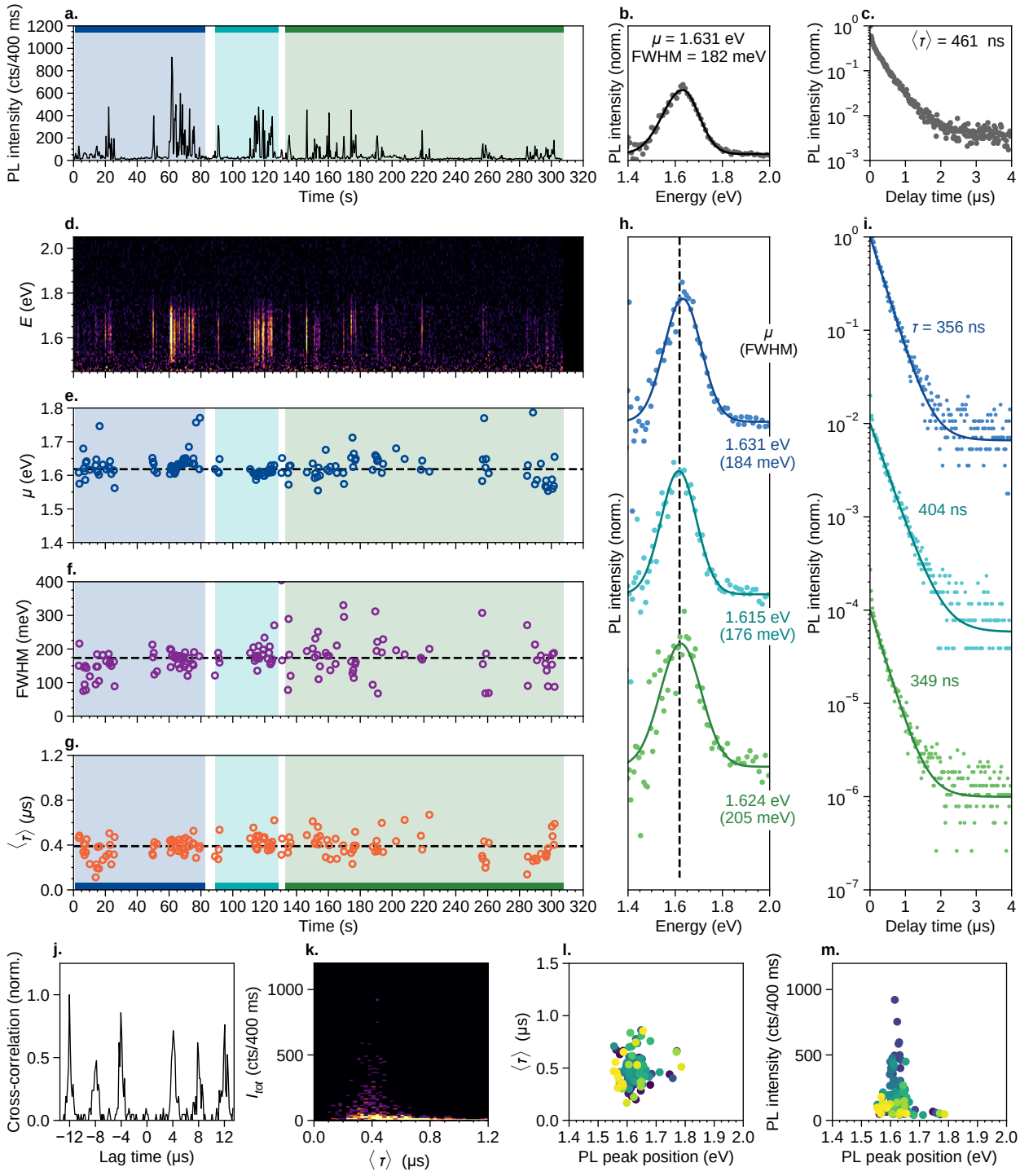

Figure E37 — Results of micro-spectroscopy experiment on core/shell $CuInS_2$/CdS quantum dot 21.

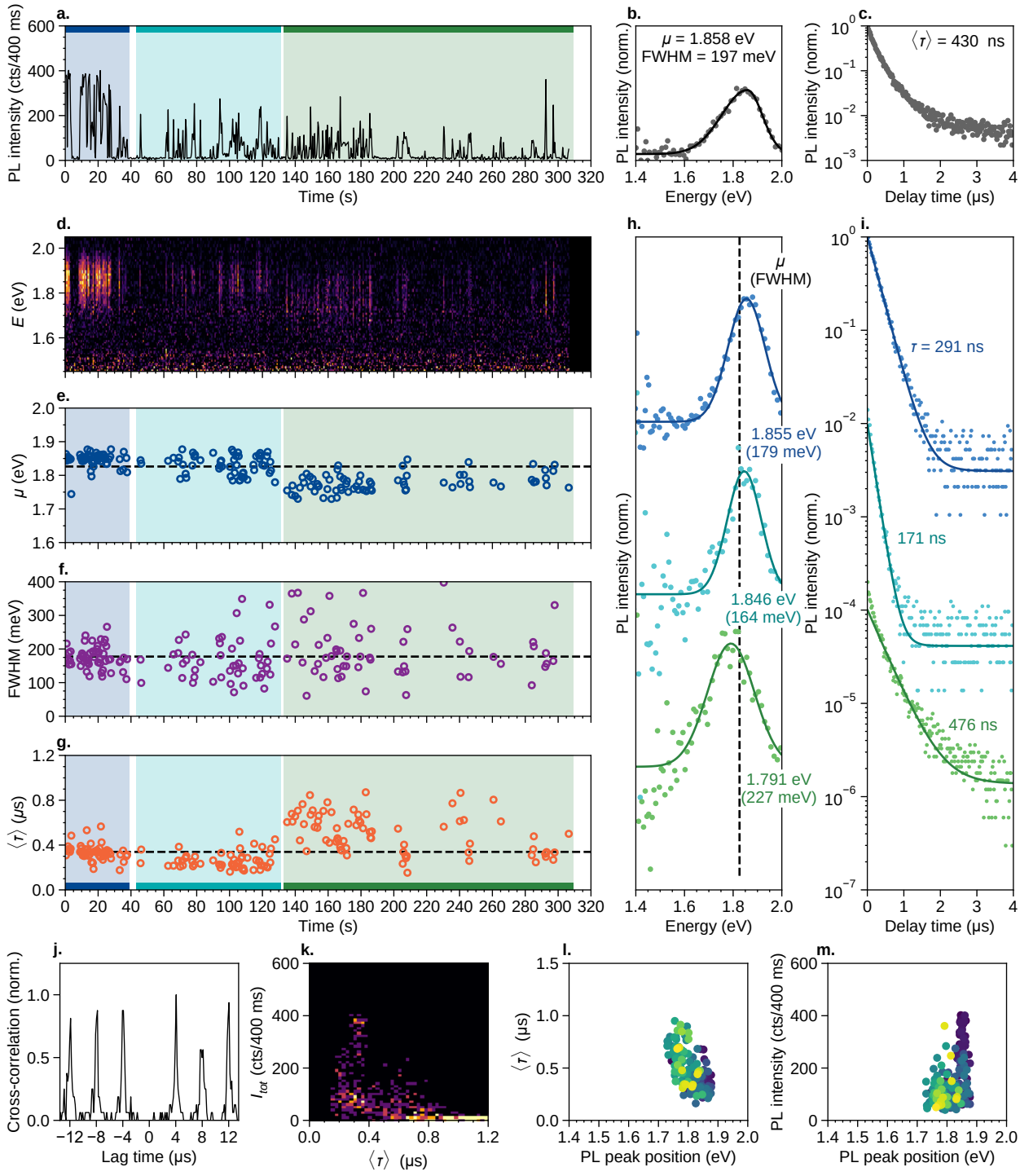

Figure E38 — Results of micro-spectroscopy experiment on core/shell $CuInS_2$/CdS quantum dot 22.

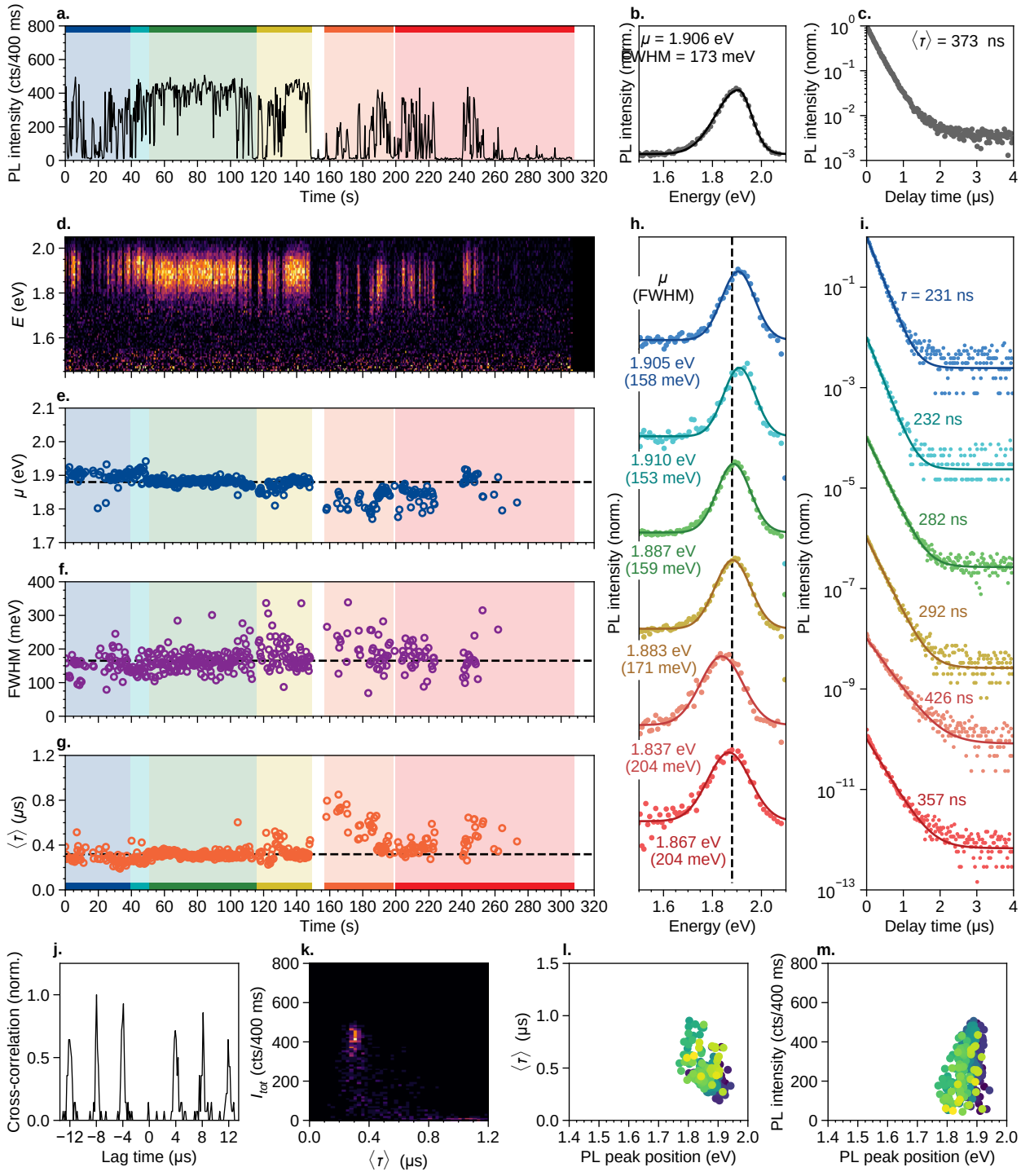

Figure E39 — Results of micro-spectroscopy experiment on core/shell $CuInS_2$/CdS quantum dot 23.

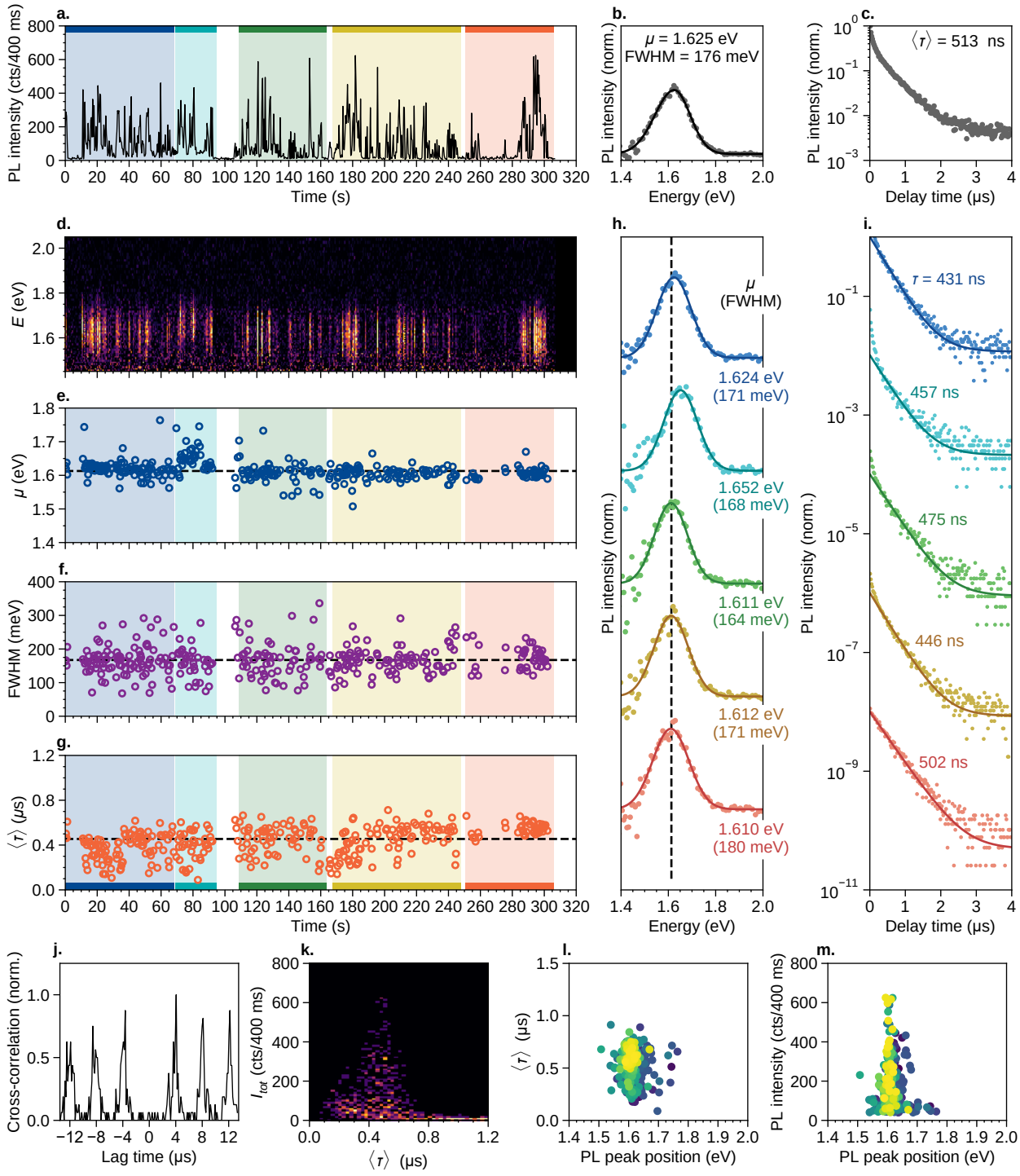

Figure E40 — Results of micro-spectroscopy experiment on core/shell $CuInS_2$/CdS quantum dot 24.

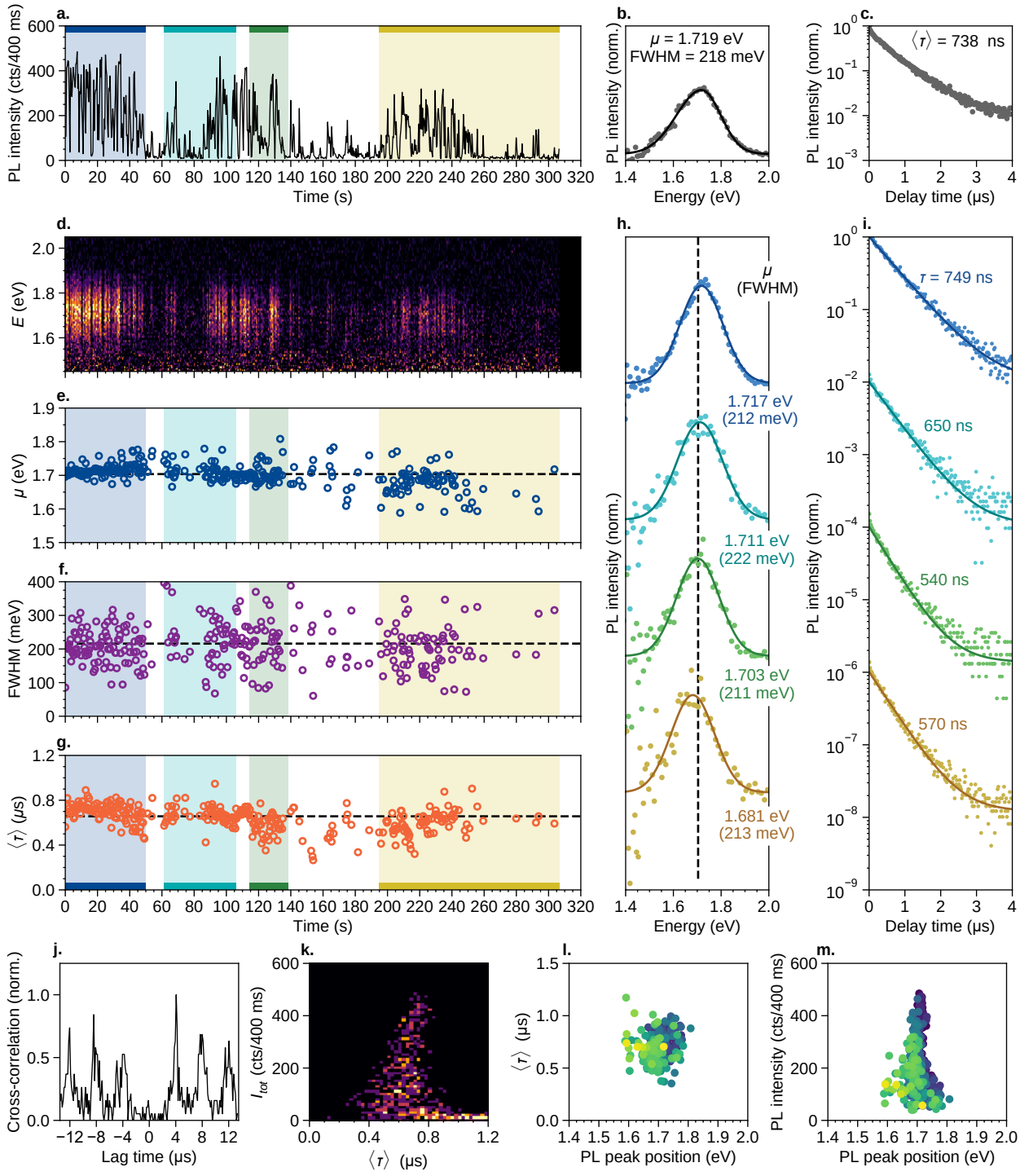

Figure E41 — Results of micro-spectroscopy experiment on core/shell $CuInS_2$/CdS quantum dot 25.

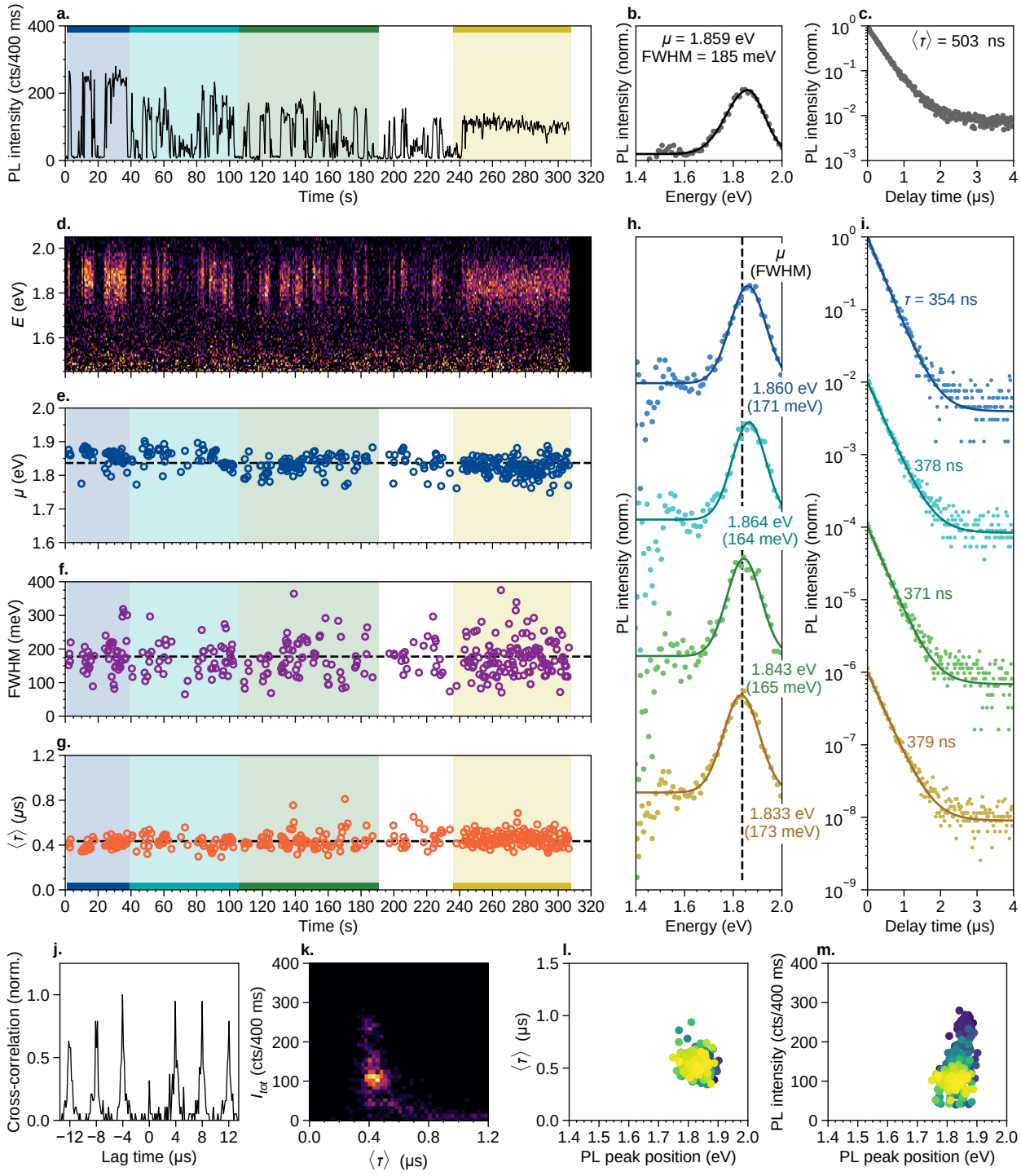

Figure E42 — Results of micro-spectroscopy experiment on core/shell $CuInS_2$/CdS quantum dot 26.

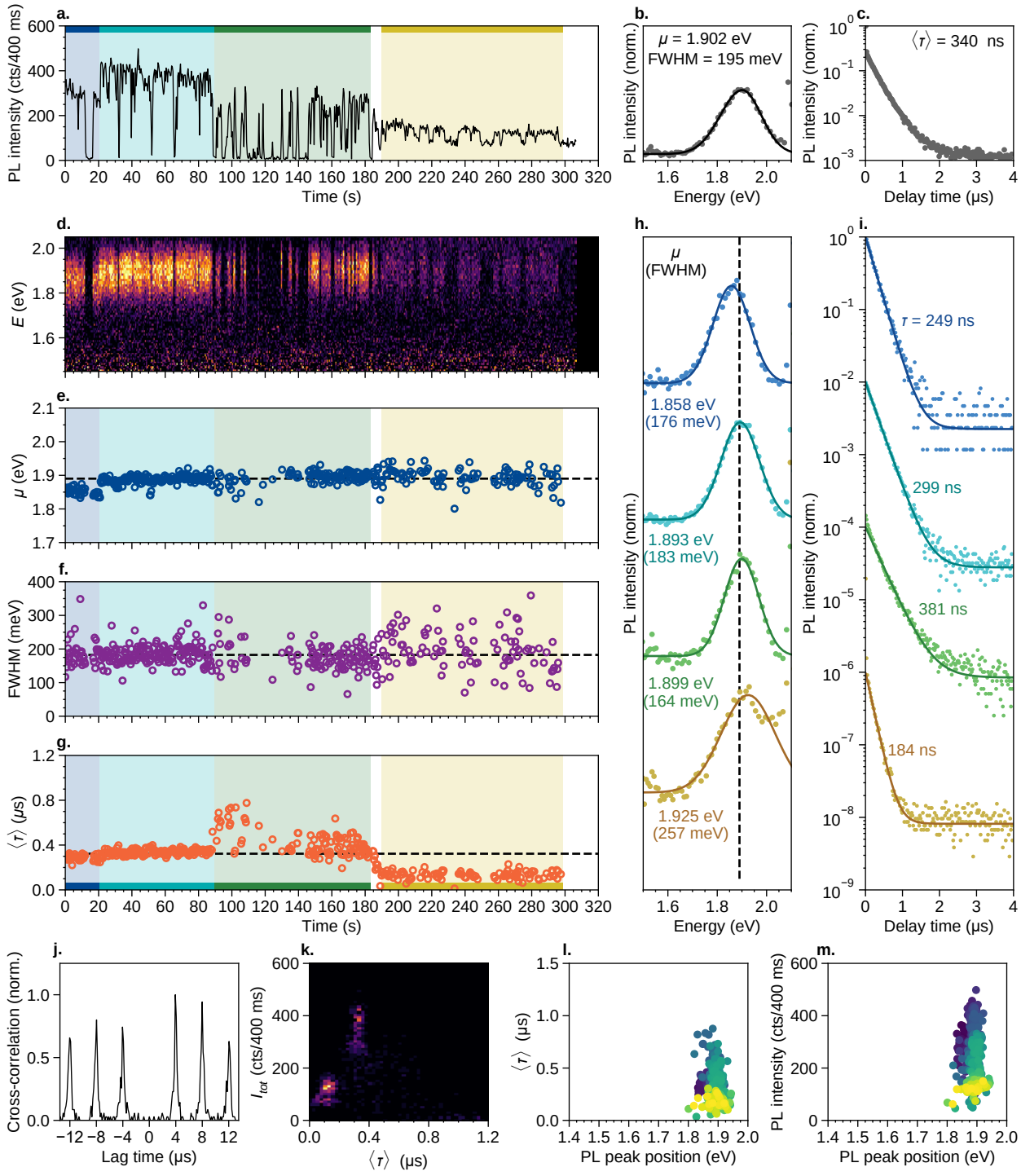

Figure E43 — Results of micro-spectroscopy experiment on core/shell $CuInS_2$/CdS quantum dot 27.

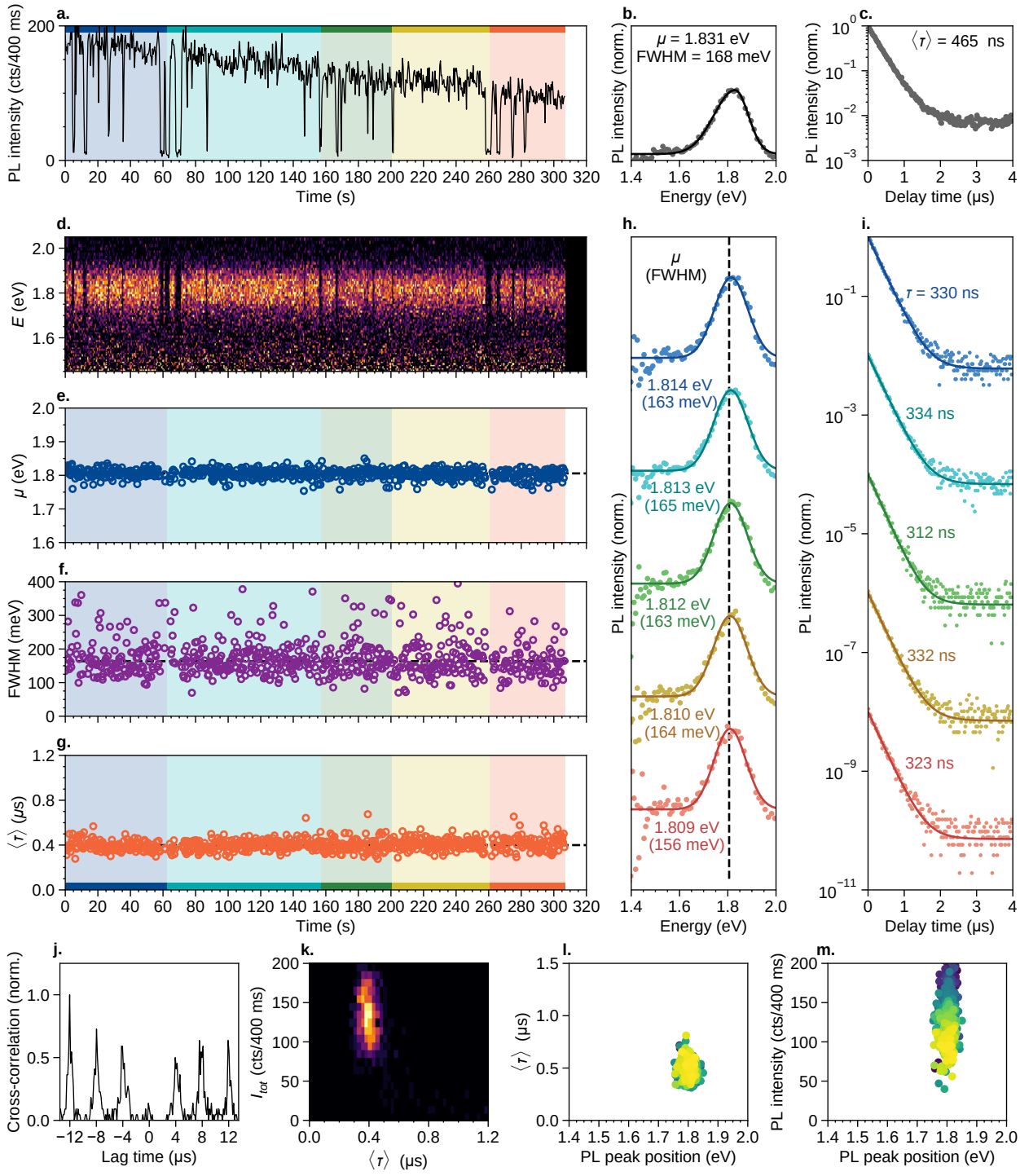

Figure E44 — Results of micro-spectroscopy experiment on core/shell $CuInS_2$/CdS quantum dot 28.

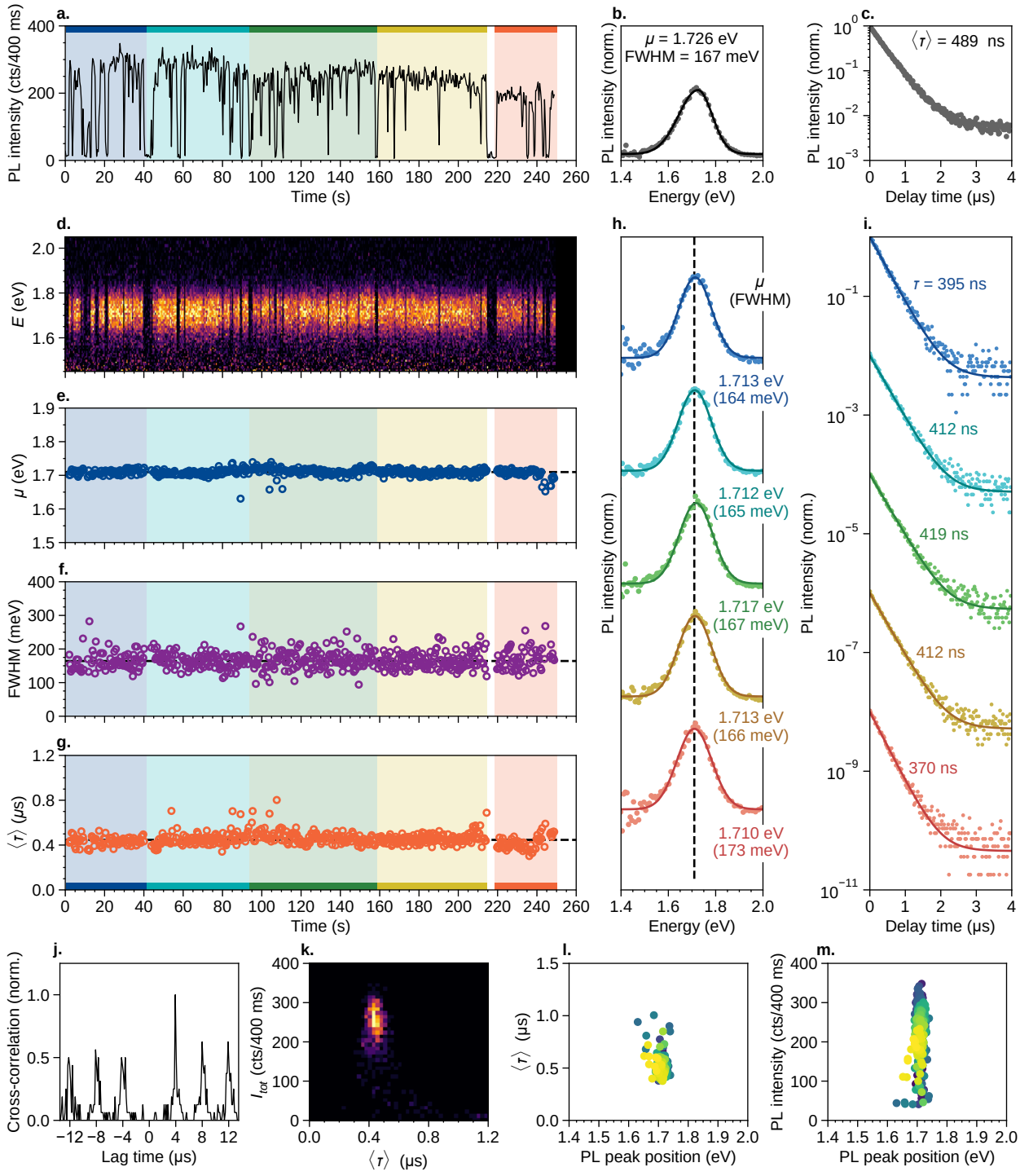

Figure E45 — Results of micro-spectroscopy experiment on core/shell $CuInS_2$/CdS quantum dot 29.

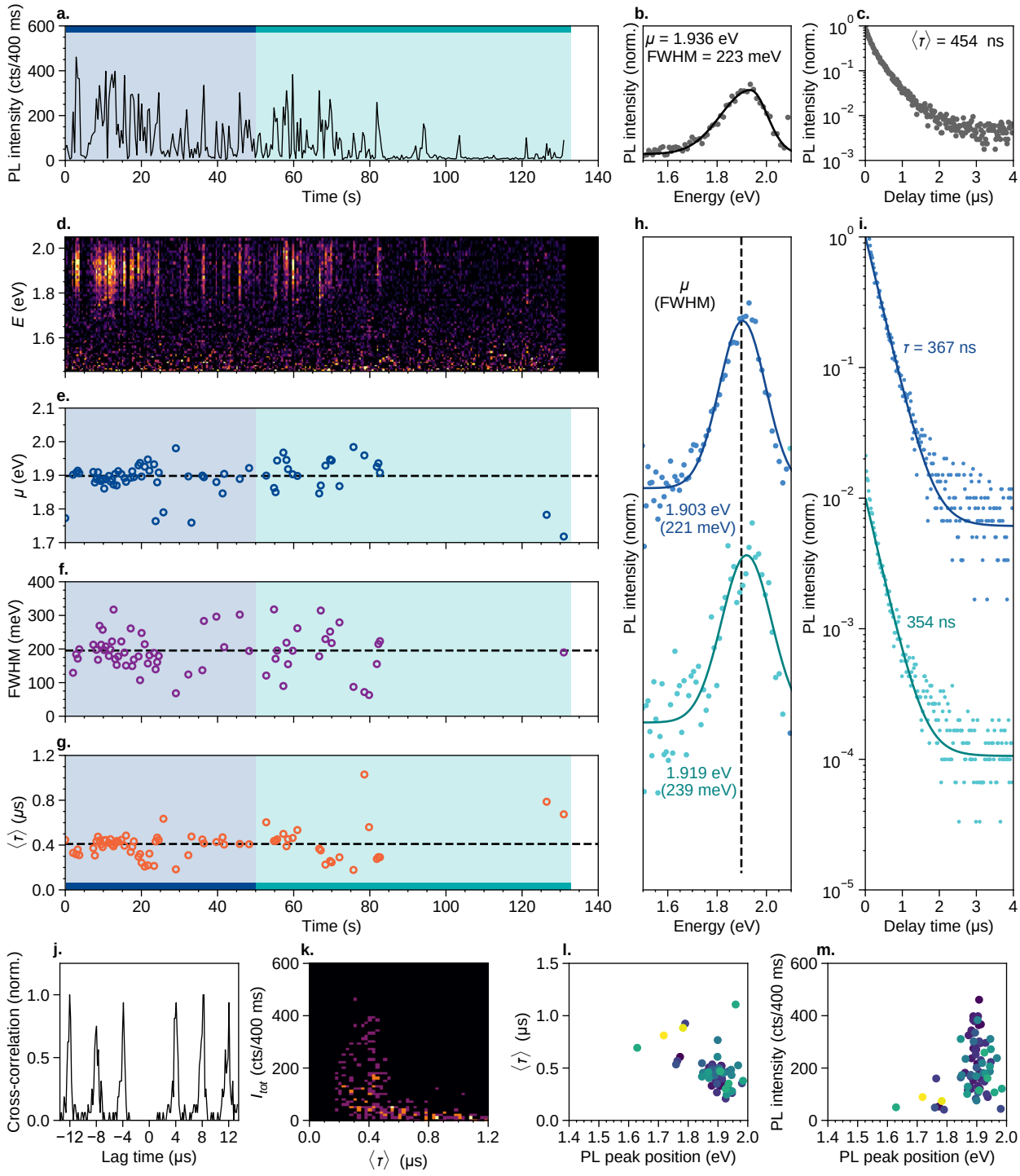

Figure E46 — Results of micro-spectroscopy experiment on core/shell $CuInS_2$/CdS quantum dot 30.

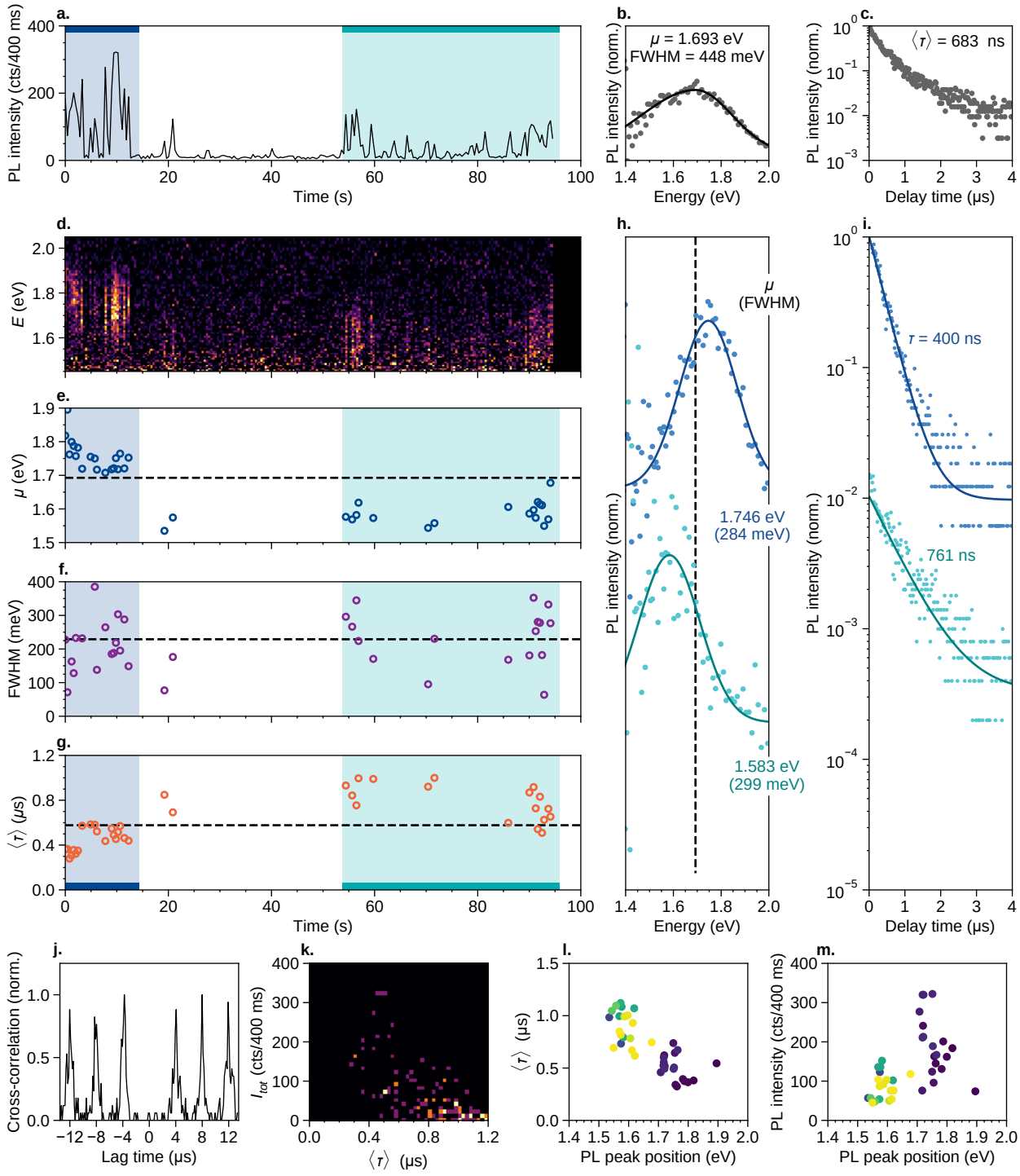

Figure E47 — Results of micro-spectroscopy experiment on core/shell $CuInS_2$/CdS quantum dot 31.

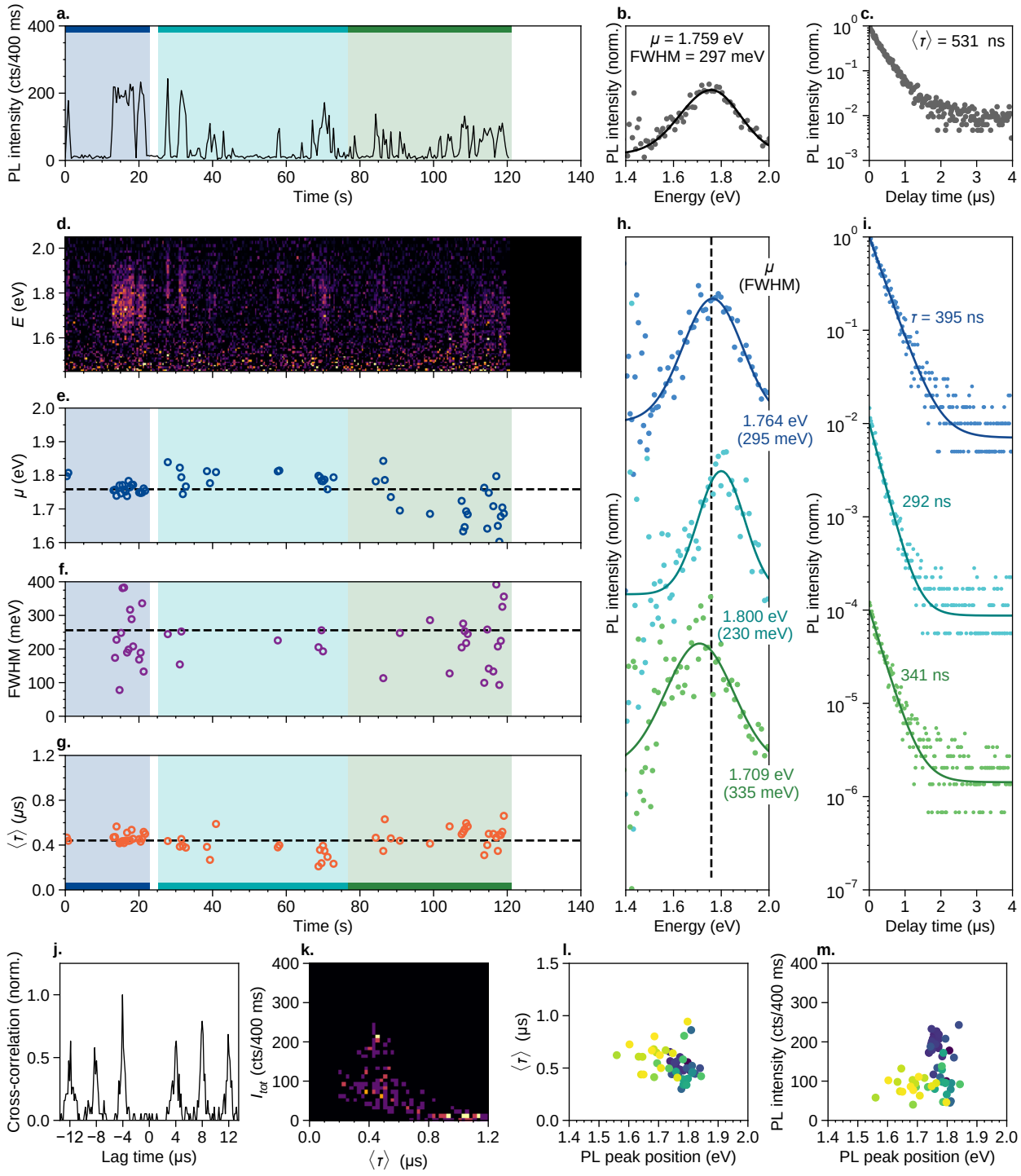

Figure E48 — Results of micro-spectroscopy experiment on core/shell $CuInS_2$/CdS quantum dot 32.

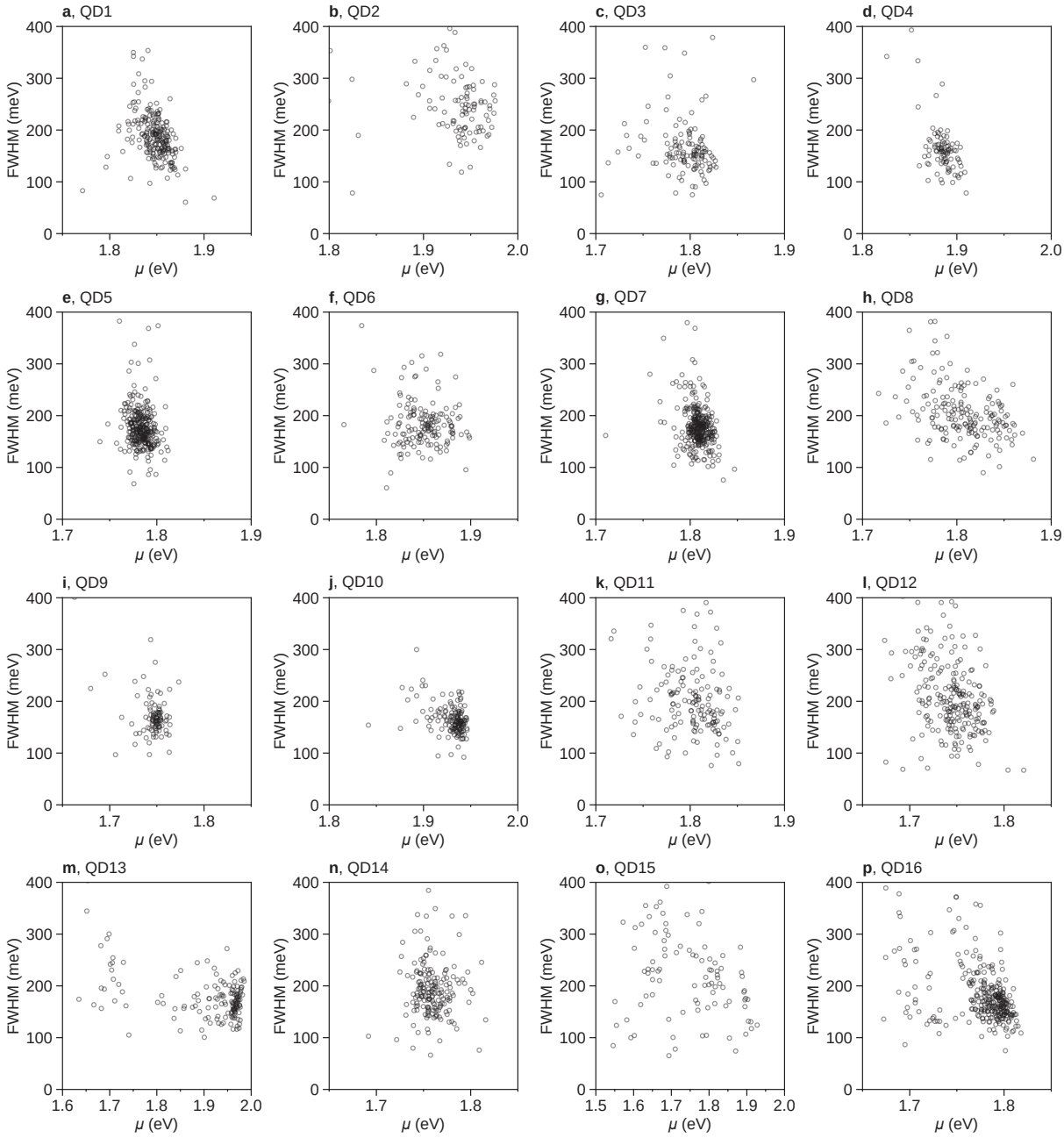
a, QD1
b, QD2
c, QD3
d, QD4
e, QD5
f, QD6
g, QD7
h, QD8
i, QD9
j, QD10
k, QD11
l, QD12
m, QD13
n, QD14
o, QD15
p, QD16
FWHM (meV)
μ (eV)

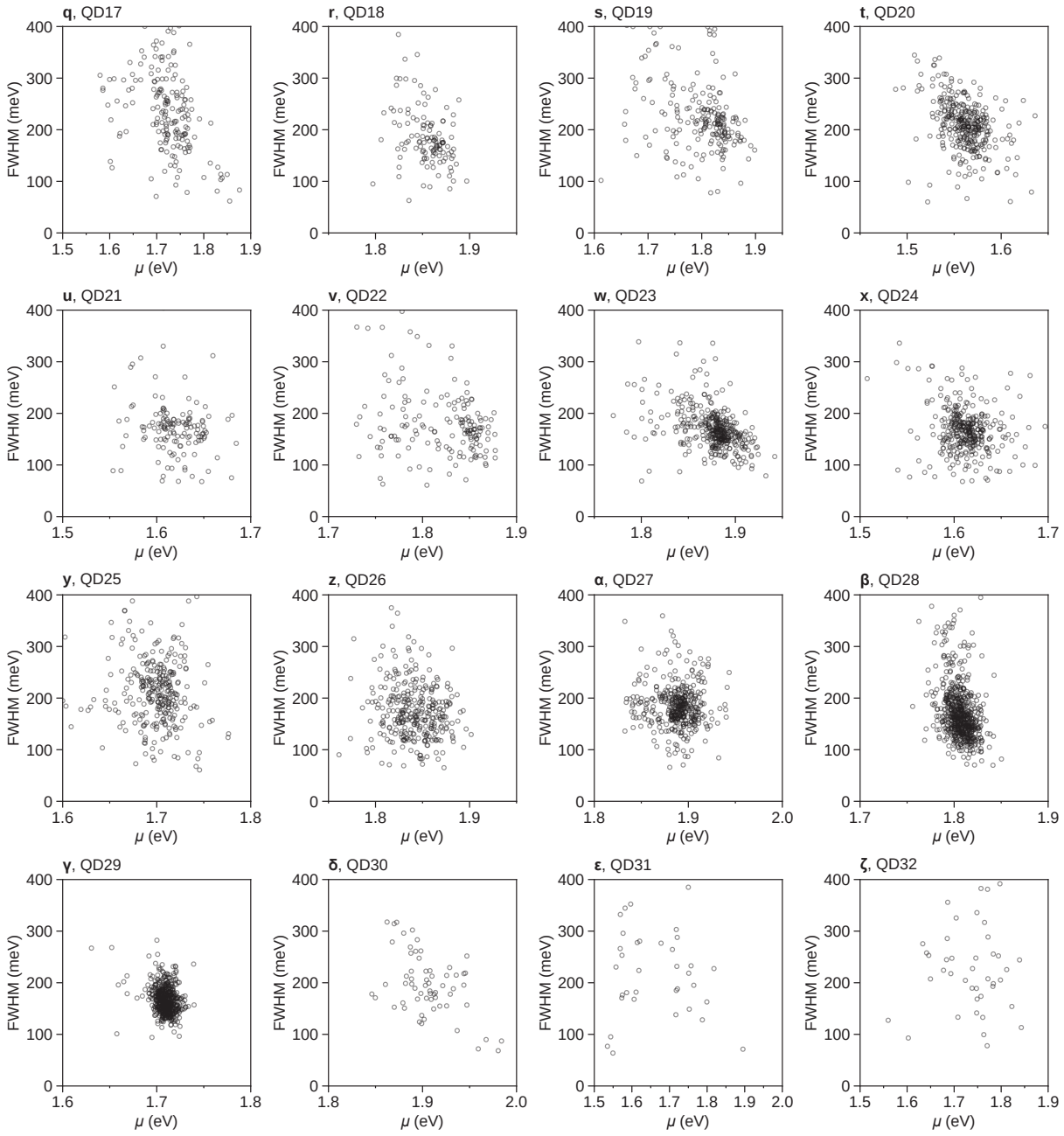

Figure E49 — Correlation of fitted linewidth and peak position for all core/shell $CuInS_2$/CdS quantum dots.

References

[1] Zhong, H.; Lo, S. S.; Mirkovic, T.; Li, Y.; Ding, Y.; Li, Y.; Scholes, G. D. *ACS Nano* **2010**, *4*, 5253–5262, DOI: 10.1021/nn1015538.

[2] Li, L.; Pandey, A.; Werder, D. J.; Khanal, B. P.; Pietryga, J. M.; Klimov, V. I. *Journal of the American Chemical Society* **2011**, *133*, 1176–1179, DOI: 10.1021/ja108261h.

[3] David, G.; Pérez, J. *Journal of Applied Crystallography* **2009**, *42*, 892–900, DOI: 10.1107/S0021889809029288.

[4] Huang, T. C.; Toraya, H.; Blanton, T. N.; Wu, Y. *Journal of Applied Crystallography* **1993**, *26*, 180–184, DOI: 10.1107/S0021889892009762.

[5] Maes, J.; Castro, N.; De Nolf, K.; Walravens, W.; Abécassis, B.; Hens, Z. *Chemistry of Materials* **2018**, *30*, 3952–3962, DOI: 10.1021/acs.chemmater.8b00903.

[6] *Norland Optical Adhesive 68 Safety Data Sheet*; Norland Products Incorporated: Cranbury, New Jersey, USA, 2019.

[7] Hinterding, S. O. M.; Rabouw, F. T. *Zenodo* **2020**, DOI: 10.5281/zenodo.4354144.

[8] Xia, C.; Wu, W.; Yu, T.; Xie, X.; Van Oversteeg, C.; Gerritsen, H. C.; De Mello Donega, C. *ACS Nano* **2018**, *12*, 8350–8361, DOI: 10.1021/acsnano.8b03641.

[9] Brandt, G.; Räuber, A.; Schneider, J. *Solid State Communications* **1973**, *12*, 481–483.

[10] Traill, R. J.; Boyle, R. W. *American Mineralogist* **1955**, *40*, 555–559.

[11] Li, T.; Senesi, A. J.; Lee, B. *Chemical Reviews* **2016**, *116*, 11128–11180, DOI: 10.1021/acs.chemrev.5b00690.

[12] Scherrer, P. *Nachrichten von der Gesellschaft der Wissenschaften zu Göttingen, Mathematisch-Physikalische Klasse* **1918**, *26 July*, 98–100.

[13] Langford, J. I.; Wilson, A. J. C. *Journal of Applied Crystallography* **1978**, *11*, 102–113, DOI: 10.1061/9780784479896.140.

[14] Momma, K.; Izumi, F. *Journal of Applied Crystallography* **2011**, *44*, 1272–1276, DOI: 10.1107/S0021889811038970.

[15] Li, P. W.; Anderson, R. A.; Plovnick, R. H. *Journal of Physics and Chemistry of Solids* **1979**, *40*, 333–334, DOI: 10.1016/0022-3697(79)90113-6.

[16] Binsma, J. J. M.; Giling, L. J.; Bloem, J. *Journal of Luminescence* **1982**, *27*, 55–72, DOI: 10.1016/0022-2313(82)90029-1.

[17] Mudryi, A. V.; Yakushev, M. V.; Volkov, V. A.; Zhivulko, V. D.; Borodavchenko, O. M.; Martin, R. W. *Journal of Luminescence* **2017**, *186*, 123–126, DOI: 10.1016/j.jlumin.2017.02.014.

[18] Brus, L. E. *The Journal of Chemical Physics* **1983**, *79*, 5566–5571, DOI: 10.1063/1.445676.

[19] Brus, L. E. *The Journal of Chemical Physics* **1984**, *80*, 4403–4409, DOI: 10.1063/1.447218.

[20] Zang, H.; Li, H.; Makarov, N. S.; Velizhanin, K. A.; Wu, K.; Park, Y.-S.; Klimov, V. I. *Nano Letters* **2017**, *17*, 1787–1795, DOI: 10.1021/acs.nanolett.6b05118.